ABSTRACT

Title of Dissertation:	DETERMINING THE EFFECT OF EXTRACELLULAR MICROENVIRONMENT ON TROPHOBLAST INVASION USING A BIOPRINTED PLACENTA MODEL
	Che-Ying Kuo, Doctor of Philosophy in Bioengineering, 2017
Dissertation directed by:	John P. Fisher, Ph.D., Fischell Family Distinguished Professor & Department Chair, Fischell Department of Bioengineering

Preeclampsia is a leading cause of maternal and perinatal morbidity and mortality, affecting 8% of all pregnancies. Currently, the only effective treatment for preeclampsia is the premature delivery of the fetus and placenta resulting in significant fetal morbidity. In early pregnancy, fetal trophoblast cells invade and remodel maternal spiral arteries in the uterine wall to create the high capacitance organ of placenta. The uterine spiral arteries in preeclampsia, however, remain narrow and poorly remodeled. The exact mechanisms of how trophoblast invade and remodel the spiral arteriole are not known, and there is a paucity of relevant experimental models to study the mechanisms in human pregnancy. The goal of this work was to develop a dynamic bioprinted placenta model and use it to determine the role of extracellular microenvironment in preeclampsia. We began by developing a

3D placenta model that could quantify trophoblast invasion rates through bioprinting. Then we used decellularization techniques to isolate and established the necessary role of placental basement membrane protein to achieve effective trophoblast invasion. Finally, we used the dynamic bioprinted placenta model and found trophoblast impairs the flow-induced angiogenesis of endothelial cells, a process that plays a central role in preeclampsia. Overall, we described the significant impact of the extracellular microenvironment on the behavior trophoblast and/or endothelial cells, an area that is less investigated but appeared to be critical in the pathogenesis of preeclampsia. Moreover, the approach presented in this work can be used to screen and develop novel therapeutics and biomarkers not only for preeclampsia but also other diseases such as cancer metastasis and wound healing.

DETERMINING THE EFFECT OF EXTRACELLULAR MICROENVIRONMENT ON TROPHOBLAST INVASION USING A BIOPRINTED PLACENTA MODEL

by

Che-Ying Kuo

Dissertation submitted to the Faculty of the Graduate School of the
University of Maryland, College Park, in partial fulfillment
of the requirements for the degree of
Doctor of Philosophy
2017

Advisory Committee:
Dr. John P. Fisher, Chair
Dr. Helim Aranda-Espinoza
Dr. Kan Cao
Dr. Keith E. Herold
Dr. Peter Kim

Dedication

This work is dedicated to my family for their unconditional support.

Acknowledgements

I would like to acknowledge my advisors, Drs. John Fisher and Peter Kim, for their guidance and support throughout my graduate school training. I would also like to thank the undergraduate researchers who contributed in various parts of this work (Ms. Kelly Rhodes, Ms. Nidhi Gandhi, Ms. Amy Garcia-Vivas, and Ms. Maria Shevchuk).

Table of Contents

List of Figures

Chapter 1: Introduction, Objectives and Background

1.1 Introduction

Preeclampsia (PE) is a leading cause of maternal and perinatal morbidity and mortality, affecting up to 8% of all pregnancies [6-8] and resulting in greater than 60,000 maternal deaths worldwide per year [9]. PE significantly impacts fetal development, and the only effective treatment for PE is premature delivery of the fetus and placenta resulting in significant fetal morbidity. The placenta serves the critical function of fetal gas exchange, nutrition and waste removal based a high flow and volume, low pressure hemodynamic environment. In early pregnancy, fetal trophoblast cells invade and remodel maternal spiral arterioles in the uterine wall to create this high capacitance system. The uterine spiral arteries in PE, however, remain narrow and poorly remodeled. The exact molecular and cellular mechanisms of how trophoblast invade and remodel the spiral arteries are not known, and there is a paucity of relevant and suitable experimental models to study the mechanisms in human pregnancy. For example, human studies during pregnancy are not feasible due to ethical, safety and regulatory constraints. Small and large animal systems as a surrogate model to study PE are sometimes misleading [10, 11]. Although current transwell-based, *in vitro* models of PE have enabled important findings, these data do not capture the complex elements and interactions in the decidua (e.g. maternal spiral vasculature, heterogeneous cell populations, extracellular matrix, and biochemical signals) [5, 11]. These limitations are particularly noteworthy since cell migration invasion can be significantly affected by their microenvironment [12].

1.2 Objectives

The overall goal of this work was to determine the role of extracellular microenvironment in preeclampsia using a bioprinted placenta model, which was accomplished through the following objectives:

1. The first objective was to develop a 3D bioprinted placenta model. Based on the Young's modulus of *ex vivo* term placenta, we bioprinted a 3D placenta model that could assess trophoblast invasion. The profile of chemotactic gradient was characterized both *in vitro* and *in silico*. The efficacy of the 3D placenta model was validated by the migratory response of trophoblasts towards epidermal growth factor.
2. The second objective was to determine the effect of placental basement membrane protein on trophoblast differentiation and invasion. Placental basement membrane proteins were isolated from basal plate of human term placenta and incorporated into the bioprinted placenta model. The effect of these placental basement membrane proteins on trophoblast invasion and differentiation were determined by measuring the invasion rates, protein, and gene expressions.
3. The third objective was to assess the impact of trophoblast on interstitial flow on the angiogenesis of endothelial cells. A perfusion based bioreactor and a 3D printed chamber customized for the bioprinted placenta model were developed to place 3D placenta model under flow. We successfully induced extensive neovascular development *in vitro*. The effect of shear stress and

trophoblast on angiogenesis of endothelial cells were characterized through quantitative image analysis and gene expressions.

1.3 Background: Spiral Artery Remodeling, Trophoblast Invasion, and Preeclampsia

1.3.1 Introduction

Spiral arteries in uterine wall develop during menstrual cycle under the influence of progesterone [13] and, without blastocyst implantation, the spiral arteries regress and are ultimately lost during menstrual shedding [13]. Following embryo implantation, the spiral arteries progressively remodel during the first 22 weeks of gestation[13]. The level of remodeling correlates with trophoblast invasion, with the greatest trophoblast invasion and vessel transformation occurring within the central region of the placental bed and becoming less extensive towards the periphery [14]. In the most remodeled vessels, there is loss of a discrete muscle layer and the endothelium can be completely replaced by trophoblast [15]. At the placental periphery where invasion is less extensive, both trophoblasts and endothelial cells can be seen to co-exist within the vessel [15]. The loss of vascular cells is accompanied by fibrinoid deposition together with the loss of vascular function, most notably responsiveness to vasoconstrictors [8]. The diameter of the resulting vessels can be increased up to 10-fold and, as a consequence, the total blood delivered to the intervillous space is increased 3–4 fold with a much reduced pressure [6]. This increased in total delivered blood meets the increasing demands of the growing fetus for nutrients, respiratory gases, and for the removal of metabolic waste [6]. Inadequate transformation of the spiral arteries reduces the total volume of blood into the intervillous space and cause a hypoxic condition in the placenta. The hypoxic condition is thought to be the cause of a number of pregnancy-related diseases such as preeclampsia [16]. Even though significant progress has been made in the

understanding of PE, little is known on how the remodeling of spiral arterioles are regulated at a cellular and molecular level [5]. Several mechanisms may be responsible for the loss of vascular cells, including migration, dedifferentiation, phagocytosis/autophagy and apoptosis [17]. It is likely that the maternal vascular remodeling is orchestrated by a combination of the above mechanisms [18].

1.3.2 Decidualization and Trophoblast-Independent Remodeling of Spiral Arteries

There are evidences suggesting that there are remodeling events of spiral artery taking place before the arrival of the trophoblast [19], which may be important for complete transformation to take place later. There are efforts aim to address these issues by comparing events that occur in normal and ectopic pregnancies, which showed that decidualization in the absence of trophoblasts leads to changes in vessel structure [20, 21]. These changes included endothelial basophilia, vacuolation, increased endothelial activation and vessel dilation [20]. However, the complete "physiological change" [22] required the presence of trophoblasts [21]. A proposed term of decidua-associated remodeling has recently to describe the remodeling of spiral arteries prior to the arrival of trophoblasts [23].

The mechanisms that regulates trophoblast-independent remodeling to prepare for more extensive transformation that takes place following trophoblast invasion have been little studied [18]. The sex steroids estrogen and progesterone play a dominant role in regulating endometrial growth and regression [24] but it is unclear exactly how these hormones directly regulate either endometrial blood vessel growth or structure. Estrogen is known to affect vascular reactivity by stimulating nitric

oxide synthesis [25]. Estrogen is also known to increase vessel permeability and endothelial cell proliferation through increased vascular endothelial growth factor (VEGF) release [26]. The direct effects of progesterone on uterine vessels remain unclear, although it may influence vascular remodeling indirectly through its effects on the recruitment of immune cells such as lymphocytes, macrophages and uterine natural killer cells to the endometrium [18]. For example, progesterone has been implicated in the regulation of leukocyte trafficking indirectly through its ability to up-regulate stromal cell chemokine expression [27].

1.3.3 Trophoblast-Dependent Remodeling of Spiral Arteries

Human trophoblasts differentiate from trophoblast stem cells along two pathways [6]. Villous trophoblasts fuse to form a syncytium and are bathed by maternal blood, whereas extravillous trophoblasts are functionally defined by their invasive nature [11]. The extravillous trophoblasts migrate from the anchoring villi to form two subpopulations. The interstitial extravillous trophoblasts invade the uterine wall, whereas the endovascular extravillous trophoblasts migrate along the lumen of the spiral artery in a retrograde manner up to the myometrial segment [17]. Why the extravillous trophoblasts target the spiral arteries but not vein is still under debate [23]. Studies have shown that venous endothelial cells express the ephrin EPHB4 and it is suggested that this acts to repulse invading trophoblasts [28]. Another possibility is that the gradients of oxygen and chemoattractant(s) from the arteries may contribute in this targeted invasion [5, 29]. Extracellular matrix changes in decidual tissue have also been observed and could also influence vessel wall structure by priming the vessel for subsequent trophoblast interaction [13].

1.3.4 Conclusion

The study of human spiral artery remodeling is restricted by the availability of biomaterial at all stages of gestation [5, 11]. The animal models are amenable to manipulation at both the cellular and molecular level. However, direct extrapolation to the human situation is not always possible, as there are significant differences seen during spiral artery remodeling between human and other mammal [30]. Similar loss of the endothelium and overall structural re-organization of the spiral arteries occurs in the mouse; however, comparison of different strains of immunodeficient mice indicates that uterine natural killer cells play a major role in remodeling of this species in the absence of trophoblasts [30]. The advances in *ex vivo* and *in vitro* placenta models enabled by 3D bioprinting and tissue engineering, along with time-lapse microscopy techniques, have enabled some of these questions to be addressed [5].

1.4 Background: Epithelial-Mesenchymal Transition (EMT) and Differentiation of Trophoblast

1.4.1 Introduction and Overview

Epithelial-mesenchymal transition (EMT) describes the process by which an immotile, polarized epithelial cell undergoes biochemical changes to attain mesenchymal cell characteristics, which include fibroblast-like morphology, matrix metalloproteinase (MMP) secretion and gaining the ability to migrate and invade [31-34]. Classic EMT events in humans include: 1) embryogenesis; 2) wound healing; and 3) cancer metastasis [31, 35-37]. Trophoblasts and malignant cells share many similar phenotypic properties including extensive proliferation, migration and invasion into neighboring tissues and vasculature, ability to evade the immune system and expression of many signaling pathways [38].

In early placental development, trophoblasts differentiate and lose their organized epithelial phenotype and transition to a migratory and invasive mesenchymal phenotype allowing them to infiltrate into the maternal decidua and spiral arteries. This transition has been suggested as the 4th type of EMT [31, 37]. However, in contrast to the environment of tumor cells, the uterine environment very tightly controls trophoblast behavior in a spatial-temporal manner. This is evident since EVT invasion is restricted to the decidua and the first third of the myometrium at the maternal-fetal interface in uncomplicated pregnancies. With the very tight controls on trophoblast migration and invasion, disruption to their tight homeostasis is also thought to contribute to many pregnancy pathologies. For example, shallow invasion is a characteristic feature of pre-eclampsia and fetal growth restriction, while

abnormal deep EVT invasion is associated with placenta accreta/increta/percreta and uncontrolled invasion by EVT is associated with choriocarcinoma.

A wide diversity of EMT inducers exists. Multiple extracellular stimuli such as growth factors, hormones, cytokines, chemokines or cell-matrix contacts, miRNAs initiate signaling upon interaction with receptor tyrosine kinases (RTKs), G-protein-coupled receptors (GPCRs), integrins or others [35]. This ultimately leads to the activation of critical signaling cascades such as mitogen-activated protein kinases (MAPKs), focal adhesion kinase (FAK), the phosphoinositide 3-kinase (PI3K)-Akt pathway or Janus kinase (JAK)-Signal Transducers and Activators of Transcription (STAT) and the whole of Wnt signaling cascades controlling a wide range of biological processes including proliferation, differentiation, migration and apoptosis [35]. Nevertheless, despite the vast range of inducers, many of the signaling pathways have similar end points. These inducers often promote EMT via regulation of downstream transcription factors. A key challenge in establishing the definitive role of any inducing signal of EMT is that the effects of any given EMT inducer are context dependent. Drawing parallels from one field of biology is often difficult, which requires basic research to identify and resolve these context dependent effects. For example, transforming growth factor β (TGF-β) plays multifunctional roles in the regulation of cell behavior, and is implicated in both developmental biology and cancer biology [37]. EMT is reported to be mainly mediated by TGF-β family receptors and tyrosine kinase receptors [35].

1.4.2 Inducer of EMT: TGF-β Superfamily

TGF-β is noteworthy for its paradoxical actions in EMT, having both inhibitory and stimulatory effects on cell growth. During early trophoblast invasion in the first trimester, the maternal plasma levels of TGF-β is downregulated [39, 40]. In the early stages of cancer, TGF-β acts as a growth inhibitor and tumor-suppressor; but in the later stages, it can act as a potent inducer of EMT. Genetic and molecular changes in malignant cells are thought to alter their responses to signaling molecules. TGF-β plays crucial roles in regulating trophoblast cell adhesion, proliferation, differentiation, migration and invasion at the maternal-fetal interface. TGF-β exists in 3 different isoforms, with TGF-β1 and TGF-β2 thought to be the most important at the maternal-fetal interface [41]. EVTs within the placental bed express TGF-β2, while extracellular TGF-β1 and cytoplasmic TGF-β2 are localized within the decidua [41]. TGF-β1 and TGF-β2 inhibit trophoblast proliferation, migration and invasion, and increase formation of multinucleated cells [36]. These data suggest that TGF-β is an important growth factor that is secreted by the decidua and has a role in controlling trophoblast invasion, while protecting maternal tissues from over-invasion by trophoblast cells.

1.4.3 Inducer of EMT: Tyrosine Kinase Receptor (TKR) Family Growth Factors

Tyrosine kinase receptor family is another class of EMT inducer for tumor cells that promotes trophoblast migration and invasion. Interestingly, among tyrosine kinase receptor family growth factors (e.g. FGF [42], IGF [43-46], EGF [47, 48] and PDGF [49]) which have demonstrated significant effects on placenta development

and fetal growth [50], only EGFR appears to have a direct and specific impact on endometrial susceptibility to implantation *in vivo* based on a murine EGFR-ablated uterus model. [51] And EGF showed reduced expression in preeclamptic human trophoblasts. [47]. EGF acts through the PI3K/Akt pathway, a major signaling component downstream of growth factor receptor tyrosine kinases that regulates normal cellular processes including motility, proliferation, survival and [52]. During early trophoblast invasion in the first trimester, the maternal plasma levels of EGF are elevated [53, 54]. Indeed, there are evidences that suggest EGF induces partial EMT of trophoblast by promoting invasion [5], increasing the abundance of MMP-9 [55], and upregulating expression of fibronectin [56], a known EMT inducer for mammary epithelial cells via the tyrosine kinase receptor [57].

1.4.4 Conclusions

Our current understanding of EMT in the human placenta is limited [35]. Trophoblasts are unique in this arena because even though they also undergo extensive proliferation, migration and invasion, there are mechanisms that precisely control these functions [36]. Determining the spatial and temporal expression of important EMT markers and establishing their roles in the placenta are essential to understanding trophoblast regulation and placental development in early pregnancy [36]. Trophoblast functions, particularly proliferation, migration and invasion are likely to be influenced by EMT regulators [31]. Furthermore, unravelling the complex pathways and interactions that characterize the EMT in normal placental development will provide important clues in our understanding of how a deregulated EMT contributes to the pathogenesis of pregnancy complications such as preeclampsia.

1.5 Background: Recent Developments in 3D In Vitro Models to Assess Cell Migration

1.5.1 Introduction

Cell migration is fundamental in many biological processes such as angiogenesis [58], wound healing [59], cancer metastasis [60], neural growth [61], and placental development [6]. These biological processes have significant health implications. For example, according to American Cancer Society, it is estimated that 600,000 cancer-related death occur in US alone yearly and the national expenditures for cancer totaled to nearly $125 billion [62]. Currently, the standard procedure of screening for potential therapeutic drugs begins with the 2D culture-based *in vitro* tests, followed by preclinical testing using animal models, and finally to clinical trials. Under this procedure, only about 10% of the potential drug passed through clinical development [63]. Many of the drug failed in clinical trials due to the lack of clinical efficacy and/or unacceptable toxicity, which could be attributed to the unreliable data collected from the 2D monolayer culture tests where cellular response to drug was altered because of their unnatural microenvironment [63]. To lower the cost of the failed compounds/molecules, the ineffective and toxic compounds should be screened out as early as possible, preferably before animal testing. Therefore, there's a pressing need for developing more advanced *in vitro* 3D migration systems that more realistically recapitulate the *in vivo* cell behaviors and provide more reliable results to predict clinical efficacy.

The low cost and convenience features associated with *in vitro* models made them very attractive when compared to animal models. However, most of the current

in vitro cell migration assays are often performed in 2D culture systems with flat and rigid surfaces (plastic and/or membrane surfaces). Although these approaches have produced substantial knowledge regarding cell migration, there are several fundamental differences between 2D and 3D microenvironment that may influence cell behavior [63, 64]. For example, cells cultured in 2D often results in different morphology, proliferation rates, and gene/proteins expressions compare to cells in 3D and *in vivo* [64, 65]. And it has been demonstrated that cell responses in 3D cultures are more similar to *in vivo* behavior compare to 2D culture [63, 65]. Moreover, important properties such as matrix stiffness, fluid shear stress, surface topology, and spatial arrangement of biomaterials on cell migration would be difficult to manipulate using conventional 2D culture system [66]. As such, considerable efforts have been put into engineering 3D *in vitro* models to assess cell migration. Such 3D culture systems provide excellent *in vitro* models, allowing the study of cellular migratory responses in a setting that resembles *in vivo* environments. The goal of this work was to highlight the recent developments in 3D cell migration models in the following fields: (1) angiogenesis and wound healing; (2) cancer metastasis; (3) neural/brain growth; and (4) placental development. The scope of this review is limited to studies published in the past 10 years with emphasis with 3D migration models that manipulated parameters that are difficult to tune in conventional 2D culture. Based on the reviewed literature, we proposed three design criteria that should be considered when fabricating a tissue models to assess cell migration.

1.5.2 3D Migration Models to Study Angiogenesis and Wound Healing

Angiogenesis is the development of new micro-vessels from existing blood vessels, which involves proliferation and migration of endothelial cells [67]. In adults, angiogenesis rarely occurs except in would healing, pathological conditions and/or endometrium growth during menstrual cycle/pregnancy [67]. There is a strong interest in creating vascularized engineered tissues of clinically relevant size for translation [68]. Even though angiogenic effects of soluble factors such as vascular endothelial growth factors (VEGF) has been extensively studied, biophysical properties such as flow-mediated angiogenic remodeling of endothelial cells remain unclear. As such, Song et al. developed a microfluidic tissue analog to investigate the role of fluid shear forces in controlling endothelial cells migration [69]. They found that fluid shear stress from flowing blood attenuated sprouting of endothelial cells. Furthermore, positive VEGF gradients initiated sprouting but negative gradients inhibited sprouting, promoting instead sheet-like migration analogous to vessel dilation. These results there are interactions between the angiogenic cues (shear stress and VEGF). In another study, the effect of interstitial flow on the angiogenic response and phenotype of endothelial cells was investigated in a 3D microfluidic device [70]. The authors found that in the presence of interstitial fluid significantly facilitated vasculogenic organization of the microvascular network regardless of the direction of the flow. In contrast, angiogenic sprouting was promoted only when the directions of flow and sprouting were opposite while angiogenic activity was suppressed into the direction of flow. This is one of the first reports evaluating the effect of inferential

flow on angiogenetic response, a physiologically relevant yet rarely investigated and difficult to study in conventional 2D culture systems

To investigate interactions between endothelial cells and stromal cells, Belair et al. demonstrated a strategy to model blood vessel development using a induced pluripotent stem cell derived endothelial cell type (iPSC-EC) cultured within engineered platforms that mimic the 3D microenvironment [71]. In this study, the iPSC-ECs yielded perfusable, interconnected lumen when co-cultured with primary human fibroblasts, and aligned with flow in microfluidics devices. iPSC-EC functions during tubule network formation, barrier formation, and sprouting were consistent with those of primary ECs. This study provided an alternative source of endothelial cells and demonstrated the importance of cell-cell interactions. In addition to endothelial-fibroblast interactions, Trkov et al. developed a novel micropatterned three-dimensional hydrogel system to study human endothelial–mesenchymal stem cell interactions [72]. They showed mesenchymal stem cells had strong distance-dependent migration toward endothelial cells and supported the formation of stable vascular networks resembling capillary-like vasculature, emphasizing the effect of spatial arrangement of biomaterials on cell behavior.

Surface topology is another regulating parameter for angiogenic response that would be difficult to study in 2D *in vitro* culture systems. Hadjizadeh et al. used polymer fibers that were covered with endothelial cells to induce directional angiogenesis in a 3D coculture system [73]. These endothelial cells-covered fibers were embedded in a fibrin gel, following a parallel alignment pattern, in the presence of fibroblasts. Tube-like structures occurred along the fibers and a network was

formed between neighboring fibers. Biomolecule-grafted fibers created a guidance pathway that facilitated coated endothelial cells to form lumens and, from them, sprouting processes [73]. In addition, Sundararaghavan investigated the effect of topological cues in regulating angiogenesis response of endothelial cells. Aligned fibers were created by electrospinning technique. When fibers were aligned perpendicular to a chemical gradient, cells were directed by fiber alignment and there was no effect of the chemical gradient. These results suggest that topographical cues may be more influential than chemical cues in directing cell motility and should be considered in material design. However, the physiological relevance of surface topology *in vivo* is unclear.

Mechanical properties and composition of extracellular matrix play important roles in the migration of endothelial cells but are difficult to study using conventional 2D platform [74]. To address this challenge, Turturro et al. developed an *in vitro* model with gradients of elastic modulus and MMP-sensitive peptides to determine their effects on angiogenesis of endothelial cells [74]. Aggregate invasion in gradient hydrogels occurred with sprout alignment observed in the direction parallel to the gradient while control hydrogels with homogeneous properties resulted in uniform invasion. This directionality was found to be more prominent in gradient regions of increased stiffness, crosslinked MMP-sensitive peptide presentation, and immobilized YRGDS concentration. In another study, the effect of the degradability of extracellular matrix on endothelial cells migration was investigated [75]. Trappmann et al. developed an 3D migration model whereby molded tubular channels inside a novel dextran-based hydrogel were seeded with endothelial cells and subjected to

chemokine gradients within a microfluidic device. They demonstrate that matrix degradability switched 3D endothelial cell invasion between two distinct modes: single-cell migration and the multicellular, strand-like invasion required for angiogenesis, introducing a new parameter to tune endothelial cell migration. All these studies have shown that biochemical and biomechanical properties of the extracellular matrix significantly regulate the migration of endothelial cells, which would be challenging to study using 2D *in vitro* models.

As demonstrated, these recently developed *in vitro* angiogenic models have successfully characterized the impact of the cellular microenvironment on migration of endothelial cells. However, these models often lack smooth muscle cells that wrap around the endothelial cells. In addition, many of these models were based on microfluidics. While they are useful for mechanistic studies at the cellular level, they are not necessary relevant in generating vascularized tissues grafts/models in clinically relevant size (millimeter-centimeter scale).

Wound Healing

Cell migration is critical in the wound healing process, which has significant health implications [76]. It is estimated that there are 47.5 million cases of trauma cases every year with a total of $695 billion of economic burden [77]. In a recent study, a fibroblast migration model was 3D bioprinted using gelatin-based hydrogel to assess wound healing responses to in tympanic membrane perforation [78]. Epidermal growth factor was predicted to promote wound closure based on the invasion rates of a murine fibroblast cell line. This result was later validated by *in vivo* results using chinchilla models, demonstrating the predictive value of the 3D

fibroblast migration model [78]. In another study that also focused on regenerating soft tissue, Grasman et al. created an *in vitro,* 3D outgrowth assay system to mimic cell recruitment *in vivo* [79]. They used this system to investigate the effect of a growth factor (hepatocyte growth factor (HGF))-loaded, fibrin micro-threads on myoblast recruitment [79]. They showed that HGF loaded micro-threads supported enhanced myoblast migration. Looking at migration a relatively less explored tissue, Aizawa et al. developed a new hydrogel model to evaluate interactions between endothelial cells and retinal stem and progenitor cells [80]. They found ECs adopted tubular-like morphologies similar to those observed *in vivo* and inhibited proliferation and differentiation of retina stem and progenitor cells. These studies again emphasize the importance of spatial orientation of different cell populations and cell-ECM interactions in governing cell migration.

In additional to migration models for soft tissues, other investigators developed 3D models to investigate cell migrations in bone injuries. Sundelacruz et al. developed a 3D tissue engineered bone model to determine the roles of bioelectric modulation in bone regeneration, contrast with the more common exogenous stimulation of bone using applied electromagnetic fields. They developed bone-like scaffold by seeding human mesenchymal stem cells on silk, and cultured under osteogenic conditions. A bone "injury" was created by carving out a portion of the differentiated bone-like scaffold, and inserted a fresh and acellular scaffold to fill the wound. Using this system, they identified two electrophysiology-modulating compounds (glibenclamide and monensin) that augmented osteoblast mineralization, suggesting a new parameter to be considered in bone tissue engineering. However,

the authors did not assess the mechanical integrity of these bone models, which is the primary function of bones *in vivo*. Also focusing on bone tissue engineering, Muerza-Cascante et al. developed an *in vitro* model using 3D printed polycaprolactone (PCL) scaffolds to create a construct that mimics the human endosteum [81]. This 3D tissue-engineered endosteal microenvironment supported the growth and migration of primary human hematopoietic stem cells (HSCs) when compared to HSCs maintained in 2D culture. Overall, these recently developed *in vitro* wound healing models demonstrated the relationship between cell migration with their cellular microenvironment. However, their relevance in predicting *in vivo* in wound healing response is limited because the effects of macrophages and other immune cells, which are critical in the wound healing process [82, 83], were not included.

1.5.3 3D Migration Models for Cancer Metastasis

Despite the significant advancements in early diagnostic and therapeutic regimens, the metastatic progression of tumors remains a leading cause of mortality in cancer patients [84, 85]. The hallmark of tumors is the ability of cancerous cells to disseminate and invade to distant organs [85]. The metastatic process is heavily influenced by the extracellular matrix (ECM) density and composition of the surrounding tumor microenvironment [86]. Understanding the complex mechanisms of tumor cell migration within conventional 2D *in vitro* models is challenging and there has been an increase in tissue engineered solutions to model the tumor microenvironment in 3D.

There is a significant amount of efforts in developing 3D *in vitro* models to investigate epithelial-breast cancer interactions, one of the most common cancers

[62]. In one study, Carey et al. developed a 3D multicellular spheroid coculture model that recapitulated the cellular diversity and fully 3D cell–cell and cell–matrix interactions in breast cancer [87]. Their results indicated that the heterogeneous subpopulations within a tumor could possess specialized roles during tumor migration. These complex interactions among the various subpopulations of cancer cells within a tumor could regulate critical aspects of tumor biology and affect clinical outcome [87]. Recently, a new model of breast cancer was proposed featuring both epithelial and stromal tissues arranged on a microfluidic chip to monitor tumor progression [88]. Similarly of what's been reported *in vivo*, they found ECM remodeling in terms of hyaluronic acid and fibronectin overexpression in the stroma compartment (modeled by fibroblasts) [88]. In another study based on a microfluidic approach, Hockemeyer investigated the effect of cancer-associated fibroblasts and endothelial cells on breast cancer cell migration [89]. They found breast cancer cells responded differently between normal fibroblast and tumor-associated fibroblast [89]. To model long-term cancer progression, Estrada et al. developed an alginate-based assay in which aggregates of human breast cancer cells were microencapsulated in alginate, either alone or in combination with human fibroblasts, and cultured for 15 days [90]. Over the culture period, there was a reduction in estrogen receptor and membranous E-cadherin alongside loss of cell polarity, increased collective cell migration and enhanced angiogenic potential in co-cultures, which are phenotypic alterations typical of advanced stages of cancer [90]. These features were not observed in the monocultures of MCF-7 cells [90]. Overall it is clear that interactions

between stromal cells and breast cancer cells play a vital role in the activation of breast tumors to metastasize, a biological process that would be hard to model in 2D.

In addition to cell-cell interactions, other 3D breast cancer migration models were developed to investigate other microenvironmental effects. Boghaert et al. explored how the biophysical characteristics of the host microenvironment affected the proliferative and invasive tumor phenotype of the earliest stages of tumor development [91]. They used a 3D microfabrication-based approach to engineer ducts composed of normal mammary epithelial cells that contained a single tumor cell. Regions of invasion correlated with high endogenous mechanical stress, which suggests that the mechanical tone of nontumorigenic host epithelium directed the phenotype of tumor [91]. In addition, DelNero et al. utilized alginate-based, oxygen-controlled 3D tumor models to study the interdependence of culture context and the hypoxia response [92]. Notably, they showed pro-inflammatory pathways are critical regulators of tumor hypoxia response within 3D environments that ultimately impact tumor angiogenesis, potentially providing important therapeutic targets [92]. Altogether, these studies on breasts cancer migration demonstrated the considerable impact of ECM mechanical properties and oxidative stress on breast cancer migration, parameters that are difficult to investigate in 2D plastic culture.

3D colon cancer models, another common cancer especially among men [62], are another area under intense research. Nietzer developed a 3D colorectal cancer model based on decellularized porcine intestinal scaffold [93]. Colon cancer cell lines in their 3D colorectal cancer model showed decreased numbers of proliferating cells compare to 2D, a feature observed consistent with previous findings [64]. To foster

tissue generation, they assembled a bioreactor and induced a tissue-like association of cultured tumor cells with fibroblasts reflecting tumor biopsies [93], demonstrating the value of using tissue-specific biomaterials for disease modeling. Another group developed a 3D colon cancer model comprised of a dense artificial cancer mass. This model was created by partial plastic compression of collagen type I containing colorectal cancer cells, nested in a non-dense collagen type I gel populated by fibroblasts and/or endothelial cells [94]. Tumor formed spheroids which invaded the surrounding matrix, away from the hypoxic conditions in the core of the construct, demonstrating the migratory effect of oxygen gradient as observed in breast cancer models. In another study using a collagen-based, compartmentalized approach, Magdeldin showed that ECM density was associated with an altered colon cancer migration pattern from aggregates to epithelial cell sheets. Laminin appeared to be a critical component in regulating endothelial cell morphology and vascular network formation [95], again emphasizing the critical role of extracellular matrix on cell migration.

Another type of cancer that attracted researchers to develop 3D migration models for is skin cancer, the largest organ in human. Okochi et al. developed a novel magnetic cell culture array to study interactions between fibroblast and melanoma in spheroid culture [96]. Using a pin-holder device made of magnetic soft iron and an external magnet, magnetically labeled cells on the collagen gel-coated surface were patterned precisely. The presence of fibroblasts significantly increased the invasive capacity of melanoma, and the promotion of adhesion, migration, and invasion were also observed. This magnetic-based fabrication approach was quite unique, and they

demonstrated its feasibility in their study. However, the advantage of this approach over microfluidics and 3D printing was unclear. Moreover, another research group developed a wounded and inflamed *in vitro* 3D melanoma model to investigate the use of an anti-inflammatory on melanoma invasion [97]. The tissue engineered skin model was based on human de-epidermised acellular dermis to which keratinocytes, fibroblasts and three different melanoma cell lines were added in various combinations. A simple incisional wound was made in the model and TNF-α and fibrin were added to simulate conditions of inflammation. Addition of anti-inflammatory drugs significantly decreased invasion of A375SM skin cancer cell line. This is one of the few studies that investigated the role inflammatory response in migration of skin cancer cells.

Altogether, these recent cancer migration models have demonstrated the significance of extracellular matrix and stromal cells on metastasis. The usage of tissue-specific ECM is interesting and should be applied in other migration models for other tissues. However, important features of tumors such as the heterogenous matrix stiffness [98], immune cells [98], and tortuous vasculatures [99] should be included in future cancer migration models, which would be future studies.

1.5.4 3D Migration Models for Neural Science and Brain Development

There are a number of emerging 3D *in vitro* models to investigate neuronal migration, a pivotal step to form a functional brain [100]. Impaired neuronal migration is believed to contribute the pathology of psychiatric disorders including schizophrenia, autism spectrum disorders and epilepsy [100]. Romano developed a microfluidic device with 3D protein-engineered hydrogels to study the effect of RGD

ligand density on neurite pathfinding [101]. In this work, the authors combined gradient-generating microfluidic devices with 3D protein-engineered hydrogels to study the effect of RGD ligand density on neurite pathfinding. Neural spheroids were encapsulated in elastin-like polypeptide hydrogels presenting with ligands and exposed to a microfluidic gradient of nerve growth factor. The authors found a trade-off between neurite extension and neurite guidance, which mimics the well-known trade-off between adhesive forces at the leading and trailing edges of a migrating cells. Continue to investigate neuronal-extracellular matrix interactions, Koivisto et al. developed a new biomimetic hydrogels based on gellan gum [102]. The crosslinked gellan gum hydrogel showed properties comparable to native brain tissue under physiologically relevant stress and strain. Human neuronal cells demonstrated biocompatibility in the gellan gum-based hydrogels. Functionalization of hydrogels with laminin resulted neuronal cell maturation and neurite migration, but the mechanism of action was unclear, which called for future study [103]. Recently, a novel approach combining the advantages of self-organizing organoids (e.g. recapitulating early developmental events) and bioengineered constructs (e.g. reproducibly generate desired tissue architectures) to produce guided self-organization and cortical plate formation in human brain organoids was presented [104]. They modeled the distinctive radial organization of the cerebral cortex and allowed for the study of neuronal migration. It was elegantly demonstrated that combining 3D cell culture with bioengineering techniques could better replicate the biological processes while improving tissue integrity. In another study, an *in vitro* 3D model of motor nerve regeneration was developed to study motor neuron axonal

migration [105]. Mouse spinal cord motor neurons were seeded on a collagen sponge populated with Schwann cells and fibroblasts. This fibroblast-populated sponge was intended to mimic the connective tissue supporting axon migration. The authors showed a vigorous neurite elongation and demonstrated the spontaneous formation of numerous thick myelin sheaths surrounding motor fibers after long-term culture (28 days) [105].

In summary, these advanced *in vitro* neuronal migration models enabled researchers to study the complex interactions between cells, extracellular matrix, and gradients of soluble factor - parameters that are difficult to study using conventional 2D culture. The novel approach of combining organoid and bioengineered construct was promising and this hybrid fabrication approach is likely to generate biologically functional neuronal migration model with the required structural integrity. However, additional microenvironmental factors such as brain interstitial fluid, which could play important roles in cell-cell communication, drug delivery, and immune function of the brain [106], should be considered in future studies to improve the physiological relevance of these neuronal migration models.

1.5.5 3D Migration Models for Placentation

A relatively less explored cell migration phenomenon in 3D culture is trophoblast invasion and placental development. The formation of placenta involves trophoblast invasion and substantial remodeling of the maternal spiral arteries [107]. Impaired trophoblast invasion and remodeling of the spiral arteries has significant implication in preeclampsia, a leading cause of maternal and fetal morbidity and mortality. Recently, a 3D printed, bioengineered placenta model to evaluate the role

of trophoblast migration in preeclampsia was developed [5]. Utilizing the capability of 3D bioprinting and shear wave elastography, the authors developed used the 3D placenta model to study and quantify trophoblast migration and demonstrated a positive correlation between trophoblast migration rates and EGF concentration. In another study, Aldo et al. developed an *in vitro* model to evaluate endothelial–trophoblast interaction and signaling in a 3D system [108]. Human endometrial endothelial cell line and first trimester trophoblast cells were co-cultured and the trophoblast achieved complete replacement of the endothelium. Even those both 3D trophoblast migration model successfully demonstrated the impact of microenvironment, the mechanism of actions remained unclear.

1.5.6 Design Criteria for Fabricating 3D *In Vitro* Cell Migration Models

Based on these recent developments in 3D *in vitro* migration models, we propose 3 design criteria to be considered when fabricating a 3D migration model: 1) inherent properties of tissue and biomaterial; 2) the microenvironmental parameter to be assessed; 3) scale of the tissue.

First, one would need to appreciate and select an appropriate biomaterial(s) that allow for cell adhesion and migration, while mimicking the bulk mechanical properties of the tissue. This is important because matrix stiffness has been demonstrated to play a significant role in cell behavior [109]. For example, enzymatic-degradable hydrogel (e.g. collagen [98], gelatin [78], and fibrin [79]) would be a prime candidate to model cell migration in soft tissues and synthetic material such as polycaprolactone (PCL) [81] or poly(lactic-co-glycolic acid) (PLGA) [110, 111] would be used to model cell migration in bones or cartilage. However, if

these synthetic materials will need to be functionalized by inserting MMP-sensitive and cell adhesion protein sequences to study cell migration. The biofabrication approach that utilizes both hydrogel and stiff synthetic polymer was presented, which is likely to yield the more physiologically relevant 3D cell migration models in the future [112]. This approach allows cells to be encapsulated in 3D, which is similar to *in vivo*, while maintains the necessary mechanical integrity. In addition, the ability to monitor the movement of cells is critical in studying cell migration [113]. Although post processing such as histological sections can be performed, real-time observation using microscopy would ideal for determining the dynamic migratory responses of cells in the 3D microenvironments. In this regard, translucent materials such as polydimethylsiloxane (PDMS) used in microfluidic devices [88] and gelatin methacrylate [114] would likely be more suitable for real-time, *in situ* imaging.

Secondly, the microenvironmental parameter that modulates cell migration would need to be considered before fabricating the 3D migration models. For example, if fluid shear stress is the parameter of interest, the migration model must be able to be cultured under dynamic flow. In this case, microfluidics [115] or perfusion based bioreactor [111, 116-118] would provide the necessary biophysical cue. On the other hand, if cell-ligands in extracellular matrix is the process of interest, synthetic polymer with defined and tunable chemical structures would be appropriate as the peptide chains of natural polymers are generally not well-defined [74]. Moreover, if the initial spatial arrangement of biomaterials is important in cell migration, one would need to use a fabrication method that enable patterning of cells/extracellular

matrix/growth factors such as 3D (bio)printing, microfluidics, and compartmentalized molding technique.

Lastly, the scale of the tissue would need to be considered. For example, if one is investigating angiogenesis with an intent to directly fabricating pre-vascularized tissue for human implantation, one would avoid using microfluidics because human tissue is typically in millimeter-centimeter scale. Moreover, diffusion of nutrients would need to be considered to prevent undesired necrosis when deciding on a scale for the cell migration model [116], which is typically not an issue in microfluidic devices. Altogether, the scale of the cells migration model must be considered because scaling up from micrometer scale to clinically relevant scale can be problematic [119].

1.5.7 Conclusions

In this work, we have highlighted the recent developments of 3D *in vitro* cell migration models and proposed three design considerations. Even though significant progress in bioengineering and biomaterials has enabled investigators to study the impact of microenvironment (e.g. fluid flow, cell-cell interactions, extracellular matrix) on cell migration in 3D, the effects of immune cells, tissue-specific ECM [120], and patient-specific cells/ECM should be considered in future work. Considering the proposed design considerations, it is not surprising that microfluidic devices has become a popular platform technology to study cell migration as spatial arrangements of biomaterials and fluid flow can be relatively easily accomplished. However, the inherent micron-scale of these devices calls for a need to fabricate 3D migration models in the scale of human tissue scale (millimeter-centimeter), in which

3D bioprinting and perfusion bioreactor system can be utilized. With the advancement the enabling technologies (e.g. microfluidics, 3D printing, and perfusion based bioreactor), we believe more complex and physiologically relevant *in vitro* 3D migration models will continue to be developed.

Chapter 2: Development of the Bioprinted Placenta Model

2.1 Introduction

In normal pregnancy, placentation occurs by trophoblast invasion of the maternal spiral arteries that resides in the decidua which produces a low-resistance, high-flow maternal uterine circulation [6, 9, 121, 122]. The maternal decidua will later become the maternal side of the placenta which consist of cotyledons [123]. The trophoblasts will form the fetal side, which consist of the chorionic villi and the fetal plate [123]. In contrast, poor placentation appears to arise from interactions between inadequate trophoblast invasion, leading to reduced placental perfusion and oxidative stress resulting in the production of inflammatory cytokines [6, 9, 121, 122]. One of the major complications resulting from poor placentation is preeclampsia (PE), which is a leading cause of maternal and perinatal morbidity and mortality affecting 3 to 8% of all pregnancies [6, 9, 107, 121, 124]. Complications of PE include preterm delivery, cerebrovascular accidents, liver rupture, pulmonary edema, and acute renal failure that can result in maternal death [6, 9, 107, 121, 124-126]. The pathogenesis of preeclampsia remains poorly understood and no effective treatment is available today other than premature delivery of the fetus and placenta [9]. The lack of effective experimental models has been the major obstacle to understanding the pathobiology of PE [11, 15, 127]. The current paucity of clinically relevant experimental models impedes efforts to identify prognostic indicators and potential effective treatment options [6, 11, 107, 121]. For example, any clinical testing on pregnant mothers is often not feasible due to ethical and regulatory constraints. Animal models used to study PE are not directly relevant and are misleading as the placentation process in

humans is very different from those of other species [11, 127]. Although researchers have been using *in vitro* models of PE, these models are often based on transwell membranes and therefore do not recapture the complex elements of the maternal decidua (growth factor-secreting maternal spiral vasculature, heterogeneous cell populations, extracellular matrix (ECM), and biochemical cues) [11]. This limitation is particularly noteworthy since these complex elements are critical to the development of PE [6, 9, 107, 121, 124].

Extrusion-based bioprinting is a subclass of additive manufacturing that involves the organized and specific placement of cells, biomaterials, and biochemical factors to recreate complex natural tissues and organs with micro-scale resolution [128]. The possibility of combining different cell types and biomaterials makes bioprinting particularly attractive for placental tissue engineering because the tissue is highly complex. Gelatin methacrylate (GelMA) is a natural inexpensive protein derived from hydrolysis of collagen which is highly biocompatible and biodegradable through enzymatic degradation and can be used for cell encapsulation[129-132]. With a reversible thermoplastic transition occurring around 20-30°C at 5-10 w/v %, GelMA is an ideal candidate for bioprinting[129, 133]. Gelatin can also be engineered for sustained drug release by tuning its electrostatic charges at physiological conditions [133]. To fabricate a biomimetic 3D model of the placenta, we must characterize the biophysical properties of the placenta. However, the dynamic mechanical properties of soft tissues such as the placenta are challenging to quantify. Previous studies on mechanical properties of biological tissues, such as brain [134], liver [135], and kidney [135], have demonstrated that mechanical

properties can be developed by applying curve-fitting techniques to experimental data obtained through conventional mechanical test techniques (e.g. dynamic mechanical testing (DMA)). However, this approach often requires the testing specimen to be uniform with a known geometry, which is difficult to achieve with placental tissue as its mechanical properties are inherently heterogenous [136]. Shear wave elastography (SWE) based on diagnostic ultrasound has emerged to be a powerful imaging technique for characterizing complex tissues and differentiating between soft and stiff tissues [8, 137, 138] that has several advantages over conventional mechanical testing techniques such as DMA. For example, measurements done by SWE are independent of the geometry of the specimen [8, 138]. Moreover, in contrast with conventional mechanical testing techniques, SWE can distinguish between hard and soft regions of a single specimen in a simple, rapid and minimally invasive manner which would allow real-time, not only *ex vivo* scans but also *in vivo* scans [8].

To this end, we hypothesized that a bioengineered placenta model (BPM) that captures the essential features of the decidua to model trophoblast invasion, particularly the tissue's ECM composition and mechanics as well as its growth factor-secreting vascular network, can be utilized to measure the effects of biochemical factors on trophoblast migration rate. We tested our hypothesis through the following three objectives. Our first objective was to characterize the biophysical properties of the placenta using SWE and develop a 3D printing platform that is able to recreate those properties. In addition, we confirmed that our bioprinting platform allows us to recreate the spiral geometry of the maternal vasculature through our 3D printing platform *in vitro*. The second objective was to bioprint a 3D bioengineered placenta model with appropriate cells, ECM, and growth factors.

Lastly, we aimed to test the efficacy of the BPM by evaluating the effect of epidermal growth factor (EGF) concentration on the migratory response of two types of cell populations that are present in the placenta (trophoblasts and human mesenchymal stem cells (hMSCs) [139, 140]). EGF was selected because the EGF family has been shown to play a major role in decidualization of the endometrium as well as the implantation and invasion of blastocysts by activation of the intricate signaling and transcriptional networks [141]. To accomplish these objectives, we first determined the stiffness of *ex vivo* placenta using SWE and developed a bioprinting platform based on GelMA. We then formulated our GelMA-based bioink to yield constructs with stiffness resembling that of *ex vivo* placenta. To ensure nutrients can diffuse through BPM, we used glucose as a model for nutrients and calculated its concentration profile. By studying the migratory behavior of BeWo cells, a trophoblast cell line that is widely used to study trophoblast migration[11, 29], in 2D and developing another diffusion model of EGF through GelMA, we decided on two EGF loading levels that are able to induce BeWo migration. We finally validated the efficacy of our placental model by successfully quantifying the 3D migration rates of trophoblast and hMSCs. To our knowledge, this BPM is the first *in vitro* placenta model that would enable study of the pathobiology of preeclampsia and development of novel treatment options. Even though the BPM presented here is a simplified model, it will serve as a significant step towards fabricating a more complex physiological placental model in later studies.

2.2 Materials and Methods

Cell Culture

BeWo cells were purchased from ATCC and cultured in Kaighn's Modification of Ham's F-12 Medium (F-12K; ATCC) with 15% (vol/vol) Fetal Bovine Serum (FBS; Thermo Fisher Scientific) and 1% penicillin/streptomycin (Pen/Strep; Thermo Fisher Scientific). Human mesenchymal stem cells (hMSCs) were kindly provided by Dr. Patrick Hanley of Children's National Health System. hMSCs were grown in high-glucose Dulbecco's Modified Eagle Medium (DMEM; Thermo Fisher Scientific) supplemented with 10% (vol/vol) FBS and 1% penicillin/streptomycin. All hMSCs used in this study were passage 5 or below.

Shear Wave Elastography & Ex vivo Placenta

A clinical diagnostic ultrasound system was used to quantify the mechanical properties of the *ex vivo* placenta and *in vitro* 3D printed GelMA construct. Specifically, SWE was performed using Aixplorer ultrasound system (Supersonic Imagine, Aix-En Provence, France) with a linear array transducer (SL 15-4), with 50 mm footprint and 256 elements. Duplex real-time SWE and b-mode imaging of the *ex vivo* placenta and GelMA were performed. The SWE window was placed on a portion of the placenta and the Young's modulus was measured within the window as heat maps (high (red) to low (blue) Young's modulus). Quantitative results of the Young's modulus will be measured by placing region of interest (ROI) within the window. The quantitative values of average Young's moduli in these ROIs were obtained and recorded for comparison and further analysis. *Ex vivo* placentas were collected from

MedStar Washington Hospital Center. All placentas were de-identified following the protocol IRB-2015-131 approved by the MedStar Research Institute Institutional Review Board.

Gelatin Methacrylate Synthesis

Gelatin methacrylate was synthesized according to previously published methods [129-131]. Briefly, Type A porcine skin gelatin (Sigma-Aldrich; 300 bloom) was mixed at 10% (w/v) into phosphate buffered saline (PBS; Thermo Fisher Scientific) at 50 ^{o}C for 20 minutes. Methacrylic anhydride (MA, Sigma-Aldrich) was added at the ratio of 0.6 g MA/g gelatin under rigorous stirring for an hour. The reactants were then diluted 2x with PBS to stop the reaction. The mixture was centrifuged, and the pellet was discarded. The supernatant was dialyzed against deionized water using dialysis cassettes (10kDa MWCO, Thermo Fisher Scientific) for at least 3 days at 50°C to remove salts and excess methacrylic acid. The dialyzed GelMA was then lyophilized and kept at -80°C for long-term storage.

Nuclear Magnetic Resonance

The degree of methacrylation was quantified using nuclear magnetic resonance (NMR) according to a previously described method [129, 132, 142]. Briefly, the composition of acid-treated porcine skin gelatin used for analysis of ^{1}H NMR data was acquired from previously published data. Spectra were collected at 50°C in deuterium oxide (Sigma) at a frequency of 600 MHz using a Bruker BioSpin GmbH spectrometer with a 5 mm BBI 1H probe.

2D Migration Study of BeWo Cells

To characterize the migratory behavior of BeWo cells in 2D, the surfaces of glass bottom dishes were treated with fibronectin (100 μg/mL; FN) from bovine plasma (Sigma) for an hour. BeWo cells were then seeded on top of the FN treated glass bottom dishes under different concentrations of recombinant epidermal growth factor (0-100 nM; EGF; Corning). Videos were then acquired using a fluorescent microscope over 20 hours with environmental chamber capable of humidity, temperature and CO_2 control. Image J software was used to trace the movements of BeWo cells every 10 minutes to quantify migration rate. BeWo cells were assumed to be moving linearly within the 10 minutes.

Diffusion Studies

Texas-Red-tagged EGF (Life Technologies) was mixed with the prepolymer (GelMA + photoinitiator) solution at a final concentration of 0.7 μM, and printed in the center of 3D printed GelMA constructs. Time-lapse fluorescent microscopic images were taken every 15 minutes for 6 hours to examine the diffusion of EGF within GelMA. The fluorescence intensity map was obtained by Image J software. A standard curve was created to convert intensity values to EGF concentration. Intensities were obtained starting from the edge of the circular EGF source (interface between EGF-loaded and EGF-free GelMA at time = 0) to a distance 700 μm from the source edge for four different time points (1, 2, 4, and 6 hr).

Diffusion models of EGF and Glucose in GelMA

The diffusion model developed in this study was based on the diffusion equation assuming 1D radial diffusion in cylindrical coordinates. For diffusion of EGF, we assumed a perfect source from the center of the disc and a no flux condition at the edge of the disc:

$D\frac{1}{r}\frac{\partial}{\partial r}\left(r\frac{\partial C_{EGF}}{\partial r}\right)=\frac{\partial C_{EGF}}{\partial t}$; C_{EGF}=0 μM @ t=0; C_{EGF}=13 μM @ r=0; $\frac{\partial C_{EGF}}{\partial r}$=0 @ r=1

For diffusion of glucose, we assumed a perfect source at the edge of disc from the surrounding media and a no flux condition at the center of the bioprinted placenta model:

$D\frac{1}{r}\frac{\partial}{\partial r}\left(r\frac{\partial C_{gluc}}{\partial r}\right)=\frac{\partial C_{gluc}}{\partial t}$; C_{gluc}=0 μM @ t=0; C_{gluc}=6 mM μM @ r=1; $\frac{\partial gluc}{\partial r}$=0 @ r=0

COMSOL and MATLAB were used to solve the partial differential equation to obtain the concentration profiles, which are then numerically integrated to obtain mass diffused as a function of time and position. Various mesh sizes were tested to ensure the computational model converges with stable output. This is demonstrated by the smooth curves and heat maps in **Figure 2.5** and **2.6**. The diffusion coefficient of EGF in GelMA was calculated to fit the raw data by minimizing the mean squared error between modeled and experimental results. The diffusion coefficient of glucose in GelMA is obtained from the literature [143].

Analytical solutions are available for this model, which is provided below as an example:

$\frac{\partial C}{\partial t}=D\frac{1}{r}\frac{\partial}{\partial r}r\frac{\partial C}{\partial r}$; C= C_o @ t = 0; $\frac{\partial C}{\partial r}$ = 0 @ r = 0; C = C_R @ r = 1

$$c(r,t) = \sum_{m=1}^{\infty} \frac{2(C_o - C_R)}{D_{m0} J_1(D_{m0})} e^{-D_{m0}^2 \frac{Dt}{R^2}} J_0\left(D_{m0} \frac{r}{R}\right) + C_R;$$

J_n= Bessel function of the first kind with n^{th} order

While analytical solution exists for our model, we decided to move forward with computational fluid dynamics for its convenience.

Swelling Ratio

To determine the swelling ratio, 3D-printed GelMA discs were incubated in PBS overnight at 37°C to completely swell the gel. After incubating in PBS, the mass of the swelled GelMA constructs were measured to obtain the wet mass. The swelled GelMA constructs were then dried in an oven at 50°C for at least 72 hours and weighed to obtain the dry mass. The swelling ratio was calculated using the formula swelling ratio = (wet mass – dry mass)/wet mass.

Dynamic Mechanical Analysis

Dynamic mechanical testing was carried out using a Q800 DMA testing machine. To determine the Young's modulus of printed GelMA, cylinders 10 mm in diameter and 2 mm in height were fabricated using an extrusion-based bioprinter (3D-Bioplotter; EnvisionTEC; Germany). This size was chosen to reduce the fabrication time to ensure that the hydrogels did not dehydrate during the printing process. In all cases, the hydrogels were treated with a preload of 0.001 N prior to mechanical testing. For DMA testing, samples were tested using a strain sweep with a fixed frequency (1 Hz) to determine the stress-strain curve and the Young's modulus.

Bioprinting of Simplified, Cell-laden Bioengineered Placenta Model

All bioprinting work was completed using an extrusion-based bioprinter (3D-Bioplotter; EnvisionTEC; Germany). To prepare the prepolymer solution, lyophilized GelMA was dissolved in PBS at 50°C for 10 minutes. Photoinitiator (2-hydroxy-1-(4-(hydroxyethoxy)phenyl)-2-methyl-1-propanone; Irgacure 2959; BASF) was then added into the GelMA solution at a concentration of 0.1% (w/v) at 50°C for 15 minutes. The prepolymer solution was loaded into the low-temperature printer head and allowed to equilibrate for 30 minutes at a desired temperature. Additional biomaterials such as ECM, cells, and/or growth factors of interest were added at this point, and the functionalized prepolymer solution was incubated for another 30 minutes prior to printing. Printed constructs were UV-cured for 30 seconds (0.09 mW/cm^2) using a UV box (VWR). A calcein-AM/ethidium homodimer, Live/Dead assay (Life Technologies) was used to assess cell viability within printed constructs according to the manufacturer's instructions.

Cell Migration Studies

BeWo cells were encapsulated in GelMA-FN to print the cylindrical bioengineered placenta model at a concentration of 10^7 cells/mL. For the migration experiments, cells were printed along the periphery of the cylindrical bioengineered placenta model and EGF was printed in the center (**Figure 2.1**). Cells were cultured in growth media with low serum concentration (5%) and phase-contrast images were taken every 2 days for up to 8 days. The distances between the edge of the

bioengineered placenta model and the migration front was measured and averaged over time to obtain migration rates.

Statistical Analysis

Data from all the studies were analyzed using ANOVA and multiple comparison tests using MATLAB. A significance level of 95% was chosen, and a p-value less than 0.05 were considered to indicate a significant difference between samples.

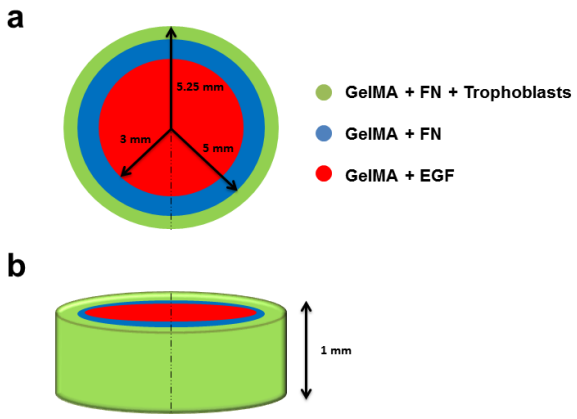

Figure 2.1: **Bioprinted Placenta Model**. This simplified placenta model was based on a cylindrical GelMA hydrogel loaded with varying components at different radial positions. A ring of trophoblasts was encapsulated and printed along the periphery of model (green). A chemoattractant, EGF, was printed in the center (red) of the construct, and diffused outwards and thus established a radial concentration gradient. Due to this concentration gradient, trophoblasts migrated towards the center. **(a)** Top view of the bioprinted placenta model. **(b)** Side view of the bioprinted placenta model.

2.3 Results

2.3.1 Development of a GelMA-based Bioprinting Platform

We began developing our bioprinting platform by synthesizing GelMA. Specifically, type A porcine gelatin was reacted with methacrylic anhydride at 0.6 g MA /g of gelatin. The number of methacrylate groups was verified by ^{1}H NMR and showed a degree of substitution of 63.1 ± 5.75% (**Figure 2.2a**). We then formulated our bioink by mixing GelMA (5 or 10% (w/v)) with Irgacure 2959 (0.1% (w/v)), and optimized the bioprinting parameters to maximize resolution (**Figure 2.2b,c)**. Due to its higher viscosity, 10% GelMA hydrogel was printed at a higher pressure and temperature compared to those of 5% GelMA (28 ^{o}C vs. 23 ^{o}C, 0.7 bar vs. 0.5 bar, respectively). In addition, the strands produced by 10% GelMA are also slightly larger than those produced by 5% GelMA, which reuslts in higher layer thickness and interstrut distances to create solid constructs. We also demonstrated our ability to print solid structures (**Figure 2.2d**) and spiral patterns using a blue dye (**Figure 2.2e-h**). In addition, the swelling ratio of GelMA was investigated, wherein all were greater than 0.95 with no significant differences between 5% and 10% GelMA (data not shown). Furthermore, we measured the Young's modulus of our 3D printed GelMA with 5% and 10% GelMA concentrations through dynamic mechanical analysis (DMA), which were 5.35 ± 0.66 kPa and 7.74 ± 0.26 kPa respectively (**Figure 2.2k**). We also measured the stiffness of 5% GelMA using both SWE and DMA (**Figure 2.2k**) and demonstrated no significant differences between the two sets of collected data. However, when we performed multiple comparison tests between the Young's modulus between the decidua, 5%, and 10% GelMA, we found no

significant differences between 5% and 10% GelMA. Therefore, we decided to move forward with 5% GelMA because the stiffness is within the same order of magnitude as the native tissue with more superior biological responses than the 10% GelMA.

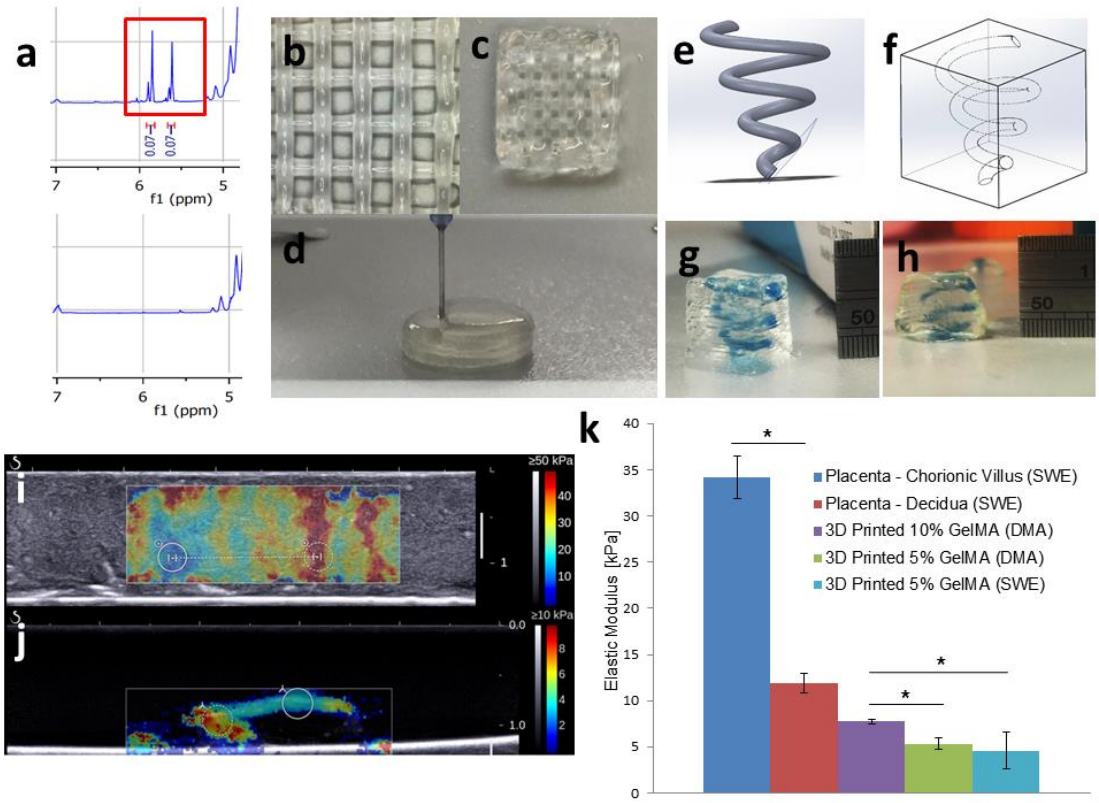

Figure 2.2: Characterization of GelMA Printing Platform and *Ex Vivo* Placental Tissue. **(a)** NMR results for gelatin methacrylate (n = 3). Successful methacrylation was confirmed by the peaks at around 5.7 and 5.9 ppm (top, red box), which does not appear in NMR results for gelatin control (bottom). **(b,c)** Lattice structures with 1×1mm spacing. **(d)** Solid disc structure (D = 10 mm). **(e)** CAD model for spiral (height: 10 mm, channel diameter: 1mm, pitch: 3 mm, taper helix angle: 20°, 3 revolutions. **(f)** Overall CAD model used for 3D printing**:** spiral embedded in a cube. **(g)** 3D printed spiral (blue) in a cube (transparent): side view. **(h)** 3D printed spiral (blue) in a cube (transparent): cross-sectional view. **(i)** Transverse imaging plane of a term placenta. The rectangular box represented the stiffness within the region where blue represented relatively soft tissues and red represents relatively stiff tissues. The solid (cotyledons) white and dotted (chorionic villus) circle represented ROI based on the anatomy of the placenta, with mean elastic modulus measured as 12 kPa and 43.9 kPa, respectively. **(j)** The transverse imaging plane of a printed GelMA disc (similar to **Figure 2d**). The rectangular box represented the stiffness within the region where blue represented relatively soft tissues and red represented relatively stiff tissues. **(k)** Elastic modulus of *ex vivo* placental tissue (n = 3) and 3D Printed GelMA (n = 6). Error bars indicated standard deviation and * indicated statistically significant differences between groups ($p<0.05$).

2.3.2 Characterizing the Diffusion of Epidermal Growth Factor (EGF) and Glucose in Bioprinted Placenta Model

To decide on the type and dosage of soluble factors and ECM that should be printed to functionalize our BPM, we performed time-lapse microscopy of BeWo cells on fibronectin (FN)-coated glass treated with different concentration of EGF (0-100 nM) for 20 hours (**Figure 2.3**). Our results demonstrate that the BeWo cells migration rate increases in response to higher EGF concentration in a dosage-dependent manner on 2D FN-coated glass (**Figure 2.3e**). Based on these results, we decided on the range of EGF concentrations between 0-100 nM to be used in our BPM. In addition, we decided to infiltrate the BPM with fibronectin (50 μg/mL), an ECM protein that is highly expressed in the placenta [144]. To verify that a chemotactic gradient of EGF can be established to induce chemotaxis of BeWo cells, we characterized the diffusion of EGF through the 3D printed GelMA. Over the course of 6 hours, red fluorescent EGF emanated from the perimeter of the inner circle providing a spatial gradient field over the micrometer-size scale (**Figure 2.4a-d**). Using a standard diffusion equation, we constructed a model that estimates the mass of EGF diffused as a function of time using MATLAB. The diffusion coefficient of EGF in GelMA was calculated to be 2.5×10^{-8} cm^2/s, which was done by minimizing the mean squared error between the predicted and experimental results (**Figure 2.4f**). We then used the optimized diffusion coefficient to model the concentration profile of EGF in GelMA at different time points which demonstrates that the concentration gradient between the EGF source and the cells remains throughout 8 days (**Figure 2.5, 6a**). Considering the diffusion model and 2D BeWo

migration results, we decided to use a loading level of 6 and 13 μM EGF for subsequent studies. As shown in **Figure 2.5c**, we expected the BeWo cells to sense the presence of EGF by Day 3, when the local EGF concentration along the edge of the disc where the cells are located had reached our regime of interest (0.1 μM) as determined in 2D migration results. To ensure the cells embedded in the BPM receive sufficient nutrients, we have modeled the concentration profile of glucose in GelMA at different time points (**Figure 2.6b**). The diffusivity of glucose in hydrogel was obtained from the literature [143]. Our results demonstrate that the glucose concentration will be homogenous in BPM by 32 hours while there is still a significant concentration gradient of EGF (**Figure 2.6c,d**).

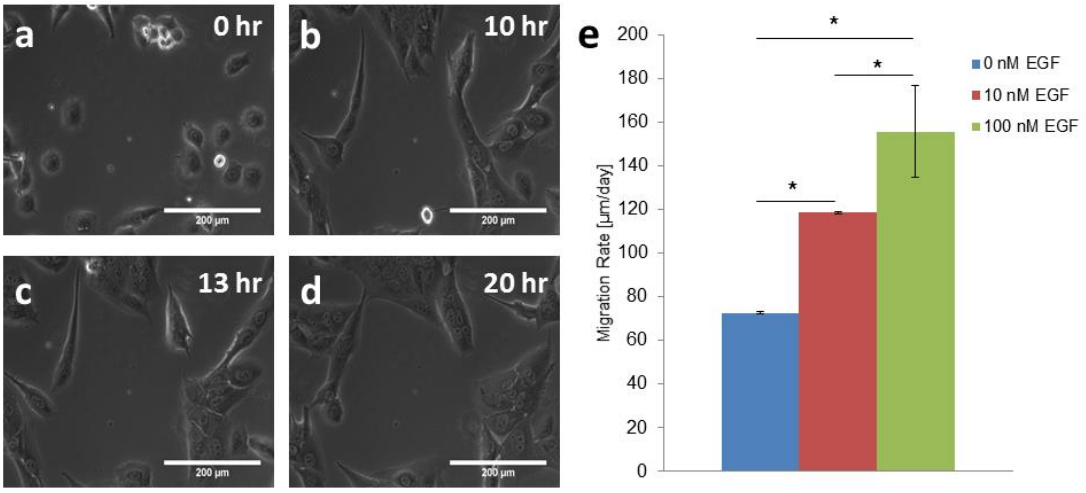

Figure 2.3: 2D Characterization of the Effect of EGF on the Migratory Behavior of BeWo cells. (a-d) Representative microscopy images of BeWo cells with 100 nM of EGF in the media. Cells appeared to have proliferated and elongated after 20 hours (scale bars = 200 µm). **(e)** 2D migration rate of BeWo as a function of EGF concentration. Migration rates were measured by tracking individual cells in microscopy video over 20 hours. Error bars indicated standard errors and * indicated statistically significant differences between groups ($n>30$, $p<0.05$).

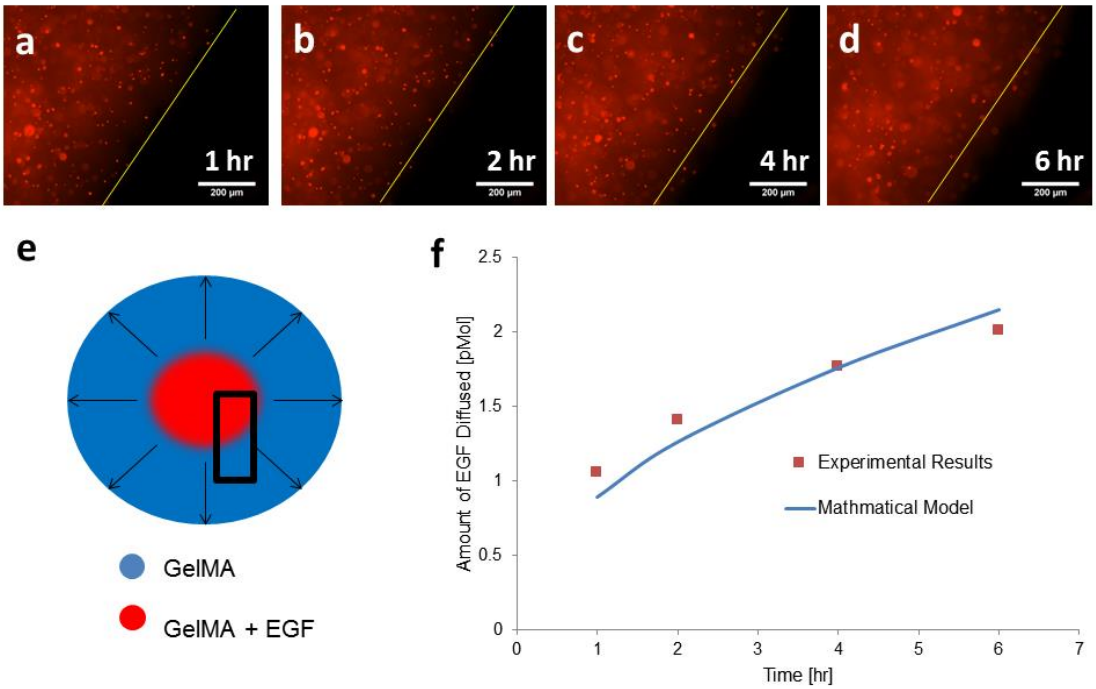

Figure 2.4: Transport of Phenomena of EGF in 3D Printed GelMA. **(a-d)** Time lapse images Texas red-tagged EGF diffusing radially from the center of the 3D-printed GelMA discs dosed at 0.7 µM (scale bars = 200 µm). **(e)** Design of the diffusion study. Blue indicated GelMA region and red indicates GelMA loaded with EGF. Black box indicated where the time lapse images were taken. **(f)** Diffusive flux of EGF as a function of time obtained through integrating concentration profiles from experimentations and mathematical models.

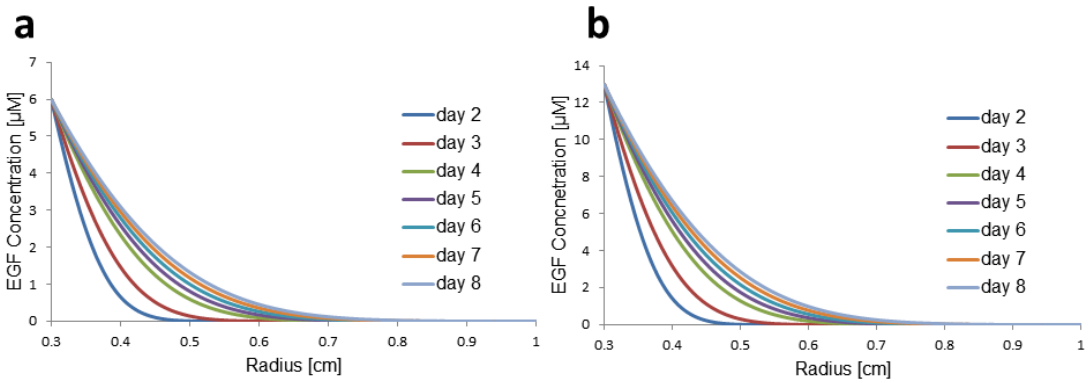

c

Source Concentration [µM]	day 2	day 3	day 4	day 5	day 6	day 7	day 8
6	0.01	0.14	0.59	0.81	1.00	1.17	1.32
13	0.02	0.31	1.29	1.75	2.16	2.53	2.86

Figure 2.5: Mathematical Model Results of EGF Diffusion in GelMA. **(a)** Concentration profile of EGF as a function of radius and time with a perfect source of 6 µM. **(b)** Concentration profile of EGF as a function of radius and time with a perfect source of 13 µM. **(c)** EGF concentration at radius of 5 mm, where the cells would be printed, as a function of time.

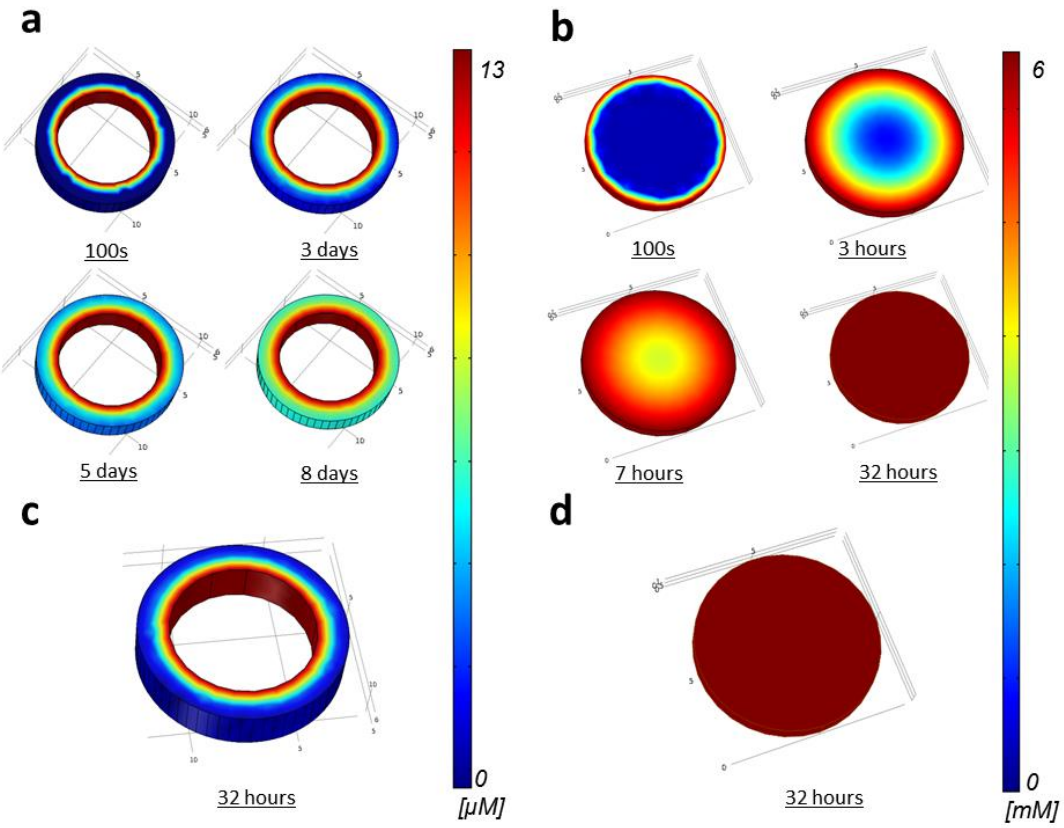

Figure 2.6: Concentration Profiles of EGF and Glucose in BPM. (a) Diffusion of EGF in GelMA over 8 days. The EGF was diffusing out from the center source (13 μM) of the disc outwards radially towards the edge of the disc where the cells were located. The distance between the EGF source and the cell was 0.25 mm. The concentration of EGF at the edge of the disc (where the cells were located) reached target concentration (0.1 μM) at around 3 days. The concentration gradient between the EGF source and the cells remained over 8 days. Scale represented concentration of EGF in μM. **(b)** Diffusion of glucose in GelMA in 32 hours. In this model, glucose, which served as a model for the nutrients coming from the surrounding media, was diffusing from the edge to the center of the BPM. Our results demonstrated glucose concentration would be homogenous within the disc in 32 hours. Scale represented concentration of glucose in mM. **(c)** EGF concentration profile at 32 hours **(d)** Glucose concentration profile at 32 hours**.** At 32 hours, glucose reached equilibrium (glucose concentration gradient is less than 0.1%) while the concentration differences between the cell and the EGF source was at least an order of magnitude

2.3.3 Bioprinting of the Simplified Bioengineered Placental Model (BPM)

Based on the results above, we designed and bioprinted the BPM (**Figure 2.1**). We measured the distance between the edge of the BPM and the migration front of the trophoblast cells at regular intervals for 8 days (**Figure 2.7a**, red arrows). We then used the average distance over time and successfully quantified migration rate (**Figure 2.7b**). We demonstrated the migration of trophoblasts by comparing microscopy images between Day 2 and Day 8 (**Figure 2.7a**, left column, scale bar = 200 μm). Day 2 was selected as a reference time point to allow the printed hydrogel to reach equilibrium with the surrounding media before measuring migration. As shown, there seems to be a dosage-dependent migratory response of trophoblasts towards EGF, where higher concentration of EGF results in larger trophoblastic migration rates which correlates well with our 2D results. The average migration distance of BeWo cells towards 6 μM and 13μM over 8 days are 52 μm and 101 μm, respectively. The EGF concentration depicted in the legend of **Figure 2.7b** indicates the loading level of EGF at the center of the BPM at t = 0 (red in **Figure 2.1**). We have also confirmed excellent viability (>90 %) of printed BeWo cells via live/dead staining after 8 days of culture (**Figure 2.7c, d**). To further demonstrate the validity of the BPM, we quantified migration of human mesenchymal stem cells (hMSCs), another cell population present in the decidua that has been demonstrated to promote trophoblast invasion[139, 140], using a similar approach (**Figure 2.8**). Similar to trophoblastic migration, we observed a dosage-dependent response of hMSC migration towards EGF (**Figure 2.8b**), which agrees with previous literature [145]. The average migration distance of hMSCs towards 6 μM and 13μM over 8 days are

993 μm and 1146 μm respectively. We have also confirmed excellent viability (>90 %) of printed hMSCs via live/dead staining after 8 days of culture (**Figure 2.8c, d**).

Herein we report the first 3D printed, *in vitro* bioengineered placenta model that can be used for to study preeclampsia. We have demonstrated that the biophysical properties, the placement of the biomaterials, and the chemotactic gradients of BPM can be engineered to better mimic those of the native tissue, which has never been demonstrated before in trophoblast biology.

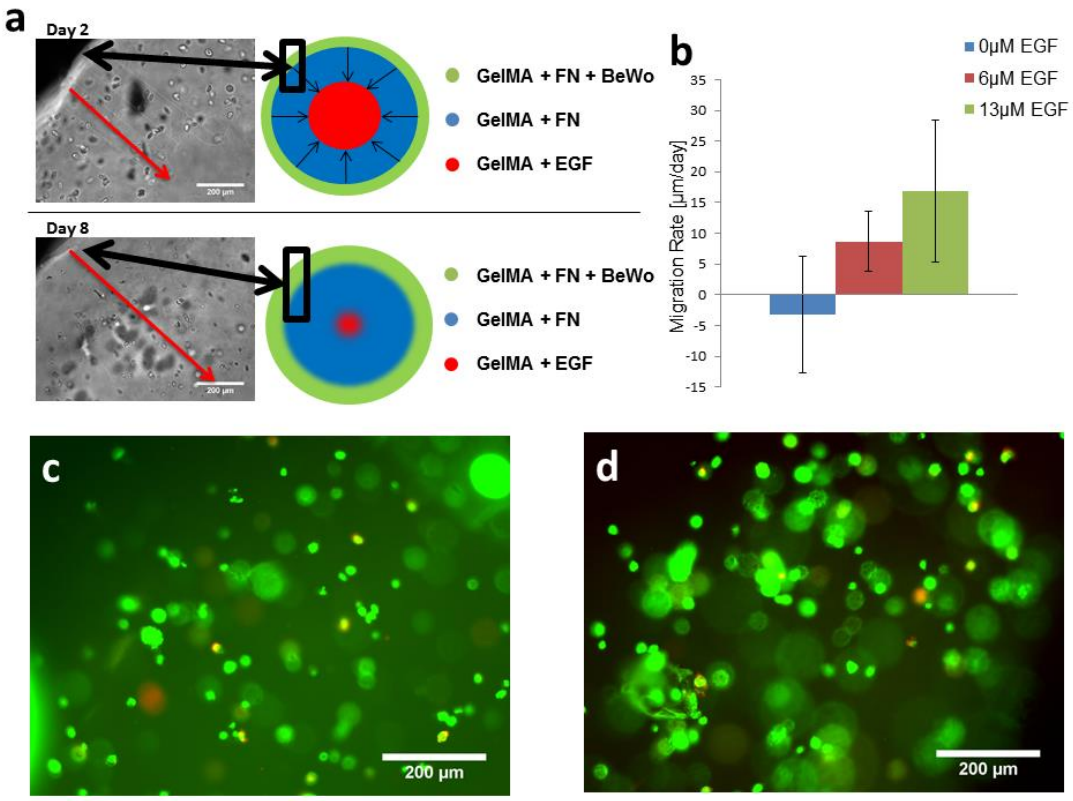

Figure 2.7: Results from the Trophoblast Migration Model. (a) Overall model design and representative microscopy images at day 0 and day 8 showing trophoblast migration (Scale bars = 100 μm). **(b)** Migration rate of BeWo cells under different concentration of EGF, which demonstrated a dosage-dependent migratory response of trophoblasts towards EGF. **(c,d)** Fluorescent live/dead stain images taken at Day 8 indicating excellent viability of BeWo cells (scale bars = 200 μm).

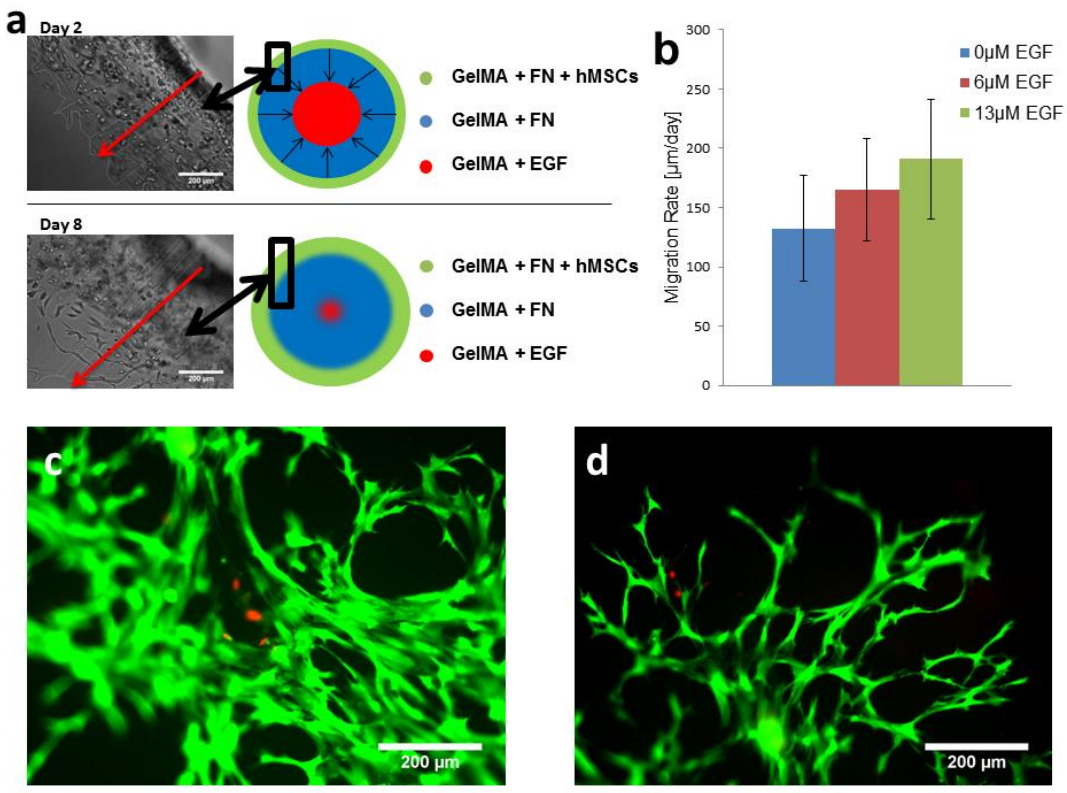

Figure 2.8: Results from the hMSC Migration Model. (a) Overall model design and representative microscopy images at day 0 and day 5 showing hMSC migration (scale bars = 200 μm). **(b)** Migration rate of hMSCs under different concentration EGF, which demonstrated a dosage-dependent migratory response of hMSCs towards EGF. **(c,d)** Fluorescent live/dead stain images taken at Day 8 indicating excellent viability of hMSC. (scale bars = 200 μm).

2.4 Discussion

Despite the efforts to better understand the pathogenesis of preeclampsia, no effective treatment is available today other than early delivery of the fetus and placenta prematurely due to the lack of effective *in vitro* models [9]. Current *in vitro* models that are used to study trophoblast invasions are 2D, which lack the complex elements of the decidua (maternal vasculature, heterogeneous cell populations, extracellular matrix, and biochemical signals) [11], which play essential roles in trophoblast migration.

To this end, we developed a 3D printing platform that is able to fabricate tissue engineered constructs with biophysical properties that closely mimic those of the placenta. We began by characterizing the stiffness of *ex vivo* term placenta using SWE. Utilizing SWE, we could successfully distinguish between the maternal decidua and the fetal villi, and measured the Young's modulus of maternal decidua where trophoblast migration occurs (11.84 ± 1.05 kPA, **Figure 2.2i**). If we were to use DMA, we would have to manually separate the placenta into respective parts, which would be cumbersome and could introduce bias. After obtaining the stiffness of regions of interest from characterizing *ex vivo* tissues, we then 3D printed 5% and 10% GelMA constructs and measured the Young's modulus through DMA, the current gold standard of evaluating mechanical properties. The Young's modulus in 5% and 10% GelMA were found to be similar to that of maternal decidua (**Figure 2.2k**). The swelling ratio of both 5% and 10% GelMA were greater than 0.95, which indicates that they allow for diffusion of nutrients that is essential for cell encapsulation. To verify that the results from SWE and DMA are comparable, we

tested the Young's modulus of 3D printed GelMA constructs using both methods and found no significant differences between the values (**Figure 2.2k**). Since it has been demonstrated in previous studies that cells elongated and migrated more in 5% GelMA hydrogels compared to those of GelMA hydrogels at higher polymer concentrations (10 and 15 % (w/v))[142], and that the stiffness of 5% GelMA is within the same order of magnitude as that of native tissue, we decided to move forward with 5% GelMA. We expect the trophoblasts embedded in GelMA will remodel their ECM overtime to achieve physiological stiffness in our BPM. In the future we plan on investigating the effect of matrix mechanics on trophoblast migration. To confirm our printing platform can recapitulate the complex maternal vasculature, we have printed constructs which include an inner spiral geometry (**Figure 2.2e-h**). We will evaluate the effect of vasculature geometry on trophoblast migration in later studies.

After developing the biomaterial and printing platform that captures the biophysical properties of the maternal decidua, we aimed to 3D print a bioengineered placenta model with appropriate cells, ECM, and growth factors based on bioprinting technologies to assess cell migration (**Figure 2.1**). The BPM is based on a cylindrical gelatin methacrylate hydrogel, a highly biocompatible and biodegradable biomaterial [129-132, 146], loaded with varying components at different radial positions. To decide on the dosage of EGF, we measured the migration rate of BeWo cells on 2D fibronectin-coated glass through time-lapse microscopy (**Figure 2.3**). The results demonstrated a dosage-dependent response where higher EGF concentration leads to significantly higher migration rate. Through the 2D migration experiments, we've

identified the physiologically relevant concentration range of EGF to that can induce trophoblast migration, and we would like to replicate the concentration in the BPM. To accomplish this, we characterized the transport phenomena of EGF through GelMA (**Figure 2.4a**) through time-lapse images of fluorescently-tagged EGF. By using a standard diffusion equation, we used MATLAB to calculate a diffusion coefficient of EGF in GelMA to be 2.5×10^{-8} cm^2/s, which resulted from the least mean squared error between the experimental and model results. The diffusion coefficient is lower than the effective diffusion coefficient of EGF through murine soft tissue[147]. We believe this is mainly due to the electrostatic interactions between GelMA and EGF, as type A gelatin and EGF carry opposite charges in physiological conditions[133, 147]. We then used the optimized diffusion coefficient to model the concentration profile for 8 days (**Figure 2.5, 2.6**). We then decided on the loading level of 6 and 13 μM that results in physiological relevant level of EGF at the location of the cells by day 3 (**Figure 2.5**). We believe these loading levels will result in an EGF concentration profile to induce trophoblast migration within 8 days. To investigate the diffusive fluxes of nutrients and EGF within BPM, we evaluated and compared the magnitudes between the two opposing gradients caused by the 1) nutrients diffusing from the edge towards the center of BPM and 2) EGF diffusing from the center of the towards the edge of the BPM. Using glucose as a model, our results showed that the concentration of nutrients will be homogenous throughout the construct in just 32 hours, whereas the determined concentration gradient at that time is at least an order of magnitude different (**Figure 2.6c, d**). We are confident that the effect of the nutrient gradient provided by the surrounding media can be neglected

because 1) small molecules such as glucose or fructose will be homogeneously distributed in BPM within 1.5 days (**Figure 2.6b**) and 2) concentration of larger molecules such as proteins and growth factors in the surrounding media is six orders of magnitude lower than our printed EGF source [48, 148-152] (pico- vs micro-, respectively). Overall the evolution of concentration gradients and the development of a diffusion model demonstrate that concentration of biomolecular species changed with time in a predictable manner which can be controlled and engineered to develop 3D migration models.

Once we identified the parameters needed to bioprint the BPM, we tested the validity of the BPM by confirming the chemotactic effect of EGF on trophoblasts and hMSCs quantitatively (**Figures 2.7, 8**) [141] . Our results indicated a dosage-dependent migratory response of trophoblasts towards EGF in a 3D matrix. These results demonstrate that EGF is a potential therapeutic agent for preeclampsia by directly promoting trophoblast invasion, which agrees with other published work [29]. To further validate the BPM, we tested migration of hMSCs, another cell population that is present in the placenta, towards EGF. Our results indicated a dosage-dependent migratory response of hMSCs towards EGF in a 3D matrix. This result suggests that EGF can indirectly treat PE by recruiting hMSCs from the maternal side to the site of trophoblast invasion, as hMSCs have been shown to alleviate symptoms of PE *in vivo [139]* and to have enhanced the migration and invasion abilities of trophoblast cells *in vitro [140]*.

To the best of our knowledge, the BPM developed herein is the first 3D *in vitro* model that captures the stiffness of decidua and contains a controlled gradient of

chemokines to induce trophoblast and hMSC migration. Such unique and clinically critical biophysical information as tissue elasticity and chemotactic gradient has not been previously incorporated to build a functional tissue model for study of disease and treatment development. Even though our BPM is a simplified model of the trophoblastic invasion, the methodology of utilizing SWE, diffusion modeling, and finally 3D printing to build a tissue model to study trophoblast migration will serve as a platform for developing more complex, physiological placental models in future studies. The current BPM allows the researcher to evaluate bulk population migration and in the future, we would like to improve the placenta model to track single cell migration including rate and direction. We believe our bioengineered placenta model will serve as a platform that will continue to shed light on placental biology and allow researchers to develop novel treatments for preeclampsia. Unlike current *in vitro* models, such as transwell permeable supports, the BPM can allow for the quantification of migration rates of different placental cell populations through 3D extracellular matrix, which is a significantly more realistic representation of the *in vivo* environment compared to current 2D models. While this work centers itself in the theme of placental tissue engineering to study preeclampsia, we foresee utilization of our tissue modeling approach to study cell migration in other contexts such as migration of fibroblasts in wound healing and/or stem cell homing to site of injuries.

2.5 Conclusion

In this work we have successfully developed the first 3D printed, bioengineered placenta model to study and quantify trophoblast and hMSC migration. We have developed the BPM by using SWE to characterize the stiffness of native

tissue, have modeled the diffusion of chemokines as well as nutrients, and finally have used bioprinting technology to fabricate a placenta model with spatial control of cells, growth factors, and ECM. To demonstrate the efficacy of our bioengineered placenta model, we evaluated the effect of EGF on 3D trophoblast migration and found a positive relationship between EGF dosage and trophoblast and hMSC migration rates. These results suggest that the EGF can directly treat PE by promoting trophoblast migration and indirectly treat PE by recruiting hMSCs from the maternal decidua. This work is a first step towards building a more sophisticated bioengineered placenta model that will be a powerful tool for researchers to test and to develop novel treatments for preeclampsia. We envision that our tissue modeling approach presented in this work will not only be used to explore trophoblastic migration in the context of preeclampsia, but also in other processes such as migration of fibroblasts in wound healing and/or stem cell homing to the site of injuries.

Chapter 3: Placental Basement Membrane Proteins are Required for Effective Trophoblast Invasion

3.1 Introduction

In normal pregnancy, embryo implantation and placentation occur by trophoblast invasion of the maternal spiral arteries to create a low-resistance, high-flow maternal uteroplacental circulation [6, 9, 121, 122]. Impaired trophoblast invasion of the maternal spiral arteries results in abnormal placentation leading to reduced placental perfusion and oxidative stress [6, 9, 52, 121, 122]. One of the major clinical complications of impaired trophoblast invasion is preeclampsia (PE) [16]. PE is a leading cause of maternal and perinatal morbidity and mortality affecting 3 to 8% of all pregnancies [6, 9, 107, 121, 124] and resulting in 29,000 deaths yearly in US [153]. The only treatment option for PE available is the premature delivery of baby and placenta because the mechanisms of trophoblast invasion are poorly defined [6, 9, 11].

In early placental development, trophoblasts differentiate and lose their organized epithelial phenotype and transitioning to a more migratory and invasive mesenchymal phenotype which allows them to infiltrate the maternal decidua and spiral arteries. This transition has been recently suggested as a type of epithelial-mesenchymal transition (EMT) that involves upregulating and secreting matrix metalloproteinase (MMP) and gaining the ability to migrate and invade [31-34, 37]. EMT has been reported to be mediated by tyrosine kinase receptors (TKR) and TGF-β family[33-35]. Among these receptors, TKR appears to have a direct and specific

impact on endometrial susceptibility to implantation *in vivo* based on a murine TKR-ablated uterus model (EGFR knock-out) [51]. Moreover, EMT is mediated through the action of PI3K signaling pathway [33, 35], a major signaling pathway located downstream of TKR that regulates cellular processes including motility, proliferation, survival and growth– which are critical for trophoblast invasion [52, 55, 60]. However, the effect of extracellular matrix (ECM) microenvironment on EMT and PI3K signaling on trophoblast invasion remains poorly understood.

Cell-ECM interactions play a fundamental role in the growth, differentiation and invasion of trophoblasts [120]. Prior to implantation of blastocysts, the maternal endometrium undergoes substantial remodeling and differentiation to become decidua, a process known as decidualization [51, 154]. When decidualization occurs, the maternal decidual stromal cells (those in direct contact with trophoblasts) produce pericellular basement membrane (BM) proteins that are critical to placental development and successful embryogenesis. For example, knocking out laminin genes in murine models cause embryonic lethal outcomes (Lama1; Lama5; Lamb1; Lamc1) and considerable abnormalities in vascular and trophoblast differentiation during placental development (Lama5) [155, 156]. These placental abnormalities are potentially caused by the lack of stable adhesion between trophoblasts and Lama5-deficient murine. Moreover, human term placenta from preeclamptic pregnancies have lower expression levels of laminin compare to those of normal pregnancies [157-159]. The expressions of laminin alpha 2 appears to also be downregulated in the basal plate of preeclamptic term placenta [160]. Even though these evidences implicate the vital role of BM proteins in placentation and trophoblast invasion, the

majority of published literature focuses on the effect of soluble factors [120]. The intricate and highly ordered nature of ECM makes it difficult to reproduce using synthetic or purified components and these BM-proteins are often tissue-specific and work in concert instead of individually [120, 156, 161]. These differences in ECM compositions between native tissue and *in vitro* culture techniques affect cellular genotypes and phenotypes [120]. Therefore, studies on cell invasion utilizing single ECM components, while still valuable, may not represent the *in vivo* environment.

Our hypothesis is that placental BM proteins from basal plate of human placenta (pECM) are required for effective trophoblast invasion. To test this hypothesis, we isolated and characterized pECM from the basal plate of term human placenta. Through proteomics, we determined that more than 80% of pECM consists of BM proteins. Our results show that the addition of isolated placental BM proteins in pECM substantially increased the invasion rates by 13-fold while significantly upregulated the gene expressions of MMP2 and MMP9 (surrogate markers for invasion and EMT [55, 162]). The addition of LY294002, a well-established PI3K inhibitor [52, 60], significantly reduced the enhanced invasive rates and expressions of MMP2 and MMP9. These results demonstrated that the placental BM proteins stimulated trophoblast invasion predominantly through PI3K signaling - first direct evidence indicating that the trophoblast differentiation and invasion are critically modulated by their surrounding ECM microenvironment.

3.2 Materials and Methods

Cell Culture

BeWo cells were purchased from ATCC and cultured in Dulbecco's Modified Eagle's Medium (DMEM, ATCC), 15% (vol/vol) Fetal Bovine Serum (FBS; Thermo Fisher Scientific), and 1% penicillin/streptomycin (Pen/Strep; Thermo Fisher Scientific).

Tissue Collection and Isolation

Ex vivo placentae were collected from MedStar Washington Hospital Center according to protocol approved by the MedStar Research Institute Institutional Review Board (IRB# 2015-131). The placentas are frozen at -80 immediately after delivery until tissue isolation. Surgical tools (e.g. scissors, scalpels, forceps) were utilized to carefully harvest the top slice of the placenta from the maternal side (no more than 3 mm). The isolated tissue is then minced and washed using until the effluent become clear.

Decellularization and Digestion of Basal Plate

The decellularization and digestion protocols are developed based on previous studies[161, 163].The minced tissues are treated with 1% (v/v) antibiotic/antifungal (Thermo Fisher Scientific) and place on a shaker overnight at room temperature. The tissue is then treated in 0.1% Sodium Dodecyl Sulfate (SDS) in dH_2O for 48 hours to decellularize the tissue. Following SDS treatment, the tissue is washed in distilled water for another 48 hours and lyophilized. The lyophilized, decellularized tissue is

crushed using a mortar and pestle set and digested in pepsin (1g of pepsin / 10 g of dry tissue) in 0.5M acetic acid in 4 ^{o}C for 48 hours. The pH of the tissue digest is adjusted to 7.4 using an aqueous base solution (e.g. NaOH) and then centrifuged at 3000 g for 5 mins. The supernatant is filtered using a cell strainer (100 µm) and stored at -80 until further use.

Gelatin Methacrylate Synthesis

Gelatin methacrylate was synthesized according to previously published methods[129-131]. Briefly, Type A porcine skin gelatin (Sigma-Aldrich; 300 bloom) was mixed at 10% (w/v) in phosphate buffered saline (PBS; Thermo Fisher Scientific) at 50 ^{o}C for 20 minutes. Methacrylic anhydride (MA, Sigma-Aldrich) was then added at 0.6 g of MA / g gelatin under rigorous stirring for an hour. The reactants were then diluted 2x with PBS to stop the reaction. The mixture was centrifuged, and the pellet was discarded. The supernatant was dialyzed against deionized water at 50°C using dialysis cassettes (10kDa MWCO, Thermo Fisher Scientific) for at least 3 days. The deionized water was changed twice a day to remove salts and excess methacrylic acid. The dialyzed GelMA was then lyophilized for at least 3 days and store at -80°C until further use.

Proteomics

The digested ECM sample was dissolved in SDS-loading buffer and separated by size using a 10% acrylamide gel by SDS-PAGE. The gel was then fixed and cut into 10 pieces for proteomics analysis. Briefly, the proteins in gel bands were

digested with sequencing grade Trypsin (Promega) and the resulting peptides were extracted with acetonitrile-formic acid buffer. The peptide mixtures from each band were sequentially analyzed by liquid chromatography-mass spectrometry (LC-MS) using nano-LC system (Easy nLC 1000, Thermo Fisher Scientific) connected to Q Exactive mass spectrometer (Thermo Fisher Scientific). The peptides were eluted at a flow rate of 300 nL/min using linear gradients of 2-25 % Acetonitrile for 35 min, followed by 25-40% for 10 min, 40-60% for 1 min, and static flow at 60% for 14 min. The MS raw data were searched against UniProt database that also included common contaminants using MaxQuant software (version 1.5.5.1).

Size Exclusion Chromatography (SEC)

250µL of digested placenta sample (prepared as specified above) were loaded onto a ENrich™ SEC 650 column (Bio-Rad) using the NGC Quest™ 10 chromatography system (Bio-Rad) which was equilibrated with 1x PBS. Proteins were eluted from the column using 1x PBS as mobile phase at a flow of 1mL min^{-1} while monitoring the absorbance at 280nm. Samples were collected in 0.7mL fractions using a fraction collector (BioFrac™, Bio-Rad) and frozen at -20°C until further use.

Cell Adhesion Study

Adhesion of trophoblasts to pECM was evaluated using the washing assay. This assay relies on seeding cells onto substrates of interest and washing off 'nonadherent' cells with physiological buffers and then counting the remaining

cells[1-3, 164]. Briefly, a 24 well plate (not tissue culture treated, Corning) was first treated with FBS for 2 hours and then coated with desired ECM overnight, both at 4ºC. Trophoblasts were stained with Calcein AM (Thermo Fisher Scientific) following manufacturer's recommendations and seeded on the treated cell culture wells in culture media. The cells were allowed to adhere for 2 hours at 37 ºC and then an initial fluorescent readings (F1) was taken using a fluorescent plate reader. Then the wells were washed twice with PBS to remove non-adherent cells and the fluorescence was read again (F2). Fraction of adhesion (FA) was calculated using the formula: FA= 1 - (F1-F2)/F1.

Bioprinting of Placenta Model with pECM

All bioprinting work was completed using a commercial bioprinter (3D-Bioplotter; EnvisionTEC). To prepare the prepolymer solution, lyophilized GelMA was dissolved in complete growth media at 50°C for 20 minutes. Photoinitiator (2-hydroxy-1-(4-(hydroxyethoxy)phenyl)-2-methyl-1-propanone; Irgacure 2959; BASF) was then added into the GelMA solution at 0.1% (w/v) at 50°C for 15 minutes. The prepolymer solution was loaded into the low-temperature printer head and allowed to equilibrate for 30 minutes at 37°C. Additional biomaterials such as pECM, cells, and/or growth factors of interest were added at this point, and the functionalized prepolymer solution was loaded into printing cartridge and allowed to equilibrate to printing temperature (e.g. ~23°C) for another 30 minutes prior to printing. Printed constructs were UV-cured for 30 seconds (0.09 mW/cm^2) using a UV box (VWR). A calcein-AM/ethidium homodimer, Live/Dead assay (Thermo Fisher Scientific) was

used to assess cell viability within printed constructs according to the manufacturer's instructions.

Invasion Study

For the invasion experiments, cells were bioprinted (2 million cells/mL) along the periphery of the cylindrical placenta model with a chemotactic source (epidermal growth factor, 10 μM) at the center as previously described[5]. Cells were cultured in growth media with low serum concentration (5%) and phase-contrast images were taken on day 2 and day 7. The distance between the edge of the placenta model and the invasion fronts were measured and averaged over time to obtain invasion rates. For samples with reduced PI3K signaling, samples were treated with LY294002 (25 μM) on days 4 and 6 for 24 hours.

DNA Isolation and Quantification

Sample discs (10 mm diameter and 2 mm height, 2 million cells/mL) were bioprinted for gene expression studies. On day 7, bioprinted discs were treated with papain (4 mg/mL) for 20 mins at 37°C to dissolve the gel. Cells were lysed with RIPA Lysis and Extraction Buffer (Thermo Fisher Scientific). A Quant-iT PicoGreen dsDNA Assay kit (Life Technologies) was used to quantify DNA following the manufacturer's protocol.

RNA Isolation and qRT-PCR

Sample discs (10 mm diameter and 2 mm height, 2 million cells/mL) were bioprinted for gene expression studies. On day 7, bioprinted discs were dissolved by treating them with papain (4 mg/mL) for 20 mins at 37°C, and dissolved in Trizol. Total RNA was isolated from

the trophoblasts using the RNeasy Plus Mini Kit (Qiagen) and then reverse transcribed to complementary DNA (cDNA) using a High Capacity cDNA Archive Kit (Thermo Fisher Scientific). Quantitative reverse transcriptase-polymerase chain reaction (qRT-PCR) was performed by combining the cDNA solution with a Universal Master Mix (Thermo Fisher Scientific), as well as oligonucleotide primers and Taqman probes for MMP2, MMP9 and the endogenous gene control glyceraldehyde-3-phosphate dehydrogenase (GAPDH; Life Technologies). The reaction was performed using a 7900HT real-time PCR System (Applied Biosystems) at thermal conditions of 2 min at 50°C, 10 min at 95°C, 40 cycles of 15 s at 95°C, and 1 min at 60°C. The relative gene expression level of each target gene was normalized to the mean of GAPDH in each group then the fold change was determined relative to the Bioprinted Placenta Model without pECM. Fold change was calculated using the ΔΔCT relative comparative method as described previously[116].

Measurement of MMP Activity

Supernatant of bioprinted placenta model with different dosage of pECM were collected after 7 days of culture. The MMP activity was measured using the MMP Activity Assay Kit (Abcam) according to manufacturer's instructions.

Statistical Analysis

Error bars indicate standard deviation and * indicates statistically significant differences between groups. Data from all the studies were analyzed using the Multiple Comparison Test function in MATLAB. A confidence level of 95% was chosen, and p-values below 0.05 were considered significant. All experiments were done in triplicates (biological replicates) unless stated otherwise.

3.3 Results

3.3.1 Isolation and Characterization of Placental Basement Membrane Proteins (pECM)

To harvest relevant extracellular matrix (ECM) material to study trophoblast invasion, we isolated the basal plate of the fresh human term placentae by removing a thin layer (less than 3 mm) of tissue from the maternal side (**Figure 3.1a**, red arrows). Following decellularization and solubilization, the amount of DNA present in it the processed tissue was 95% lower than that of solubilized native tissue (**Figure 3.1d**) and was below the level indicated to induce immune response[165]. The decellularized and solubilized ECM isolated from term placenta is referred to as pECM for the rest of the work (**Figure 3.1b,c**). Next, we compared the amounts of collagen in pECM to solubilized native tissue and showed no significant differences (**Figure 3.1e**). These data show that the decellularization treatment was effective in removing the DNA contents and kept the ECM components intact which was demonstrated by the similar collagen levels. Since the mechanical properties of the substrate have a profound impact on cellular behavior[166], we used compression test and determined that the pECM has no significant impact ($p>0.05$) on the Young's modulus and yield strength of bioprinted GelMA constructs (**Figure 3.1f**). Therefore, any biological effects induced by pECM on trophoblasts were due to differences in ECM composition rather than bulk mechanical properties.

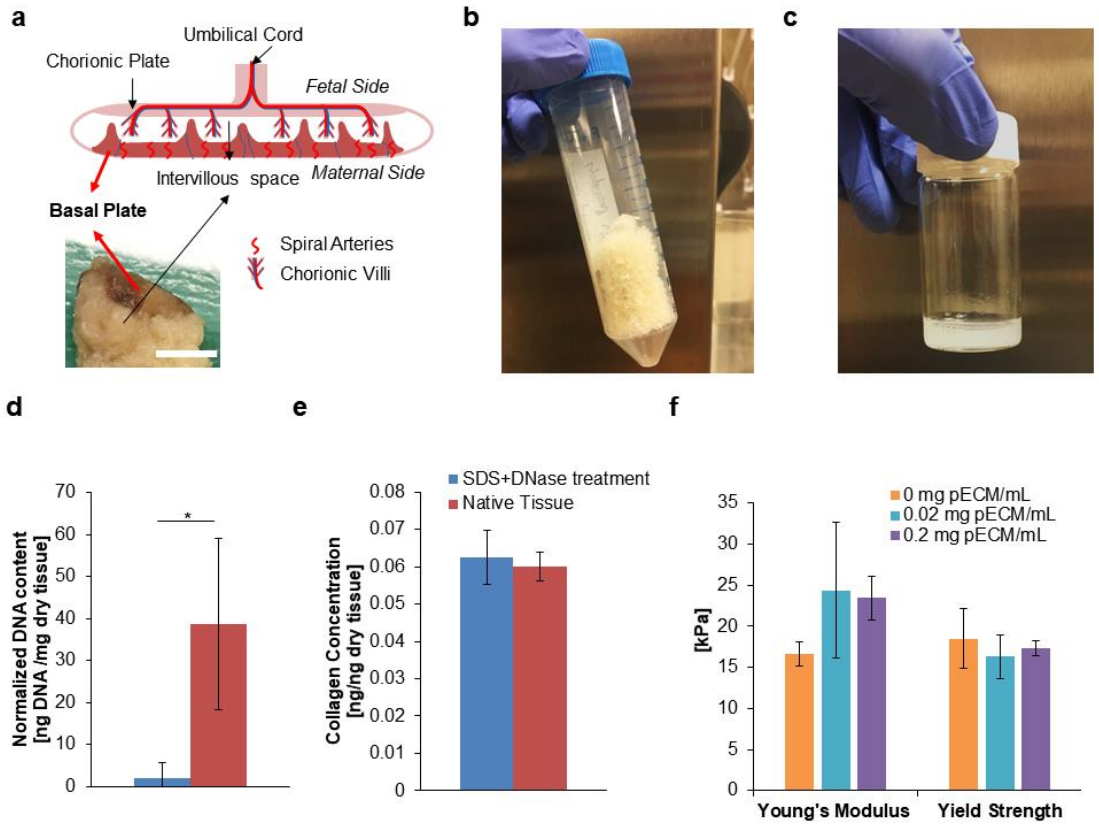

Figure 3.1. Development of Decellularized Placental ECM (pECM). (a) Anatomy of e*x vivo* placenta. Top image illustrated the major structures of human placenta and bottom image demonstrated a cross section of human placenta sample. Red arrows indicated the location of basal plate. (scale bar = 10 mm). **(b)** Representative image of lyophilized pECM. The tissue of basal plate was lyophilized for long term storage after it has been decellularized. The lyophilized pECM was a porous scaffold with white-yellow appearance. **(c)** Representative image of solubilized pECM. The lyophilized pECM was solubilized in pepsin under acidic condition at a desired concentration (0.1% w/v) to be bioprinted later. **(d)** DNA content of solubilized ECM**.** After treatments of SDS and DNase (blue), 95% of the DNA from the native tissue was removed (red) (n = 3). **(e)** Collagen content of solubilized ECM. There was no significant difference between the collagen contents of solubilized decellularized and native tissue, which suggested the integrity of the ECM was well-preserved after decellularization treatment (n = 3). **(f)** Effect of pECM on the mechanical properties of bioprinted constructs. Our results showed that the addition of pECM into bioprinted GelMA constructs did not alter the Young's modulus and yield strength significantly (n = 6). Error bars indicated standard deviation and * indicated statistically significant differences between groups ($p<0.05$).

3.3.2 Effect of pECM on Proliferation and Adhesion of Trophoblast

Since trophoblasts are anchorage-dependent and their binding to ECM is required to invade the decidual matrix, we tested the effect of pECM on proliferation and adhesion of trophoblast. As shown in **Figure 3.2a**, the fraction of adhered cells for pECM-coated group (0.82±0.05) was significantly higher than those of untreated plastic (0.35±0.19) and GelMA coated plastic (0.38±0.24). GelMA was used as a control because it is the basis material for our bioprinting work. In addition, the fraction of adhered cells on pECM coated wells was comparable to that of the fibronectin coated wells (0.85±0.06), a widely-used ECM matrix that promotes cell adhesion[5, 154]. In addition, we observed that the addition of pECM enhances the proliferation of bioprinted trophoblasts in a dosage-dependent manner (**Figure 3.2b**). Qualitative images using live/dead viability staining kit demonstrated that the additional pECM did not affect the viability of bioprinted trophoblasts with mostly viable cells (green) and very few dead cells (red, **Figure 3.2c**). Encapsulated trophoblasts form a sub-population of aggregates and appeared differently than 2D culture in bioprinted GelMA constructs, consistent with published literature with cells encapsulated in hydrogels (**Figure 3.2d**) [63]. These results demonstrated that pECM supports the adhesion and proliferation of trophoblast.

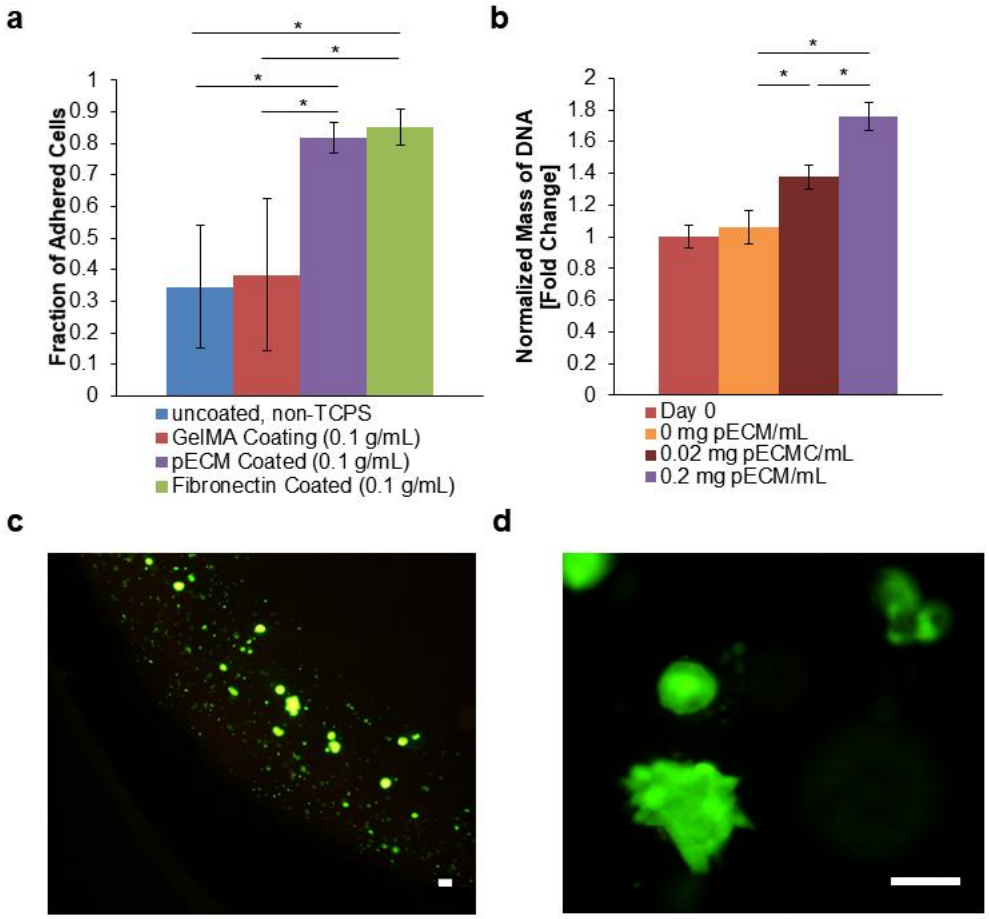

Figure 3.2. Effect of pECM on Growth of Trophoblasts. (a) Effect of pECM on relative adhesion. A washing adhesion assay, which was qualitative, was performed to test the relative adhesion of trophoblasts on different substrate coating [1-4]. Our results showed that pECM coating significantly increased the adhesion of trophoblasts compared to non-tissue culture treated polystyrene and GelMA coating. In addition, the fraction of adhesion was not significantly different from fibronectin, the most extensively utilized ECM to promote cell adhesion in biomedical research. **(b)** Effect of pECM on proliferation of trophoblasts. The mass of DNA of bioprinted trophoblasts encapsulated in different concentrations of pECM were quantified after 7 days of culture (normalized to day 0). Our results demonstrated a dosage-dependent response of DNA mass and concentration. **(c)** Representative live/dead images of bioprinted trophoblasts. The cells were stained with calcein-AM (green) for live cells and propidium iodide (red) for dead cells. The majority of the bioprinted trophoblasts were stained live (green) with very little dead (red) (scale bar = 100 µm). **(d)** Representative live/dead images of trophoblasts demonstrating formation of aggregates. The cells were stained with calcein-AM (green) for live cells and propidium iodide (red) for dead cells. (scale bar = 100µm). Error bars indicated standard deviation and * indicated statistically significant differences between groups ($p<0.05$).

3.3.3 Characterization of Complete and Fractionated pECM

Since pECM is a mixture of ECM proteins, we used proteomics to determine its composition to elucidate the mechanism behind the interactions between pECM and trophoblast. Using proteomics, we found the pECM was composed of mostly BM proteins (80% by peptide counts), including laminin, collagen, fibronectin, Howe sulfate proteoglycan (**Figure 3.3a**), and these results were validated by Western blot analyses (**Figure 3.3b**). To evaluate if the effect of pECM was due to the placental BM proteins, we used size-exclusion based chromatography (SEC) to separate pECM components into high molecular weight (>158 kDa, referred to as HMW-pECM) and low molecular weight (<3.5 kDa, referred to as LMW-pECM) as indicated by the two peaks in **Figure 3.3c**. Relative amount of ECM proteins in these two fractions were determined using proteomics (**Figure 3.3a**). Our results indicate that key placental BM proteins such as laminin, collagen, fibronectin, heparan sulfate proteoglycan, and nidogen were depleted in LMW-pECM as their amounts are lower than that of HMW-pECM by at least 3-fold.

a

ECM Molecule	Peptide Fraction	Peptide Ratio [HMW/LMW pECM]
Laminin Subunits	0.44	82
Collagen Subunits	0.14	7.5
Fibronectin	0.11	2.9
Heparan Sulfate Proteoglycan	0.09	12
Fibrinogen	0.09	6.8
Nidogen Subunits	0.02	4.0

b

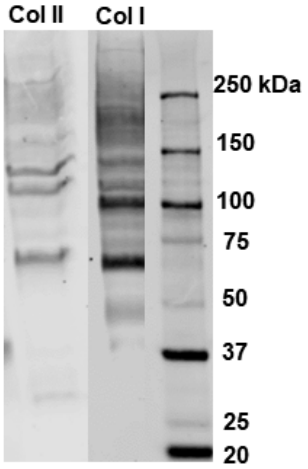

c

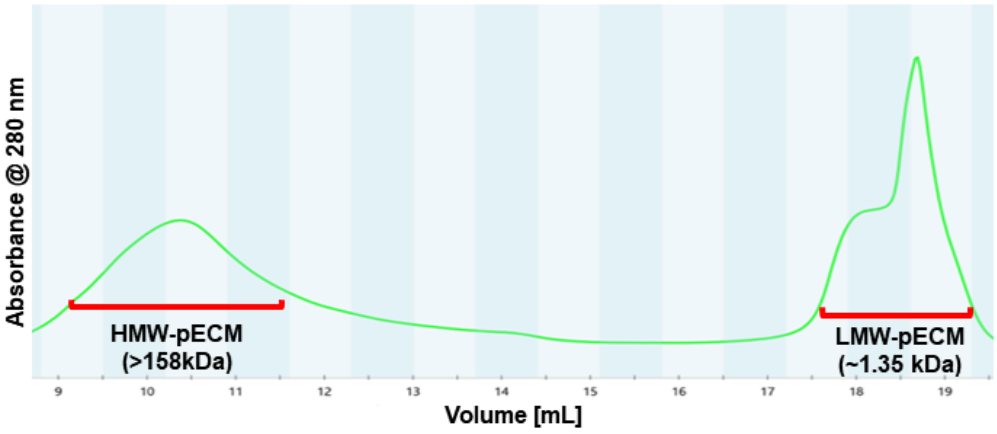

Figure 3.3 Characterization of Fractionated and Complete pECM. (a) Compositions of fractionated and complete pECM. We found that there was ample basement membrane (BM) proteins including laminin, collagen (VI, VI, XII, XIV and XV), fibronectin, BM-specific heparan sulfate proteoglycan in pECM which consist of more than 80% peptide fractions. Moreover, we quantified the peptides of ECM molecules and calculated the ratio of HMW over LMW pECM. We found that the amounts of placental BM proteins were at least two orders of magnitude higher in HMW pECM than that of LMW pECM. **(b)** Western blot results. SDS-page and positive immunostaining of collagen I, II served as confirmation of the proteomics results. **(c)** Chromatogram of solubilized pECM after eluting through a SEC column. Samples were taken from the high molecular weight fractions (defined as HMW pECM, MW>158 kDa) and low molecular weight fractions (defined as LMW pECM, MW~1.35 kDa).

3.3.4 Effects of Fractionated pECM on Trophoblast Invasion

Once the compositions of the fractionated and complete pECM were determined, we tested their effects on trophoblast invasion rates of BeWo cells, an epithelial trophoblastic cell line that is extensively used to study placental development[11, 29], in a bioprinted placenta model (BPM)[5]. BeWo cells was used instead of HTR8 because we wanted to study epithelial-mesenchymal transition of trophoblasts and HTR8 is considered mesenchymal-like based their positive expression for vimentin[167]. The concentrations of ECM protein were kept constant at a level that was comparable to current *in vitro* studies[5] across all groups in **Figure 3.4c**. The trophoblast bioprinted in LMW-pECM had a lower invasion rate compared to those of HMW-pECM (17.6±8.19 versus 36.1±12.5 μm/day, respectively; **Figure 3.4c**). Interestingly, however, both invasion rates were lower than that of complete pECM (65.8±37.5 μm/day; **Figure 3.4c**). These results indicated the effect of complete pECM on trophoblast invasion cannot be reproduced using individual fractions alone, suggesting a combination mechanism of action of both placental BM-proteins and peptide components. To confirm that invasion required the expression of MMP, a known group of enzymes that are responsible for the degradation of ECM proteins and are upregulated during EMT and invasion of trophoblasts[36, 162], we tested the effect of fractionated and complete pECM on the gene expressions of MMP2 and MMP9 (**Figure 3.5**) [60, 168]. HMW-pECM upregulated the expressions of MMP2 and MMP9 significantly ($p<0.05$) compared to LMW-pECM and the control group (**Figure 3.5a,b**). LMW-pECM, on the other hand, did not have a significant impact ($p<0.05$) on MMP2 or MMP9 expression. Even

though HMW-pECM upregulated MMP2 and MMP9 expressions, the magnitudes remained lower than that of complete pECM (1.40 versus 1.55 and 2.39 versus 5.99-fold change, respectively), again suggesting there may be synergistic effects between the different components of pECM which was consistent with the invasion rate results.

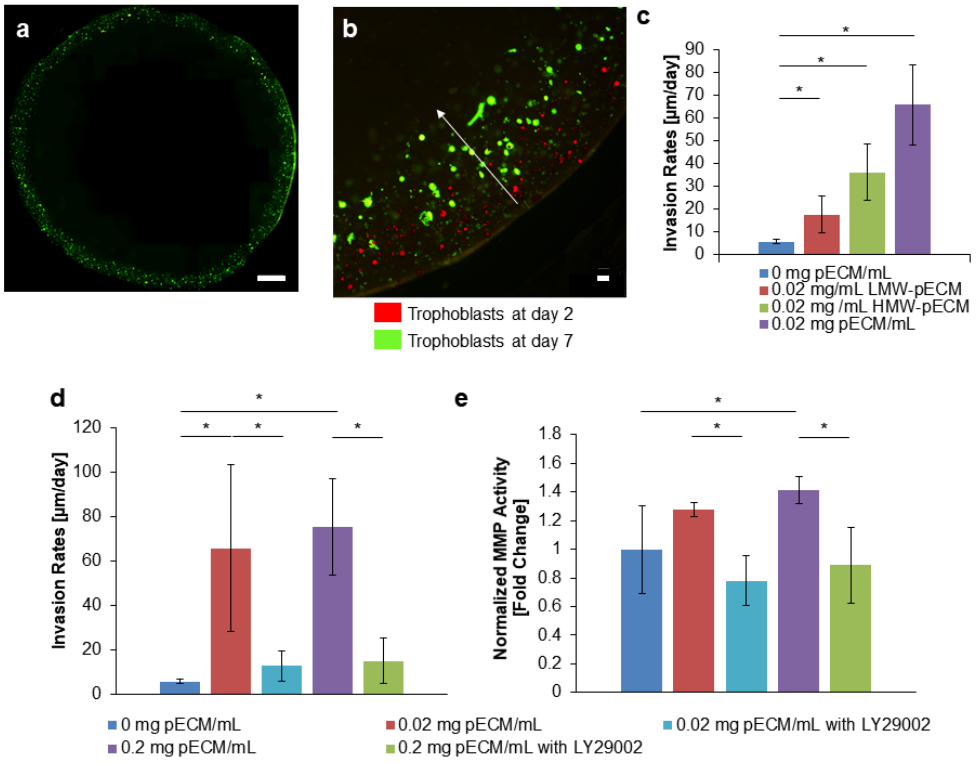

Figure 3.4. Effect of pECM on Trophoblast Invasion. (a) Overview of bioprinted placenta model. The bioprinted placenta model was based on previously published work that has a layer of trophoblasts along the periphery of a cylindrical disc (green) with a chemoattractant at the center. Placental BM proteins were incorporated with GelMA throughout the placenta model. **(b)** Representative images of trophoblast invasion. By taking images of trophoblasts at day 2 (red) and day 7 (green), we observed the shift in the invasion fronts. We calculated the invasion rates by taking the differences between the invasion fronts and average over time. **(c)** Effect of fractionated pECM on invasion rates of trophoblasts. The trophoblasts bioprinted in complete pECM had the highest invasion rates (n = 3), followed by HMW-pECM (n = 3) and then LMW-pECM (n = 3). **(d)** Trophoblast invasion rates as a function of pECM and PI3K inhibitor. The pECM at both dosages (0.02 and 0.2 mg pECM/mL, n = 3) significantly increased invasion rates of trophoblasts compared to the control BPM without any pECM (n = 3). The addition of LY29002, a PI3K inhibitor, significantly reduced the effect of pECM on the invasion rates when compared to their respective dosage of pECM (n = 3). Moreover, there's no statistically significant differences between the invasion rates of control BPM with no pECM and groups treated with PI3K inhibitor (n = 3), which indicated that the effect of pECM was completely removed. **(e**) Effect of pECM and PI3K inhibitor on MMP activities. A similar pattern was observed in the amount of MMP activity where pECM increased MMP activities significantly at both dosages (0.2 and 0.02 mg pECM/mL, n = 3) and the addition of PI3K inhibitor significantly reduced the effect of pECM (n = 3). Error bars indicated standard deviation and * indicated statistically significant differences between groups ($p<0.05$).

3.3.5 Mechanism of pECM-induced Trophoblast Invasion

Finally, we determined trophoblast invasion rates as a function of pECM concentrations to test our hypothesis that placental BM-proteins are required for effective trophoblast invasion. Our results showed that pECM, at both dosages (0.02 and 0.2 mg pECM/mL), significantly increased invasion rates of trophoblasts (65.8±37.5, and 75.5±21.8 μm/day, respectively; $p<0.05$; **Figure 3.4d**) compared to control BPM with no pECM (5.6±1.0 μm/day). Similarly, the addition of pECM increased MMP activities but only significantly at a higher pECM concentration (0.2 mg pECM/mL; $p<0.05$; **Figure 3.4e**). Since PI3K signaling is upstream of secretion of MMP and has been previously implicated in embryonic implantation, we tested its role trophoblast invasion[51, 60, 169]. The addition of a PI3K inhibitor (LY294002; 25 μM) in the presence of pECM significantly reduced the invasion rates (12.6±10.4 and 15.0±6.90 μm/day; $p<0.05$) compared to their respective dosages of pECM (65.8±37.5 and 75.5±21.8, respectively). Moreover, there were no statistically significant differences ($p>0.05$) between the invasion rates of control BPM and pECM groups treated with PI3K inhibitor, indicating that inhibiting PI3K signaling completely removed the effects of pECM. A similar pattern was observed in the amount of MMP activities (normalized to media) where pECM increased MMP activities (1.28±0.049 and 1.41±0.10; **figure 3.4e**) and the addition of PI3K inhibitor significantly reduced them (0.78±0.17 and 0.89±.27, respectively; $p<0.05$).

At the genetic level, the addition of complete pECM (0.2 and 0.02 mg pECM/mL) significantly upregulated MMP2 gene expression (1.55±0.04 and 1.97±0.08, respectively; $p<0.05$) and were reduced when PI3K inhibitor was added

(1.15±0.02 and 1.05±0.02, respectively; **Figure 3.5a**; $p<0.05$). Similarly, the addition of pECM significantly upregulated MMP9 (6.48±2.1 and 5.99±1.96, respectively; $p<0.05$) and were equally reduced when the PI3K was inhibited (1.24±1.1 and 1.48±0.50, respectively; $p<0.05$; **Figure 3.5b**). Additionally, there were no statistically significant differences ($p<0.05$) between control BPM without pECM and PI3K inhibited groups in terms of MMP2 and MMP9 expressions, indicating that the effect of pECM on the gene expressions was completely removed by PI3K inhibitors. These results indicated that the pECM-enhanced invasion rates were correlated directly with upregulated of MMP2 and MMP9, and PI3K signaling appear to play a dominant role in pECM-enhanced trophoblast invasion.

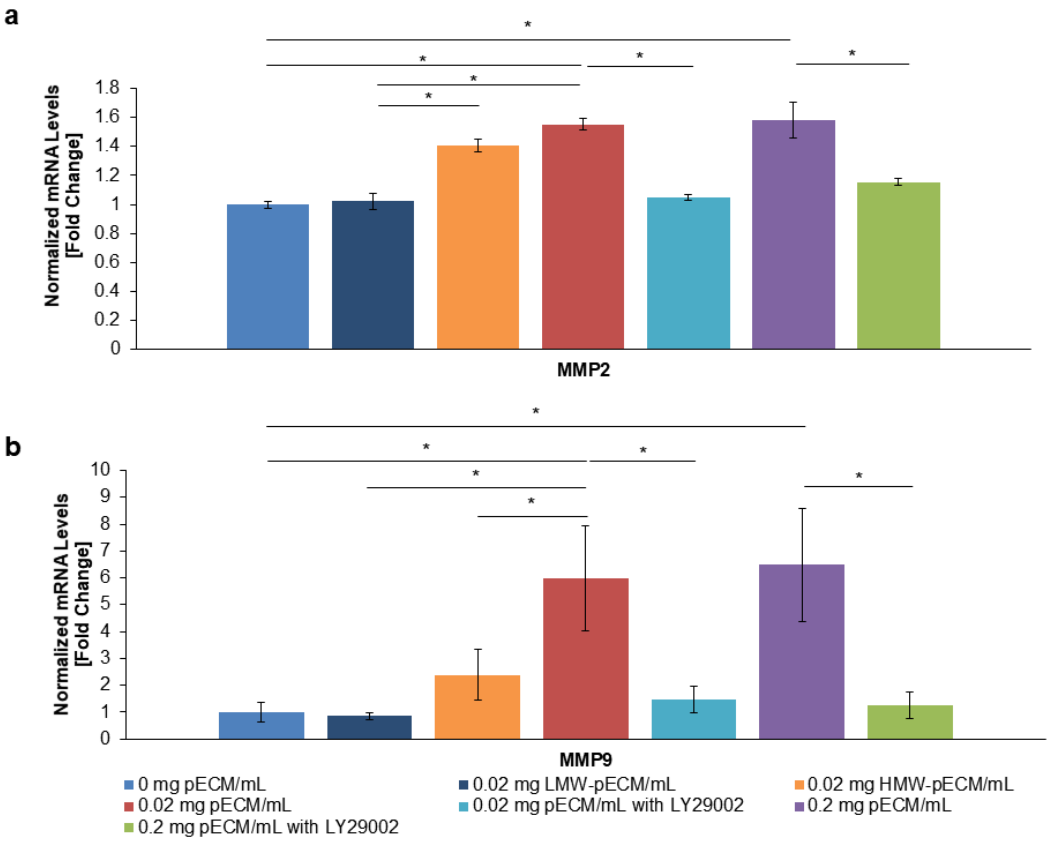

Figure 3.5. Mechanisms of pECM-enhanced Trophoblast Invasion. (a) Effect of pECM on the expressions of MMP2 of trophoblasts. The HMW-pECM increased the expressions of MMP2 significantly compared to LMW-pECM and control with no pECM (n = 3). The MMP2 expressions for HMW-pECM was lower than that of complete pECM with no significant differences (n = 3). LMW-pECM did not have a significant impact on the MMP2 expression (n = 3). The addition of pECM significantly increased the MMP2 gene expression compared to control (n = 3). However, the effect of pECM was completely removed when PI3K was inhibited with no significant differences with the control (n = 3). **(b)** Effect of pECM on the Expressions of MMP9 of Trophoblasts. The HMW-pECM increased the expressions of MMP9 significantly compared to LMW-pECM. However, the magnitude of HMW-pECM's impact on MMP9 was substantially lower than complete pECM. On the other hand, LMW-pECM did not change MMP9 expressions significantly compared to control (n = 3). Moreover, the treatment of pECM increased the MMP9 gene expression compared to control (0 mg pECM/mL) but again the effect was completely removed when PI3K inhibitor added with no significant differences with the control (n = 3). Error bars indicated standard deviation and * indicated statistically significant differences between groups ($p<0.05$).

3.4 Discussion

Trophoblast-ECM interactions play a fundamental role in placentation and are critical to placentation and pregnancy success [120]. However, there are very limited studies, if any, that examine the effect of ECM microenvironment on trophoblast invasion and differentiation. In this research, for the first time, the necessary and critical roles of placental BM proteins on trophoblast invasion were demonstrated. The addition of isolated placental BM proteins in pECM significantly increased the invasion rates by 13-fold and upregulated the gene expressions of MMP2 (1.5 fold) and MMP9 (6.3 fold) of trophoblasts. These pECM-enhanced invasive responses were completely removed upon the addition of PI3K inhibitor, suggesting placental BM protein stimulated trophoblast invasion predominantly through PI3K signaling.

In preparation for embryonic implantation, the maternal endometrium undergoes substantial remodeling and differentiation to become decidua [51, 154] and causes the maternal decidual stromal cells (those in direct contact with trophoblasts) produce pericellular basement membrane (BM) [159]. Published studies have established the significance of BM proteins in placentation and embryogenesis in murine BM-proteins ablated models [156], human placental tissue [8, 158, 170], and trophoblast invasion *in vitro* [158, 171, 172]. However, none of the studies to date have directly determined the impact of extracellular placental BM proteins on trophoblast invasion. We found the placental BM proteins significantly increased trophoblast invasion rates and MMP expressions. If we used the invasion rates obtained through the placenta model loaded with pECM and assumed a decidual thickness of 5 mm [173], the maternal decidua would be fully invaded by trophoblasts

in 7 weeks, consistent with *in vivo* results from human pregnancies [173]. Without the presence of placental PM proteins, the trophoblast invasion was critically impaired, a condition that is associated with preeclampsia [6, 9, 52, 121, 122]. These findings, for the first time, exemplifies the necessary and critical role of placental BM proteins in normal trophoblast invasion. Since placental BM proteins are secreted from decidualization, our findings validate the importance of endometrial remodeling prior to the arrival of blastocyst. Future studies will involve incorporating decidual stromal cells into our tissue-specific placental model to assess their roles in trophoblast invasion.

Our results showed that the placental BM proteins promoted trophoblast invasion predominantly through PI3K signaling, a critical signaling pathway downstream of RTK that regulates cell motility, proliferation, survival and growth [35, 60]. We demonstrated that the improved invasive phenotypes and genotypes of trophoblasts in the presence of pECM were completely removed when PI3K signaling was inhibited. This result was not surprising because other study demonstrated laminin binding activates the PI3K/AKT pathway in mammalian cells [174]. However, our results suggest that the reason for the failed implantation in RTK-ablated uterus in a murine model [51] may be due to impaired trophoblast invasion and differentiation. Since PI3K signaling appeared to be an important signaling pathway that regulates the interactions between trophoblast and placental BM proteins, it could be an attractive potential therapeutic target for preeclampsia. However, further testing for other molecular pathways and inhibitors are necessary before preclinical testing.

The ECM microenvironment plays a fundamental role in the maintenance of cellular phenotypes such as invasion [120, 161, 175]. There is strong evidence supporting that the interaction between ECM microenvironment and cells is mediated through receptor-ligand interactions and biomechanical stimuli, which in turn control cellular function [161, 175]. Recent studies have validated tissue-specific ECM improves cell function and intricate tissue formation [161, 176]. These ECM scaffolds were shown to have the capacity to direct tissue-specific cell lineage commitment and maintaining the phenotype of mature cell populations [161]. The cell-ECM interactions are extremely complex in nature and justify the need for a tissue-specific approach to recreate the native trophoblast niche to encourage and maintain their invasive phenotypes [161, 177]. As such, we isolated placental BM proteins from the basal plate of fresh term placenta because it is a rich source of invasive extravillous trophoblasts [177]. The primary amine groups of pECM should crosslink with the methacrylate side groups in GelMA through radical reactions [178]. It is unlikely that all pECM would be crosslinked with GelMA and their effects on trophoblast invasion is yet to be determined, although these soluble pECM could removed from the regular media changes. We found that we could not reproduce the biological effects of pECM using its fractionated components alone (pECM vs. LMW-pECM vs. HMW-pECM), which indicated that all components of pECM were required. Therefore, current literature on trophoblast biology that utilizes soluble, single ECM components and/or tissue culture polystyrene, while still valuable, may not represent the *in vivo* environment. Utilizing additive manufacturing technologies, we combined the unparalleled features of pECM with bioprinting to construct a

trophoblast-laden placenta model with micro-patterned biomaterials (**Figure 3.4a**). The ability to pattern cells and chemoattractant was crucial because it enabled the quantifications of cell invasion rates (demonstrated in **Figure 3.4b**) rather than the binary read-outs in current conventional 2D invasion assays (e.g. transwell). *In vitro* culture using pECM supports adhesion, proliferation and invasion of trophoblasts for at least 7 days. Altogether, we demonstrated that bioprinting with tissue-specific ECM is an attractive option for constructing *in vitro* placental tissue model to screen for novel therapeutics for placental diseases and their pathology. Our tissue specific, bioprinted placental model can potentially predict *in vivo* drug administration outcome for PE. Furthermore, other tissue models such as cancer can be developed based on the method presented in this work by recreating the key microenvironmental characteristics (complex ECM composition, mechanical properties, cellularity) that are representative to the *in vivo* environment.

3.5 Conclusion

We successfully incorporated placental BM protein (pECM) isolated from human placenta in our established bioprinting platform. Our results showed that pECM significantly increased adhesion, proliferation, and invasion of trophoblasts and these effects could not be reproduced using fractions of pECM. Particularly, the addition of pECM was required for trophoblasts to achieve effective invasion rates that is comparable normal pregnancies and PI3K appear to play a dominant role in this process. Our results illustrated, for the first time, the significant effects of the ECM microenvironment in trophoblast invasion, a parameter that is less investigated but critical in the development of preeclampsia. Moreover, the approach of

bioprinting organ models with organ-specific ECM can be used to screen for novel therapeutics for placental and other diseases such as cancer invasion.

Chapter 4: Interstitial Flow and Trophoblast Regulate Angiogenic Responses and Phenotypes in a 3D Bioprinted Placenta Model

4.1 Introduction

Tissues are composed of cells and extracellular matrix (ECM) that is filled with interstitial fluid [179]. Physiological processes such as muscle contractions can cause fluid flow within the ECM, which is defined as interstitial flow [179]. Interstitial flow causes fluid shear stress, defined as frictional force exerted by moving fluids on the surrounding wall, which is a key regulator for maintaining proper endothelium function [70, 180, 181]. Recently, studies have shown interstitial flow can induce shear stress in a hydrogel scaffold with significant biological effects on the cells encapsulated in the hydrogel [70, 182, 183]. However, the effect of interstitial shear stress on the angiogenesis (the development of new blood vessels from existing ones [67]) of endothelial cells (EC) is rarely investigated. Angiogenesis typically involves proliferation, upregulations of matrix metalloproteinase (a class of enzymes that degrades the extracellular matrix), and invasion/migration of endothelial cells [67]. In adults, angiogenesis seldom occurs except in would healing, pathological conditions (e.g. tumor growth), or endometrium growth during menstrual cycle/pregnancy [67].

Interstitial flow can arise from uterine contractile activities that are important for proper embryo implantation and pregnancy success [184]. Improper implantation can lead to preeclampsia (PE), which is a leading cause of maternal and perinatal

morbidity and mortality, affecting 3 to 8% of all pregnancies [107]. Globally, about 76,000 pregnant women and 500,000 infants are dying from PE and related hypertensive disorders [186]. Preeclampsia is characterized by intense systemic vasoconstriction leading to maternal hypertension, a clinical hallmark for preeclampsia [187]. Some of the early evidences of systemic endothelial dysfunction in preeclampsia came from measurement of plasma biomarkers of endothelial cell activation including von Willebrand factor [188], plasma cellular fibronectin [189], thrombomodulin [190], endothelin-1 (ET-1) [191, 192], and soluble fms-like tyrosine kinase (sFlt-1) [193]. These findings indicate that endothelial dysfunction plays a central role in preeclampsia, but the underlying mechanism is unclear [193]. One theory suggests that the microparticles secreted by trophoblast could be a major contributor [194, 195]. However, the effects of trophoblasts on the flow-induced remodeling of endothelial cells are unknown. This is, in part, because current *in vitro* placenta models are not equipped to simultaneously manipulate of fluid shear stress and cellularity.

In this work, we presented a robust platform to address this challenge using 3D printing and a perfusion based bioreactor. Our hypothesis was that interstitial flow induces angiogenic responses of endothelial cells and these responses are reduced in the presence of trophoblasts. We started by designing a cylindrical placenta model (diameter=10 mm; height=2 mm) with an patent central lumen (diameter = 1 mm) to model a major human artery (1-2 mm in diameter [196]). Customized bioreactor chambers were 3D printed to fit the bioprinted placenta model and connected to a perfusion based bioreactor [111, 116-118]. Shear stress and diffusion profiles were

characterized *in vitro* and *in silico*. Next, we bioprinted the 3D placenta model with endothelial cells homogenously distributed, and perfused through the lumen. We found that the flow could only affect endothelial cells that were less than 400 μm away from the lumen. Increasing shear stress led to higher angiogenic responses of endothelia cells, which were significantly impaired in the presence of trophoblast. These results demonstrated, for the first time, that the position of endothelial cells within a bioprinted hydrogel scaffold influenced their angiogenic responses and phenotypes. Moreover, fluid flow significantly augmented the angiogenic outgrowth and responses of endothelial cells, which were impaired by the presence of trophoblasts, providing a cellular mechanism for the systemic endothelial dysfunction observed in PE. Our strategy that generated neovascularized placenta model with spatially-defined heterogenous cellularity is a physiologically relevant tool for developing novel therapeutics and biomarkers for preeclampsia.

4.2 Materials and Methods

Cell Culture

Human Umbilical Vein Endothelial Cells (HUVEC) were purchased from Lonza, cultured in Endothelial Growth Medium Bullet Kits (EGM BulletKit; Lonza) according to manufacturer's instructions, and used until P5. HTR8 cells, an extravillous trophoblast cell line, were purchased from ATCC and cultured according to manufacturer's instructions. For coculture experiments, bioprinted placenta model were cultured in complete endothelial growth medium.

Gelatin Methacrylate Synthesis

Gelatin methacrylate was synthesized according to previously published methods [5, 78]. Briefly, type A porcine skin gelatin (Sigma-Aldrich; 300 bloom) was mixed at 10% (w/v) in phosphate buffered saline (PBS; Thermo Fisher Scientific) at 50 ^{o}C for 20 minutes. Methacrylic anhydride (MA, Sigma-Aldrich) was then added at 0.6 g of MA / g gelatin under rigorous stirring for an hour. The reactants were then diluted 2x with PBS to stop the reaction. The mixture was centrifuged, and the pellet was discarded. The supernatant was dialyzed against deionized water at 50°C using dialysis cassettes (10kDa MWCO, Thermo Fisher Scientific) for at least 3 days. The deionized water was changed twice a day to remove salts and excess methacrylic acid. The dialyzed GelMA was then lyophilized for at least 3 days and store at -80°C until further use.

Bioprinting Placenta Model

The placenta model is a cylindrical construct (height = 2 mm; diameter = 10 mm) with different biomaterials in the radial directions. All bioprinting work was completed using a commercial 3D bioprinter (3D-Bioplotter; EnvisionTEC). To prepare the prepolymer solution, lyophilized GelMA was dissolved in complete growth media at 50°C for 20 minutes. Photoinitiator (2-hydroxy-1-(4-(hydroxyethoxy)phenyl)-2-methyl-1-propanone; Irgacure 2959; BASF) was then added into the GelMA solution at 0.1% (w/v) at 50°C for 15 minutes. The prepolymer solution was loaded into the low-temperature printer head and allowed to equilibrate for 20 minutes at 37°C. Fibronectin (50 µg/mL), Human Umbilical Vein Endothelial Cells (HUVEC, 10 million/mL), and/or a trophoblast cell line (HTR8, 2 million/mL) were then added. The final enriched prepolymer solutions were then loaded into printing cartridge and allowed to equilibrate to printing temperature (20-21°C) for another 30 minutes prior to printing. Printed constructs were UV-cured for 30 seconds (0.09 mW/cm^2) using a UV box (VWR).

3D Printing of the Bioreactor Chamber

The bioreactor was designed using Solidworks 3D CAD software (Dassault Systèmes SolidWorks Corporation). The bioreactor is composed of two halves that form a single chamber when assembled together. Both halves of the bioreactor are separated by a biocompatible Viton Fluroelastomer O-ring (McMaster Carr) to ensure a leak free seal when assembled. The CAD model was exported as a binary stereolithography (STL) file for 3D printing. A deviation tolerance of 0.50 µm and

angular tolerance of 10 deg was chosen to preserve resolution during fabrication. The bioreactor was fabricated using the Connex500 3D printer (Stratasys) with Med610 polyjet material. Med610 was chosen for its biocompatibility to ensure the bioreactor did not adversely affect the soft tissue model. After 3D printing, the bioreactors were cleaned with water and sodium hydroxide, and then disinfected with an isopropyl bath per the manufacture's guidelines for Med610.

Perfusion Bioreactor System

The perfusion bioreactor system was assembled as described previously [111, 117, 118, 197] and illustrated in **Figure 1d**. Bioprinted placenta models were loaded into 3D printed bioreactor chamber (**Figure 1f**) and connected to the perfusion based bioreactor. The cell culture media was driven by an L/S Multichannel Pump System (Cole Parmer, Vernon Hills, IL) at controlled flow rates and cultured for 3 days. At the end of the study, bioprinted cells were isolated from GelMA scaffolds by dissolution in papain (4 mg/mL) for 30 min at 37^{o} C. A cell pellet was formed by centrifugation and used for downstream analysis.

Computational Fluid Dynamics (CFD)

The diffusion models developed in this study was generated using COMSOL assuming 1D radial diffusion in cylindrical coordinates. For diffusion of oxygen, we assumed a perfect source from the center of the disc and a no flux condition at the edge of the disc. For diffusion of biomolecules secreted from trophoblasts, we used EGF as our model biomolecule with a perfect source along the outer periphery of the

tissue model where trophoblasts were bioprinted and a perfect sink condition along the center lumen where endothelial cells were resided. The diffusion coefficient of oxygen [143] and epidermal growth factor [5] as the model biomolecule in GelMA was obtained from the literatures. Diffusion model were set up as described in chapter 2.

RNA Isolation and qRT-PCR

Cell pellets were dissolved in Trizol (Thermo Fisher Scientific). Total RNA was using the RNeasy Plus Mini Kit (Qiagen) and then reverse transcribed to complementary DNA (cDNA) using a High Capacity cDNA Archive Kit (Thermo Fisher Scientific). Quantitative reverse transcriptase-polymerase chain reaction (qRT-PCR) was performed by combining the cDNA solution with a Universal Master Mix (Thermo Fisher Scientific), as well as oligonucleotide primers and Taqman probes for MMP2, MMP9 and the endogenous gene control glyceraldehyde-3-phosphate dehydrogenase (GAPDH; Thermo Fisher Scientific). The reaction was performed using a 7900HT real-time PCR System (Applied Biosystems) at thermal conditions of 2 min at 50°C, 10 min at 95°C, 40 cycles of 15 s at 95°C, and 1 min at 60°C. The relative gene expression level of each target gene was normalized to the mean of GAPDH in each group then the fold change was determined relative to appropriate controls. Fold change was calculated using the ΔΔCT relative comparative method as described previously[116].

Invasion Study

For the invasion experiments, phase-contrast images were taken on day 1 and day 3. The distance between the periphery of the inner lumen of the soft tissue model and the invasion fronts of endothelial cells were measured and averaged over time to obtain invasion rates, as described previously [5, 78].

Immunofluorescence staining and Quantitative Image Analysis

Bioprinted, cell-laden GelMA hydrogels were fixed in 3.7% formaldehyde solution for 15 minutes and permeabilized with 0.3% Triton X-100 for 5 min. Hydrogels were blocked by 5% bovine serum albumin (BSA) solution for 30 min and incubated overnight with primary antibody (mouse anti-human CD31; 1:100 dilution; R&D systems). The stained HUVECs were observed with a fluorescent microscope. The endothelial cells were characterized for number of linear aggregates/area, length of aggregates, fraction of area covered by network of endothelial cells, and number of branching points/area using Image J [198]. At least 3 samples for each condition were processed for analysis.

Statistical Analysis

Error bars were expressed as standard deviation (SD) and * indicated statistically significant differences between groups. Data from all the studies were analyzed using student's t-test and/or analysis of variance (ANCOVA) using Minitab. All experiments were done in triplicates unless stated otherwise.

4.3 Result

4.3.1 Development and Characterization of a Customized Perfusion based Bioreactor System

Previous studies have demonstrated that interstitial flow can be generated *in vitro* near the surface of the hydrogels expositing to a parallel fluid flow [182]. In the present work, we leveraged the advantages of 3D printing to fabricate customized chambers to fit bioprinted placenta models based on a perfusion based bioreactor (**Figure 4.1a,d**) [5, 116]. We also fabricated a rack to hold the bioreactor chambers in place to ensure the directions of media flow and gravitational forces were uniform between samples. Next, the resulting fluid shear stress profile for the placenta model was calculated through computational fluid dynamics (**Figure 4.1b**). We found that the fluid shear stress could be controlled by adjusting the flow velocity, and the resulting shear stress values were in the physiologically relevant regime (**Figure 4.1c**). To ensure the nutrients could diffuse radially outwards in the bioprinted placenta model from the central lumen, we used a blue dye to observe the diffusion characteristics qualitatively. As shown in **Figure 4.1e**, the central lumen (red arrow) was patent and visible (top two images; d = 1 mm) at t = 0. After two hours of perfusion, limited radial diffusion was observed from the central lumen while the bulk of the 3D printed gel remained translucent. After 12 hours of perfusion, there were significant radial diffusion of the blue dye (**Figure 4.1e**). Computational fluid dynamics was utilized to quantitatively assess the mass transport of nutrients within the bioprinted placenta model. Using oxygen as a model nutrient, we found that there would be a gradient of oxygen in the first 11 hours of dynamic culture. After 11 hours

of dynamic culture, computational model predicted the nutrient would diffuse equally throughout the placenta model.

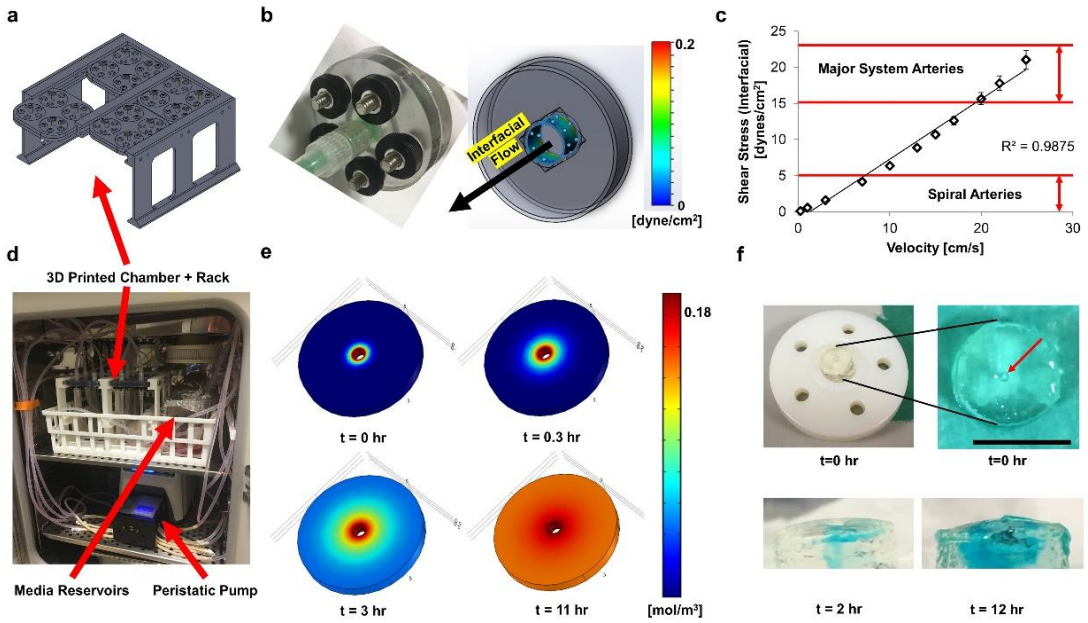

Figure 4.1. Development 3D Printed Perfusion Bioreactor System for the Bioprinted Placenta Model. (a) Computer-aided design (CAD) for customized bioreactor chamber. **(b)** Characterization of interfacial fluid shear stress. Flow was perfused through the center lumen of the bioreactor chamber (left) which induced shear stress along the wall. The wall shear stress was calculated by computational fluid dynamics (CFD, right). **(c)** Fluid shear stress as a function of flow velocity. CFD demonstrated a linear relationship between fluid shear stress and velocity in the physiologically relevant range ($R^2 = 0.99$). **(d)** Illustration of 3D printed tubular perfusion system. The perfusion system was driven by a peristaltic pump (bottom) that pushed the media from the media reservoirs through the 3D printed bioreactor chambers. The media was then returned to the media reservoir to complete the circulation. The entire system was housed in a cell culture incubator with temperature and humidity control. **(e)** Concentration profile of oxygen in the bioprinted placenta model. Computational fluid dynamic predicted that oxygen concentration would reach equilibrium by 11 hours. **(f)** Qualitative images of bioprinted placenta model. The picture on the top left demonstrated where the placenta model would be housed relative to the 3D printed reactor chamber, and was enlarged in the picture on the right. The bioprinted placenta model had a cylindrical shape (diameter = 10 mm; height = 2 mm) with a patent channel at the center (red arrow). Using a blue dye, we demonstrated that material diffused radially outwards from the central lumen after 12 hours of perfusion (scale bar = 1 mm).

4.3.2 Position of Endothelial Cells Influences their Proliferation and Angiogenesis

To determine effect of position on angiogenesis of endothelial cells, we bioprinted placenta models that had endothelial cells homogenously distributed. Then we divided the bioprinted placenta model into 3 zones according to their distances from the central lumen for quantitative image analysis (I = 0-200 μm, II = 200-400 μm, and III = 400-600 μm; **Figure 4.2a**). Fluorescent intensity (FI, normalized to the brightest reading in each zone) of DAPI, which correlated with number of cells, decreased as distance from the central lumen increased (I=0.92±0.08; II=0.77±0.11; III=0.66±0.15). This was not surprising because fluid shear stress is known to induce endothelial cells proliferation [180]. Similarly, angiogenic responses measured by network formation of endothelial cells also significantly decreased as distance from the central lumen increased (**Figure 4.2c,d**; number of linear aggregates (I=92.67±37.69, II=50.68±22.92, III=8.61±5.51 tubules/mm^2) and fraction of area covered by EC networks (I=7.9±2.81, II=4.32±0.94, III=0.74±0.92 %)). Altogether, we found that the angiogenic effects of flow significantly reduced for endothelial cells that were more than 400 μm away from lumen. Therefore, analysis for the rest of the work focused on endothelial cells that were within 400 μm measured from the lumen.

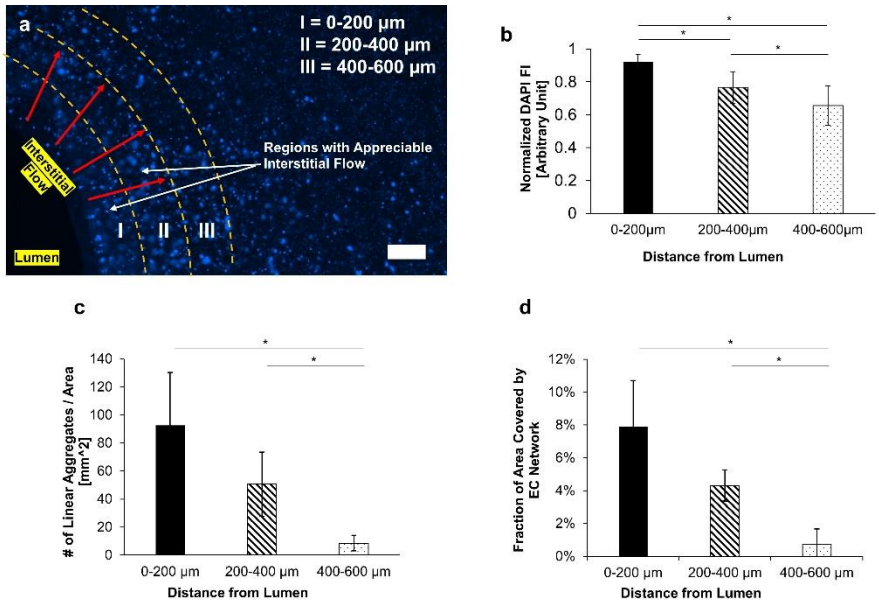

Figure 4.2 Position of Endothelial Cells Influenced Proliferation and Angiogenesis during Dynamic Culture. (a) Representative of bioprinted endothelial cells with DAPI Staining. The bioprinted placenta model was divided into 3 zones according to their distance from the central lumen (I = 0-200 µm, II = 200-400 µm, and III = 400-800 µm) for quantitative image analysis (scale bar = 200 µm). **(b)** Fluorescent intensity (FI) of DAPI as a function of position. Average DAPI FI, which correlated with the number of cells, was measured. The FI decreased as the distance from the central channel increased (n = 3). **(c)** Number of linear aggregates as a function of position. The number of linear aggregates/area decreased as the distance away from the central channel increased (n = 3). **(d)** Fraction of area covered by EC network. The fraction of area covered by EC network decreased as distance from central channel increased (n = 3). Error bars represented standard deviation and * indicated significant difference between groups ($p<0.05$).

4.3.3 Dosage-Dependent Effects of Shear Stress on Angiogenesis and Outgrowth of Endothelial Cells

It is widely accepted that fluid shear stress promotes angiogenic response of endothelial cells but the impact of interstitial flow in endothelial cells remain poorly understood. To investigate the effect of interstitial flow in angiogenesis, a layer of endothelial cells (<400 μm wide) were bioprinted along the periphery of the central lumen in the placenta model. After 3 days of perfusion, the angiogenic responses of endothelial cells were assessed and compared against static control. Representative images in **Figure 4.3a,c,b** showed a dosage-dependent response of network formations (demonstrated by multiple nuclei stains) in the dynamic culture groups while the static control group remain their circular morphology. Quantitative image analysis demonstrated a significant ($p<0.05$) dosage-dependent angiogenic responses of endothelial cells, measured by network formation, towards interfacial shear stresses based on length of aggregates, number of linear aggregates/area, fraction of area covered by EC network, and number of branching points/area (**Figure 4.3d-g**). Normalized fluorescent intensity (FI) of CD31 of endothelial cells (a marker for angiogenesis [199]) also appeared to be positively correlated with shear stress (static=1±0.001, 0.1 dyne/cm^2=2.43±0.01 and 1 dyne/cm^2=2.84 ±0.02; $p<0.05$; **Figure 4.4**).

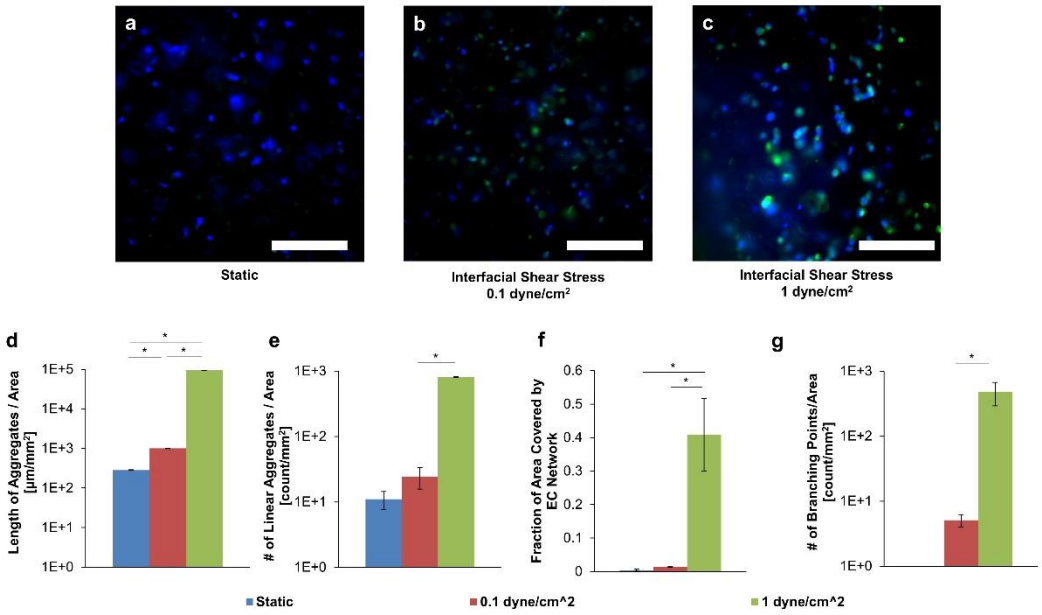

Figure 4.3. Fluid Shear Stress Augmented *In Vitro* Angiogenesis of Endothelial Cells. (a) Representative fluorescent images of EC in static culture. After 3 days of static culture, cells remained circular (blue = nuclei; green = CD31; scale bar = 100 µm). **(b)** Representative fluorescent images of EC under 0.1 dyne/cm^2 of interfacial shear stress. Limited network formation of EC occurred after 3 days of dynamic culture (blue = nuclei; green = CD31; scale bar = 100 µm). **(c)** Representative fluorescent images of EC under 1 dyne/cm^2 of interfacial shear stress. Significant network formation of EC occurred after 3 days of dynamic culture (blue = nuclei; green = CD31; scale bar = 100 µm). (**d-g**) Quantitative image analysis to determine EC network formation. Interstitial flow induced angiogenic response of EC in a dosage dependent-manner by increasing the number, length, and area of the linear aggregates, as well as the number of branching points (n = 3). Error bars represented standard deviation and * indicated significant difference between groups ($p<0.05$).

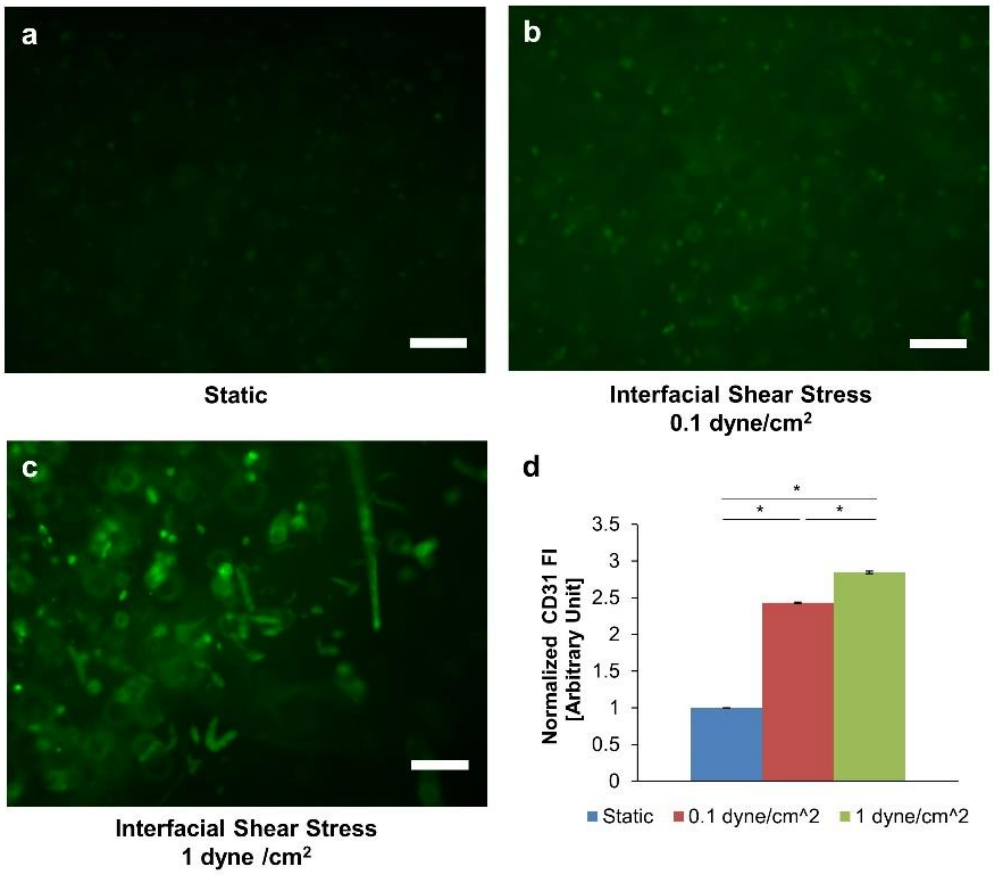

Figure 4.4. CD31 Staining of Endothelial Cells was Enhanced by Fluid Shear Stress. (a) Representative image of fluorescent staining for CD31 in static culture (scale bar = 100 μm). **(b)** Representative image of fluorescent staining for CD31 under 0.1 dyne/cm^2 of interfacial shear stress (scale bar = 100 μm). **(c)** Representative image of fluorescent staining for CD31 under 1 dyne/cm^2 of interfacial shear stress (scale bar = 100 μm). **(d)** Fluorescent intensity of CD31. Fluid shear stress enhanced fluorescent intensity of CD31 in a dosage-dependent manner (n = 3). Error bars represented standard deviation and * indicated significant difference between groups ($p<0.05$).

In addition to network formation and CD31 staining, another key angiogenic phenotypes are the migration/outgrowth of endothelial cells [198]. Bright field images showed interfacial shear stress at 1 dyne/cm^2 induced invasion of endothelial cells compare to static control (**Figure 4.5a,b**) with significant differences in the outgrowth rates (static=14.10±2.30 μm/day, dynamic=31.88±7.48 μm/day; $p<0.05$; **Figure 4.5c**). Gene expressions of invasion and angiogenic markers such as MMP2 (static=1±0.06, dynamic=2.74±0.12; $p<0.05$), MMP9 (static=1±0.05, dynamic=17.18±4.03; $p<0.05$), and VEGFA (static=1±0.06, dynamic=1.75±0.08; $p<0.05$) were all significantly upregulated when exposed to interstitial fluid shear stress (**Figure 4.5d-f**). The significant upregulation of VEGFA suggest the interstitial flow-induced angiogenic responses may be mediated by VEGF signaling pathway.

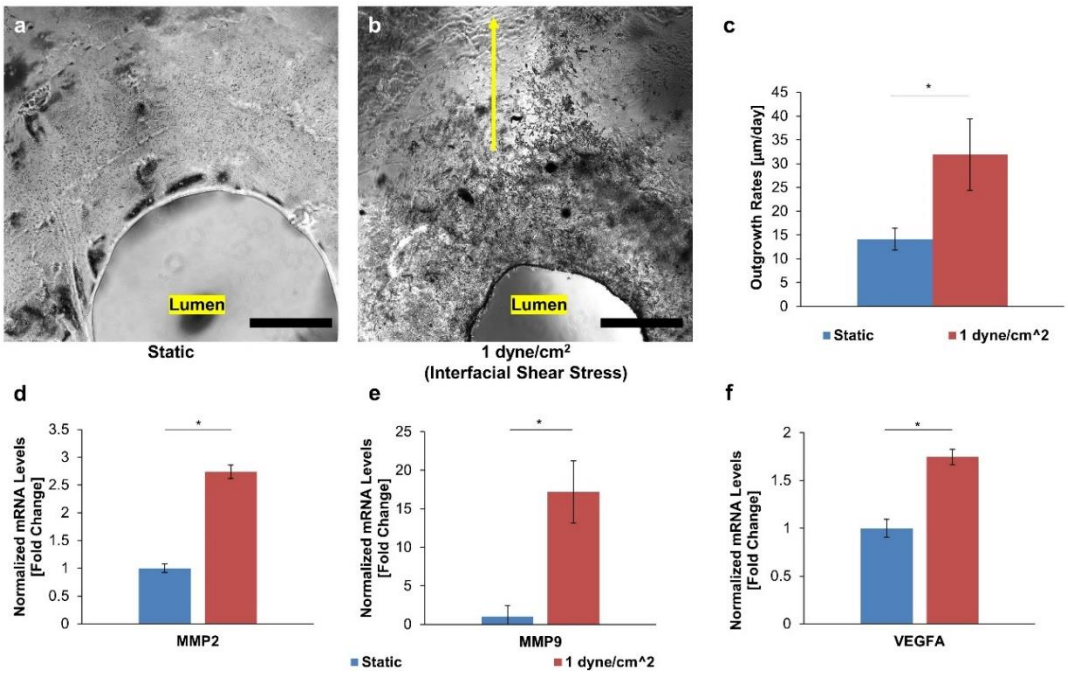

Figure 4.5. Fluid Shear Stress Promoted Outgrowth of Endothelial Cells. (a) Representative image of placenta model under static culture. After 3 days of static culture, endothelial cells remained circular with limited outgrowth (scale bar = 500 μm). **(b)** Representative image of dynamic culture. Outgrowth of endothelial cells occurred in the direction of interstitial flow (yellow arrow) with extensive network formation after 3 days of dynamic culture (scale bar = 500 μm). **(c)** Outgrowth rates of endothelial cells. Interstitial flow enhanced endothelial cells outgrowth rates significantly (n = 3). Interstitial flow significantly increased gene expressions of angiogenic markers such as **(d)** MMP2 (n = 3), **(e)** MMP9 (n = 3), and **(f)** VEGFA (n = 3). Error bars represented standard deviation and * indicated significant difference between groups ($p<0.05$).

4.3.4 Flow-Induced Endothelial Cells Outgrowth and Angiogenesis were Impaired by Trophoblasts

Once we have determined the angiogenic responses of endothelial cells in the customized perfusion bioreactor system, we used it to test endothelium-trophoblast interactions, a crucial process in placental development and preeclampsia [6, 107, 200, 201]. Utilizing the advantages of bioprinting, we patterned a ring of trophoblasts (green in **Figure 4.6a**) that was relatively far away from the endothelial cells (<4 mm). Endothelial cells remained along the periphery of the inner lumen (red in **Figure 4.6a**). Shear stress was maintained at 1 dyne/cm^2, which was similar to what is observed *in vivo* [196]. Compare to controls, the endothelial cells invaded less and had less network formation in the presence of trophoblasts (**Figure 4.6b,c**). Quantitative image analysis showed the outgrowth rate of endothelial cells was significantly impaired by the presence of trophoblasts (Trophoblast (+) = 1.82±7.11 μm/day, Trophoblast (-) = 30.47±5.99 μm/day; **Figure 4.6d**; $p<0.05$). On the other hand, presence of endothelial cells reduced the invasion rates of trophoblasts significantly (**Figure 4.6e)**. Further analysis demonstrated that the presence of trophoblasts reduced the length of aggregates of endothelial cells in **Figure 4.7a,b** (Trophoblast (+) = 14.03 ± 4.32 x1000μm/mm^2, Trophoblast (-) = 27.11±1.77 x1000μm/mm^2; $p<0.05$) and number of linear aggregates (Trophoblast (+) = 401.14±122.02 /mm^2, trophoblast (-) = 558.18±115.42 tubules/mm^2; $p>0.05$). Moreover, the presence of trophoblasts significantly reduced the fraction that are covered by EC network (Trophoblast (+) = 0.095 ± 0.024, Trophoblast (-) = 0.43±0.14; $p<0.05$) and number of branching points (Trophoblast (+) =

152.33±31.12/mm^2, Trophoblast (-) = 305.05±25.06/mm^2; $p<0.05$). Since there was a relatively large distance between endothelial cells and trophoblasts, the reduced outgrowth rates were most likely due to the biomolecules secreted by the trophoblasts. Computational fluid dynamic predicted that the biomolecules secreted by trophoblasts, using EGF as a model, would diffuse to the endothelial cells and reached a physiologically relevant concentration (>100 nM) by day 1 (**Figure 4.7e,f**). Taken together, these results showed the presence of trophoblasts impaired the angiogenic response and phenotypes of endothelial cells.

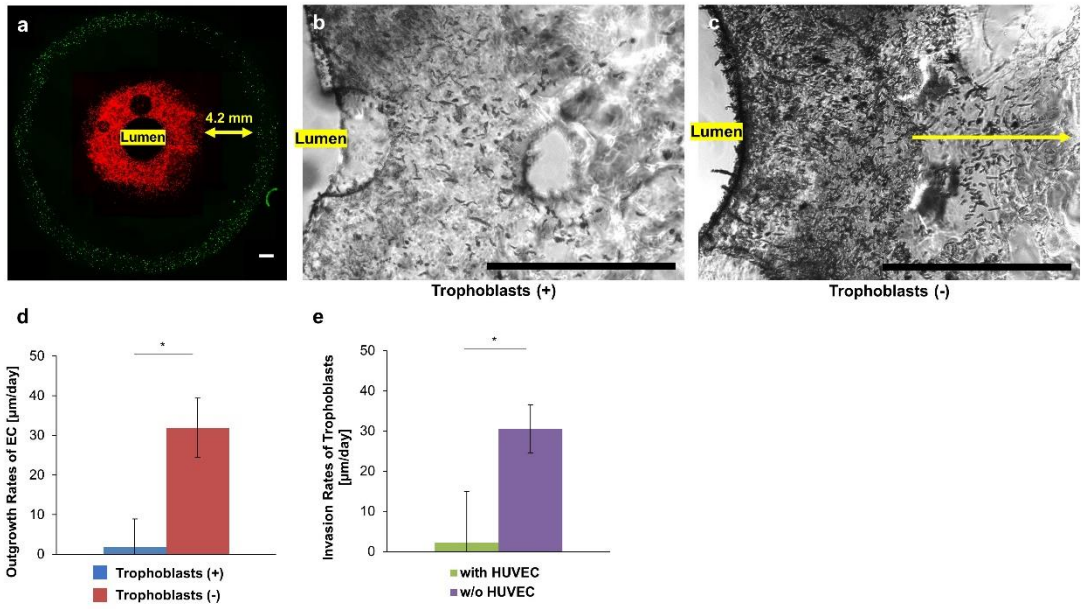

Figure 4.6. Interactions between Trophoblasts on Endothelial Cells. (a) Representative fluorescent images of bioprinted placenta model to determine endothelium-trophoblasts interactions. Endothelial cells (red) were bioprinted along the inner periphery of the inner lumen while trophoblasts (green) were bioprinted along the outer periphery (scale bar = 500 µm). **(b)** Representative bright field image of endothelial cells with trophoblasts (scale bar = 500 µm). **(c)** Representative bright field image of endothelial cells without trophoblast (scale bar = 500 µm). **(d)** Outgrowth rates of endothelial cells. The presence of trophoblasts significantly impaired the outgrowth rates of endothelial cells compare to control (n = 3). (**e**) Invasion rates of trophoblasts as a function of endothelial cells. The presence of endothelial cells significantly reduced the invasion rates of trophoblasts (n = 3). Error bars represented standard deviation and * indicated significant difference between groups ($p<0.05$).

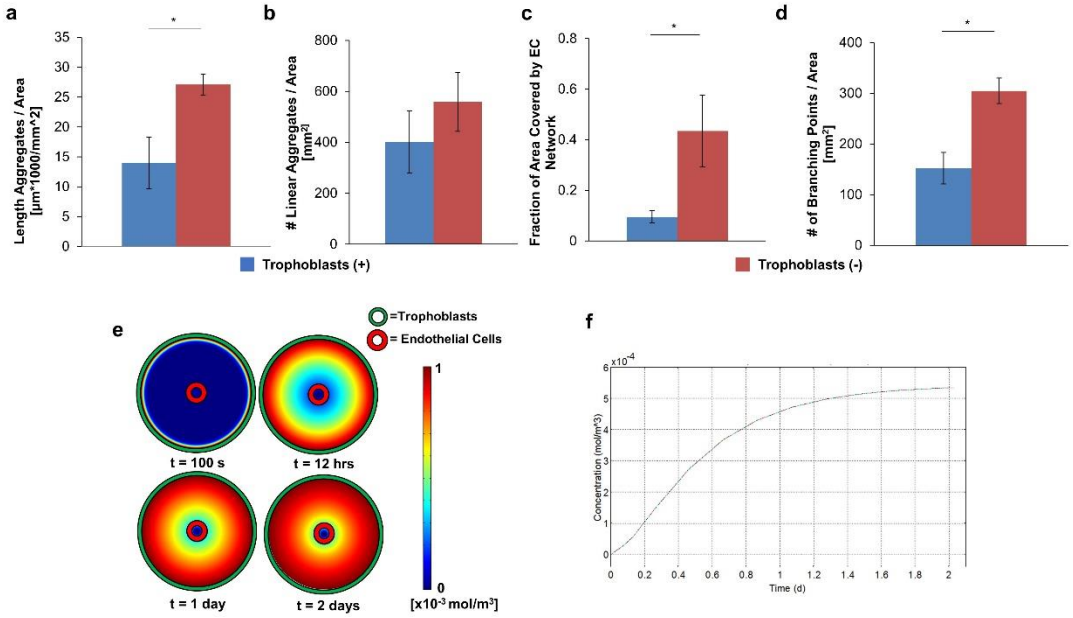

Figure 4.7. Effect of Trophoblasts on Angiogenesis of Endothelial Cells *In Vitro*. Quantitative image analysis indicated the presence of trophoblast impaired angiogenic phenotypes of endothelial cells such as **(a)** Length of aggregates/area (n = 3), **(b)** Number of linear aggregates/area (n = 3), **(c)** Fraction of area covered by EC network (n = 3), and **(d)** Number of branching points/area (n = 3). **(e)** Diffusion profile of EGF as our model biomolecule secreted from trophoblasts (outer ring in green with black outline) towards endothelial cells (inner ring in red with black outline) by computational fluid dynamics. **(f)** Local concentration profile of EGF secreted by trophoblasts at the position of endothelial cells (400 µm away from the lumen). Error bars represented standard deviation and * indicated significant difference between groups ($p<0.05$).

4.4 Discussion

The goal of this research was to determine the effect of interstitial flow and trophoblast on the angiogenic response and phenotypes of endothelial cells. Leveraging the advantages of 3D printing and perfusion based bioreactor, we developed a robust experimental platform that could apply stable and controlled fluid shear stress in a 3D bioprinted placenta model. Flow stimulation led to a dosage-dependent increase of angiogenic and proliferative responses of endothelial cells in regions near the perfused lumen (<400 μm). The shear stress-induced angiogenic response of endothelial cells was impaired in the presence of trophoblasts.

Previous studies have demonstrated interstitial flow can occur by applying an interfacial flow parallel to the surface of a hydrogel [70, 182, 183]. Chen et al. characterized the interstitial flow fields based on the fluorescence recovery after photobleaching technique and found the effect of interstitial flow (e.g. shear stress and convective diffusion) become negligible at depths beyond 50 micrometers [182]. However, the system used by Chen et al. was acellular and significantly smaller (lumen diameter=200 μm; thickness=100 μm), while our system was cell-laden and orders-of-magnitude larger (lumen diameter=1000 μm and thickness=5000 μm). The depth influenced by interstitial flow in the larger system should scale-up in proportion [182], which explain the deeper region (200-400 μm) of enhanced proliferation and network formation of EC observed in our study. Additionally, gradients of soluble factors created from the enhanced transport and mechanotransduction from the interstitial flow may lead to paracrine signaling effects that extend beyond that layer of interstitial flow.

Endothelium plays a central role in preeclampsia that is characterized by systemic maternal hypertension and intense vasoconstriction [67]. While the underlying mechanism of this endothelium dysfunction is unclear, one theory suggested that the microparticles secreted by trophoblast could be a major contributor [194, 195]. Specifically, Sargent et al. showed that a higher concentration of trophoblast-derived microparticles in women with preeclampsia [194]. However, the effect of trophoblasts on angiogenesis of endothelial cells, a process that is critical in successful implantation, remain to be elucidated. In this research, we showed the presence of trophoblast reduced the angiogenic response of endothelial cells. The spatial arrangement of cells suggested the reduced angiogenesis was most likely due to the diffusion biomolecules from trophoblasts to the endothelial cells, a first piece of *in vitro* support for the theory proposed by Sargent et al. Interestingly, the presence of endothelial cells seem to reduce trophoblast invasion rates. This implied the invasion of trophoblast is likely to be driven by chemokines secreted from the maternal circulation [42] rather than signals produced directly from endothelial cells. Overall, our results propose a novel cellular mechanism for endothelium dysfunctions observed in preeclampsia.

The creation of vascularized engineered tissues of clinically relevant size has been a major challenge in tissue engineering [202]. Recent advances in bioengineering have led to the development of complex experimental platforms to model angiogenesis of endothelial cells in response to fluid shear stress [70]. However, these existing experimental platforms are often in micron-scale, which may not be suitable for all scenarios. For example, one of the major challenge in tissue

engineering is vascularization upon implantation [202], which are typically in millimeter-centimeter scale [203]. Scaling up from micrometer scale system to human-sized scale can be problematic [119]. Moreover, biological processes involving cells-ECM-growth factors may take place in millimeter-centimeter scale (e.g. trophoblast invasion penetrates 5 mm thick layer of tissue *in vivo* [173]). In this work, we found that the interstitial flow induced by tubular perfusion system induced network formation that covered 51.6±1% of the soft tissue model by volume. The heterogeneous effect of the interstitial flow on the cells encapsulated in bioprinted hydrogel was defined, which would be an important parameter to consider for engineering complex tissues. Moreover, this platform provided an effective tool to study angiogenic response and migration of endothelial cells to controlled flow and/or other microenvironmental factors. Using 3D bioprinting, multiple biomaterials (e.g. cells and growth factors) can be easily deposited simultaneously to define the mechanism governing the angiogenesis of endothelial cells. Our approach of leveraging 3D printing and perfusion based bioreactor to create a heterogenous and pre-vascularized hydrogel in millimeter-centimeter scale served as a step towards fabricating relevant tissue engineered constructs for regenerative medicine, drug discovery, and mechanistic study.

4.5 Conclusion

In this work, a robust platform that generated neovascularized, complex placenta model in millimeter-centimeter scale was presented. Through cell patterning and a customized perfusion based bioreactor, we found the position of endothelial cells relative to the lumen of the hydrogel influenced their angiogenic response.

Interstitial flow alone led to orders-of-magnitude increase in angiogenic responses of endothelial cells in a dosage-dependent manner. This enhanced angiogenesis was impaired in the presence of trophoblast, suggesting a cellular mechanism of the systemic endothelial dysfunction observed in preeclampsia. Our versatile approach can generate heterogenous, pre-neovascularized placenta model for developing novel therapeutics and biomarkers for preeclampsia.

Chapter 5: Summary and Future Directions

5.1 Summary

The goal of this work was to determine the role of cellular microenvironment in preeclampsia, a leading cause of maternal and perinatal morbidity and mortality. Utilizing the capabilities of 3D bioprinting and shear wave elastography, we first developed a bioprinted placenta model to study and quantify trophoblast migration, which is presented in chapter 2 of this work. Using the bioprinted placenta model, we established a positive correlation between of epidermal growth factor (EGF) and migration rates of trophoblasts. These results indicate a feasible *ex vivo* placental model can be bioprinted to examine cellular, molecular and pharmacologic interactions.

Once we have established the bioprinted placenta model, we wanted to determine the effect of extracellular matrix composition on trophoblast invasion, which was summarized in chapter 3. From the literature we learned the placental basement membrane proteins (e.g. laminin, collagen) has been implicated in the development of placenta while the level of laminin is significantly lower in preeclampsia. We isolated extracellular matrix material from term placenta and found that 80% of its peptides were BM proteins. These basement membrane proteins upregulated expressions of MMP2 and MMP9 and increased the motility rates of trophoblasts by 13-fold to achieve an effective invasion rate that was comparable to *in vivo* results. Treatments with PI3K inhibitors completely removed the pECM-enhanced invasive phenotypes and genotypes of trophoblasts, suggesting its dominant role in trophoblast-ECM interactions. These results described, for the first time, the

substantial effects of the extracellular matrix on regulating trophoblast invasion, an area that is less investigated but appear to be critical in the pathogenesis of preeclampsia.

Finally, in chapter 4, we use the perfusion based bioreactor system to place the placenta model under fluid flow to determine the effect of trophoblast on placental angiogenesis. Clinically, preeclampsia is characterized by systemic maternal endothelial dysfunction. Biomolecules secreted by trophoblast was proposed to be a mechanism for the systemic endothelial dysfunction in preeclampsia but their effect on the angiogenesis of endothelial cells is unclear, partly due to a lack of suitable experimental tools. In the last part of the experimental work, we improved the bioprinted placenta model by developing a customized perfusion bioreactor system that addressed this challenge. The diffusion and shear stress profile for the perfusion bioreactor system were characterized by computational fluid dynamics. We found interstitial flow could enhance angiogenic responses of endothelia cells, demonstrated by orders of magnitude increase in network formations, significantly increased outgrowth rates, and upregulation of angiogenic-associated genes. Presence of trophoblast impaired these interstitial flow-enhanced angiogenic responses and outgrowth of endothelial cells, suggesting a cellular mechanism for the systemic endothelial dysfunction observed in preeclampsia.

In conclusion, we have introduced, for the first time, the decidual ECM compositions and trophoblast-EC interactions as potential pathologies for preeclampsia. Specifically, the critical role of placental basement membrane protein in normal trophoblast invasion suggested decidual ECM can be a potential biomarker

for diagnosing and predicting preeclampsia. Moreover, trophoblast significantly impaired the angiogenic responses of endothelial cells, indicating their potential roles in the systemic endothelium dysfunction. Taken broadly, our bioprinted placenta model is a safe, physiologically relevant, and high throughput tool to screen and develop the much-needed therapeutics, biomarkers, and predictors for preeclampsia.

5.2 Proposed Future Work

In this work, we have described significant roles of extracellular matrix composition and fluid flow in preeclampsia, but there are certainly other important questions related to preeclampsia that can to be answered using our bioprinted placenta model as future work.

One interesting study would involve isolating primary biomaterials (e.g. trophoblast and extracellular matrix) from normal and preeclamptic pregnancies to answer a fundamental question in the mechanism of preeclampsia: is the impaired trophoblast invasion in preeclampsia due to the extrinsic properties of the maternal decidual microenvironment or is it due to the intrinsic properties of the fetal trophoblasts? This question has been debated among investigators in the field of placental biology [204] and we have developed a tool that can be used to find the answer. Specifically, we could use trophoblasts isolated from preeclamptic placenta and test their invasion rates in 3D placenta model containing either extracellular matrix isolated from normal or preeclamptic placenta. Assuming the impaired trophoblast invasion is due to the cells' intrinsic properties, we should expect to similar invasion rates regardless of the different placental ECM isolated from normal and preeclamptic pregnancies. A similar experimental set up could be done for

trophoblast isolated from normal pregnancies. Results from these experiments would provide some insights into the relative contributions of fetal trophoblast and maternal decidual microenvironments in preeclampsia.

Another study that would be worth pursing is to test the effect of shear stress on spiral arteries remodeling. It is well-established that during decidualization, the spiral arteries remodel and dilate slightly prior to the arrival of trophoblast [18]. However, the effect of these trophoblast-independent remodeling on the later trophoblast-dependent remodeling of spiral arteries is unclear. Our perfusion based bioreactor system uniquely permits the investigation on the effect of changing shear stress, resulting from trophoblast-independent remodeling, on the trophoblasts-mediated remodeling of the endothelial cells. Results from these experiments would shine lights on the importance of decidualization on trophoblast remodeling of the spiral arteries, an area that is largely unknown.

Bibliography

1. Khalili AA, Ahmad MR. A Review of Cell Adhesion Studies for Biomedical and Biological Applications. International Journal of Molecular Sciences. 2015;16(8):18149-84. doi: 10.3390/ijms160818149. PubMed PMID: WOS:000366826100078.

2. Christ KV, Turner KT. Methods to Measure the Strength of Cell Adhesion to Substrates. Journal of Adhesion Science and Technology. 2010;24(13-14):2027-58. doi: 10.1163/016942410x507911. PubMed PMID: WOS:000284152300001.

3. Friedrichs J, Helenius J, Muller DJ. Quantifying cellular adhesion to extracellular matrix components by single-cell force spectroscopy. Nature Protocols. 2010;5(7):1353-61. doi: 10.1038/nprot.2010.89. PubMed PMID: WOS:000279404800012.

4. Ridley AJ, Hall A. THE SMALL GTP-BINDING PROTEIN RHO REGULATES THE ASSEMBLY OF FOCAL ADHESIONS AND ACTIN STRESS FIBERS IN RESPONSE TO GROWTH-FACTORS. Cell. 1992;70(3):389-99. doi: 10.1016/0092-8674(92)90163-7. PubMed PMID: WOS:A1992JH12400004.

5. Kuo CY, Eranki A, Placone JK, Rhodes KR, Aranda-Espinoza H, Fernandes R, et al. Development of a 3D Printed, Bioengineered Placenta Model to Evaluate the Role of Trophoblast Migration in Preeclampsia. Acs Biomaterials Science & Engineering. 2016;2(10):1817-26. doi: 10.1021/acsbiomaterials.6b00031. PubMed PMID: WOS:000385213700017.

6. Christopher W. Redman ILS. Latest Advances in Understanding Preeclampsia. SCIENCE. 2005;308:1592-4.

7. Yuval Bdolah SAK, Benjamin P. Sachs. Recent advances in understanding of preeclampsia. Croat Med J. 2005;46(5).

8. Kilic F, Kayadibi Y, Yuksel MA, Adaletli I, Ustabasioglu FE, Oncul M, et al. Shear wave elastography of placenta: in vivo quantitation of placental elasticity in preeclampsia. Diagnostic and Interventional Radiology. 2015;21(3):202-7. doi: 10.5152/dir.2014.14338. PubMed PMID: WOS:000353976100003.

9. Young BC, Levine RJ, Karumanchi SA. Pathogenesis of preeclampsia. Annu Rev Pathol. 2010;5:173-92. Epub 2010/01/19. doi: 10.1146/annurev-pathol-121808-102149. PubMed PMID: 20078220.

10. Aubuchon M, Schulz LC, Schust DJ. Preeclampsia: animal models for a human cure. Proceedings of the National Academy of Sciences of the United States of America. 2011;108(4):1197-8. Epub 2011/01/15. doi: 10.1073/pnas.1018164108. PubMed PMID: 21233419; PubMed Central PMCID: PMC3029729.

11. Orendi K, Kivity V, Sammar M, Grimpel Y, Gonen R, Meiri H, et al. Placental and trophoblastic in vitro models to study preventive and therapeutic agents for preeclampsia. Placenta. 2011;32 Suppl:S49-54. Epub 2011/01/25. doi: 10.1016/j.placenta.2010.11.023. PubMed PMID: 21257083.

12. Lange JR, Fabry B. Cell and tissue mechanics in cell migration. Experimental Cell Research. 2013;319(16):2418-23. doi: 10.1016/j.yexcr.2013.04.023. PubMed PMID: WOS:000324659800004.

13. Whitley GS, Cartwright JE. Trophoblast-mediated spiral artery remodelling: a role for apoptosis. Journal of anatomy. 2009;215(1):21-6. Epub 2009/02/14. doi: 10.1111/j.1469-7580.2008.01039.x. PubMed PMID: 19215319; PubMed Central PMCID: PMC2714635.

14. Carter AM, Enders AC, Pijnenborg R. The role of invasive trophoblast in implantation and placentation of primates. Philosophical Transactions of the Royal Society B-Biological Sciences. 2015;370(1663):11. doi: 10.1098/rstb.2014.0070. PubMed PMID: WOS:000348139100010.

15. Cartwright JE, Kenny LC, Dash PR, Crocker IP, Aplin JD, Baker PN, et al. Trophoblast invasion of spiral arteries: a novel in vitro model. Placenta. 2002;23(2-3):232-5. Epub 2002/04/12. doi: 10.1053/plac.2001.0760. PubMed PMID: 11945091.

16. McMaster MT, Zhou Y, Fisher SJ. Abnormal placentation and the syndrome of preeclampsia. Seminars in Nephrology. 2004;24(6):540-7. doi: 10.1016/s0270-9295(04)00124-x. PubMed PMID: WOS:000225533900002.

17. Kaufmann P, Black S, Huppertz B. Endovascular trophoblast invasion: implications for the pathogenesis of intrauterine growth retardation and preeclampsia. Biology of reproduction. 2003;69(1):1-7. Epub 2003/03/07. doi: 10.1095/biolreprod.102.014977. PubMed PMID: 12620937.

18. Whitley GSJ, Cartwright JE. Trophoblast-mediated spiral artery remodelling: a role for apoptosis. Journal of Anatomy. 2009;215(1):21-6. doi: 10.1111/j.1469-7580.2008.01039.x. PubMed PMID: WOS:000266923900004.

19. Ganeff C, Chatel G, Munaut C, Frankenne F, Foidart JM, Winkler R. The IGF system in in-vitro human decidualization. Molecular Human Reproduction. 2009;15(1):27-38. doi: 10.1093/molehr/gan073. PubMed PMID: WOS:000263165300004.

20. Craven CM, Morgan T, Ward K. Decidual spiral artery remodelling begins before cellular interaction with cytotrophoblasts. Placenta. 1998;19(4):241-52. doi: 10.1016/s0143-4004(98)90055-8. PubMed PMID: WOS:000073767800002.

21. Kam EPY, Gardner L, Loke YW, King A. The role of trophoblast in the physiological change in decidual spiral arteries. Human Reproduction.

1999;14(8):2131-8. doi: 10.1093/humrep/14.8.2131. PubMed PMID: WOS:000081959700042.

22. Khong TY, Dewolf F, Robertson WB, Brosens I. INADEQUATE MATERNAL VASCULAR-RESPONSE TO PLACENTATION IN PREGNANCIES COMPLICATED BY PREECLAMPSIA AND BY SMALL-FOR-GESTATIONAL-AGE INFANTS. British Journal of Obstetrics and Gynaecology. 1986;93(10):1049-59. doi: 10.1111/j.1471-0528.1986.tb07830.x. PubMed PMID: WOS:A1986E654300005.

23. Pijnenborg R, Vercruysse L, Hanssens M. The uterine spiral arteries in human pregnancy: facts and controversies. Placenta. 2006;27(9-10):939-58. Epub 2006/02/24. doi: 10.1016/j.placenta.2005.12.006. PubMed PMID: 16490251.

24. Rogers PAW, Abberton KM. Endometrial arteriogenesis: Vascular smooth muscle cell proliferation and differentiation during the menstrual cycle and changes associated with endometrial bleeding disorders. Microscopy Research and Technique. 2003;60(4):412-9. doi: 10.1002/jemt.10279. PubMed PMID: WOS:000180968400004.

25. Huang A, Sun D, Koller A, Kaley G. 17 beta-estradiol restores endothelial nitric oxide release to shear stress in arterioles of male hypertensive rats. Circulation. 2000;101(1):94-100. PubMed PMID: WOS:000084664200019.

26. Aberdeen GW, Wiegand SJ, Bonagura TW, Pepe GJ, Albrecht ED. Vascular Endothelial Growth Factor Mediates the Estrogen-Induced Breakdown of Tight Junctions between and Increase in Proliferation of Microvessel Endothelial Cells in the Baboon Endometrium. Endocrinology. 2008;149(12):6076-83. doi: 10.1210/en.2008-0521. PubMed PMID: WOS:000261156300023.

27. Sentman CL, Meadows SK, Wira CR, Eriksson M. Recruitment of uterine NK cells: Induction of CXC chemokine ligands 10 and 11 in human endometrium by estradiol and progesterone. Journal of Immunology. 2004;173(11):6760-6. PubMed PMID: WOS:000225307500033.

28. Red-Horse K, Kapidzic M, Zhou Y, Feng KT, Singh H, Fisher SJ. EPHB4 regulates chemokine-evoked trophoblast responses: a mechanism for incorporating the human placenta into the maternal circulation. Development. 2005;132(18):4097-106. doi: 10.1242/dev.01971. PubMed PMID: WOS:000232579600008.

29. Nakatsuji Y, Nishio Y, Tani N, Adachi K, Ohmichi M, Hisamoto K, et al. Epidermal growth factor enhances invasive activity of BeWo choriocarcinoma cells by inducing alpha 2 integrin expression. Endocrine Journal. 2003;50(6):703-14. doi: 10.1507/endocrj.50.703. PubMed PMID: WOS:000187973400009.

30. McCarthy FP, Kingdom JC, Kenny LC, Walsh SK. Animal models of preeclampsia; uses and limitations. Placenta. 2011;32(6):413-9. Epub 2011/04/19. doi: 10.1016/j.placenta.2011.03.010. PubMed PMID: 21497901.

31. Vicovac L, Aplin JD. Epithelial-mesenchymal transition during trophoblast differentiation. Acta Anatomica. 1996;156(3):202-16. PubMed PMID: WOS:A1996WF80300006.

32. Ackland ML, Newgreen DF, Fridman M, Waltham MC, Arvanitis A, Minichiello J, et al. Epidermal growth factor-induced epithelio-mesenchymal transition in human breast carcinoma cells. Laboratory Investigation. 2003;83(3):435-48. doi: 10.1097/01.lab.0000059927.97515.fd. PubMed PMID: WOS:000181849400015.

33. Ahmed N, Maines-Bandiera S, Quinn MA, Unger WG, Dedhar S, Auersperg N. Molecular pathways regulating EGF-induced epithelio-mesenchymal transition in human ovarian surface epithelium. American Journal of Physiology-Cell Physiology. 2006;290(6):C1532-C42. doi: 10.1152/ajpcell.00478.2005. PubMed PMID: WOS:000237407600009.

34. Zeisberg M, Neilson EG. Biomarkers for epithelial-mesenchymal transitions. Journal of Clinical Investigation. 2009;119(6):1429-37. doi: 10.1172/jci36183. PubMed PMID: WOS:000266601000007.

35. Lamouille S, Xu J, Derynck R. Molecular mechanisms of epithelial-mesenchymal transition. Nature Reviews Molecular Cell Biology. 2014;15(3):178-96. doi: 10.1038/nrm3758. PubMed PMID: WOS:000332000300011.

36. DaSilva-Arnold S, James JL, Al-Khan A, Zamudio S, Illsley NP. Differentiation of first trimester cytotrophoblast to extravillous trophoblast involves an epithelial-mesenchymal transition. Placenta. 2015;36(12):1412-8. doi: 10.1016/j.placenta.2015.10.013. PubMed PMID: WOS:000366950500010.

37. Davies JE, Pollheimer J, Yong HEJ, Kokkinos MI, Kalionis B, Knofler M, et al. Epithelial-mesenchymal transition during extravillous trophoblast differentiation. Cell Adhesion & Migration. 2016;10(3):310-21. doi: 10.1080/19336918.2016.1170258. PubMed PMID: WOS:000379261600007.

38. Holtan SG, Creedon DJ, Haluska P, Markovic SN. Cancer and Pregnancy: Parallels in Growth, Invasion, and Immune Modulation and Implications for Cancer Therapeutic Agents. Mayo Clinic Proceedings. 2009;84(11):985-1000. PubMed PMID: WOS:000271486900006.

39. Peracoli MTS, Menegon FTF, Borges VTM, Costa R, Thomazini-Santos IA, Peracoli JC. Platelet aggregation and TGF-beta(1) plasma levels in pregnant women with preeclampsia. Journal of Reproductive Immunology. 2008;79(1):79-84. doi: 10.1016/j.jri.2008.08.001. PubMed PMID: WOS:000260989000011.

40. Djurovic S, Schjetlein R, Wisloff F, Haugen G, Husby H, Berg K. Plasma concentrations of Lp(a) lipoprotein and TGF-beta(1) are altered in preeclampsia. Clinical Genetics. 1997;52(5):371-6. PubMed PMID: WOS:000072004100016.

41. Caniggia I, Grisaru-Gravnosky S, Kuliszewsky M, Post M, Lye SJ. Inhibition of TGF-beta(3) restores the invasive capability of extravillous trophoblasts in preeclamptic pregnancies. Journal of Clinical Investigation. 1999;103(12):1641-50. doi: 10.1172/jci6380. PubMed PMID: WOS:000083468200006.

42. Moller B, Rasmussen C, Lindblom B, Olovsson M. Expression of the angiogenic growth factors VEGF, FGF-2, EGF and their receptors in normal human endometrium during the menstrual cycle. Molecular Human Reproduction. 2001;7(1):65-72. doi: 10.1093/molehr/7.1.65. PubMed PMID: WOS:000166460800010.

43. Crosley EJ, Dunk CE, Beristain AG, Christians JK. IGFBP-4 and-5 are expressed in first-trimester villi and differentially regulate the migration of HTR-8/SVneo cells. Reproductive Biology and Endocrinology. 2014;12:1-7. doi: 10.1186/1477-7827-12-123. PubMed PMID: WOS:000348475000001.

44. Halhali A, Diaz L, Barrera D, Avila E, Larrea F. Placental calcitriol synthesis and IGF-I levels in normal and preeclamptic pregnancies. Journal of Steroid Biochemistry and Molecular Biology. 2014;144:44-9. doi: 10.1016/j.jsbmb.2013.12.014. PubMed PMID: WOS:000345182900008.

45. Larsson A, Palm M, Basu S, Axelsson O. Insulin-like growth factor binding protein-1 (IGFBP-1) during normal pregnancy. Gynecological Endocrinology. 2013;29(2):129-32. doi: 10.3109/09513590.2012.730574. PubMed PMID: WOS:000313664000011.

46. Sifakis S, Akolekar R, Kappou D, Mantas N, Nicolaides KH. Maternal serum insulin-like growth factor-I at 11-13 weeks in preeclampsia. Prenatal Diagnosis. 2010;30(11):1026-31. doi: 10.1002/pd.2555. PubMed PMID: WOS:000284022900003.

47. Armant DR, Fritz R, Kilburn BA, Kim YM, Nien JK, Maihle NJ, et al. Reduced expression of the epidermal growth factor signaling system in preeclampsia. Placenta. 2015;36(3):270-8. doi: 10.1016/j.placenta.2014.12.006. PubMed PMID: WOS:000350778200003.

48. Brzezinski J, Lewinski A. Increased plasma concentration of epidermal growth factor in female patients with non-toxic nodular goitre. European Journal of Endocrinology. 1998;138(4):388-93. doi: 10.1530/eje.0.1380388. PubMed PMID: WOS:000073116600010.

49. Forbes K, Westwood M. Maternal growth factor regulation of human placental development and fetal growth. Journal of Endocrinology. 2010;207(1):1-16. doi: 10.1677/joe-10-0174. PubMed PMID: WOS:000282528100001.

50. Burton GJ, Charnock-Jones DS, Jauniaux E. Regulation of vascular growth and function in the human placenta. Reproduction. 2009;138(6):895-902. Epub 2009/05/28. doi: 10.1530/REP-09-0092. PubMed PMID: 19470597.

51. Large MJ, Wetendorf M, Lanz RB, Hartig SM, Creighton CJ, Mancini MA, et al. The Epidermal Growth Factor Receptor Critically Regulates Endometrial Function during Early Pregnancy. Plos Genetics. 2014;10(6). doi: 10.1371/journal.pgen.1004451. PubMed PMID: WOS:000338847700060.

52. Luo J, Manning BD, Cantley LC. Targeting the PI3K-Akt pathway in human cancer: Rationale and promise. Cancer Cell. 2003;4(4):257-62. doi: 10.1016/s1535-6108(03)00248-4. PubMed PMID: WOS:000186154200006.

53. Watanabe H. Epidermal growth factor in urine of pregnant women and in amniotic fluid throughout pregnancy. Gynecological endocrinology. 1990;4:43-50.

54. Kim YJ, Lee GS, Hyun SH, Ka HH, Choi KC, Lee CK, et al. Uterine Expression of Epidermal Growth Factor Family During the Course of Pregnancy in Pigs. Reproduction in Domestic Animals. 2009;44(5):797-804. doi: 10.1111/j.1439-0531.2008.01082.x. PubMed PMID: WOS:000269877800013.

55. Qiu Q, Yang M, Tsang BK, Gruslin A. EGF-induced trophoblast secretion of MMP-9 and TIMP-1 involves activation of both PI3K and MAPK signalling pathways. Reproduction. 2004;128(3):355-63. doi: 10.1530/rep.1.00234. PubMed PMID: WOS:000223790200011.

56. Mimura Y, Ihn H, Jinnin M, Asano Y, Yamane K, Tamaki K. Epidermal growth factor induces fibronectin expression in human dermal fibroblasts via protein kinase C delta signaling pathway. Journal of Investigative Dermatology. 2004;122(6):1390-8. doi: 10.1111/j.0022-202X.2004.22618.x. PubMed PMID: WOS:000221693500010.

57. Park J, Schwarzbauer JE. Mammary epithelial cell interactions with fibronectin stimulate epithelial-mesenchymal transition. Oncogene. 2014;33(13):1649-57. doi: 10.1038/onc.2013.118. PubMed PMID: WOS:000334344700005.

58. Egginton S, Hussain A, Hall-Jones J, Chaudhry B, Syeda F, Glen KE. Shear stress-induced angiogenesis in mouse muscle is independent of the vasodilator mechanism and quickly reversible. Acta Physiologica. 2016;218(3):153-66. doi: 10.1111/apha.12728. PubMed PMID: WOS:000385833800003.

59. Demidova-Rice TN, Hamblin MR, Herman IM. Acute and Impaired Wound Healing: Pathophysiology and Current Methods for Drug Delivery, Part 1: Normal and Chronic Wounds: Biology, Causes, and Approaches to Care. Advances in Skin & Wound Care. 2012;25(7):304-14. doi: 10.1097/01.ASW.0000416006.55218.d0. PubMed PMID: WOS:000305640700004.

60. Chen JS, Wang Q, Fu XH, Huang XH, Chen XL, Cao LQ, et al. Involvement of PI3K/PTEN/AKT/mTOR pathway in invasion and metastasis in hepatocellular carcinoma: Association with MMP-9. Hepatology Research. 2009;39(2):177-86. doi: 10.1111/j.1872-034X.2008.00449.x. PubMed PMID: WOS:000262640700009.

61. Pino A, Fumagalli G, Bifari F, Decimo I. New neurons in adult brain: distribution, molecular mechanisms and therapies. Biochemical Pharmacology. 2017;141:4-22. doi: 10.1016/j.bcp.2017.07.003. PubMed PMID: WOS:000411656600002.

62. Cancer Statistics: National Cancer Institute; 2017 [cited 2017 10/16]. Available from: https://www.cancer.gov/about-cancer/understanding/statistics.

63. Edmondson R, Broglie JJ, Adcock AF, Yang LJ. Three-Dimensional Cell Culture Systems and Their Applications in Drug Discovery and Cell-Based Biosensors. Assay and Drug Development Technologies. 2014;12(4):207-18. doi: 10.1089/adt.2014.573. PubMed PMID: WOS:000335982500002.

64. Antoni D, Burckel H, Josset E, Noel G. Three-Dimensional Cell Culture: A Breakthrough in Vivo. International Journal of Molecular Sciences. 2015;16(3):5517-27. doi: 10.3390/ijms16035517. PubMed PMID: WOS:000352955500067.

65. Shamir ER, Ewald AJ. Three-dimensional organotypic culture: experimental models of mammalian biology and disease. Nature Reviews Molecular Cell Biology. 2014;15(10):647-64. doi: 10.1038/nrm3873. PubMed PMID: WOS:000342548600010.

66. Tomei AA, Boschetti F, Gervaso F, Swartz MA. 3D Collagen Cultures Under Well-Defined Dynamic Strain: A Novel Strain Device With a Porous Elastomeric Support. Biotechnology and Bioengineering. 2009;103(1):217-25. doi: 10.1002/bit.22236. PubMed PMID: WOS:000265283000018.

67. Demir R, Yaba A, Huppertz B. Vasculogenesis and angiogenesis in the endometrium during menstrual cycle and implantation. Acta Histochemica. 2010;112(3):203-14. doi: 10.1016/j.acthis.2009.04.004. PubMed PMID: WOS:000277578900001.

68. Fedorovich NE, Alblas J, Hennink WE, Oner FC, Dhert WJ. Organ printing: the future of bone regeneration? Trends in biotechnology. 2011;29(12):601-6. Epub 2011/08/13. doi: 10.1016/j.tibtech.2011.07.001. PubMed PMID: 21831463.

69. Song JW, Munn LL. Fluid forces control endothelial sprouting. Proceedings of the National Academy of Sciences of the United States of America. 2011;108(37):15342-7. doi: 10.1073/pnas.1105316108. PubMed PMID: WOS:000294804900070.

70. Kim S, Chung M, Ahn J, Lee S, Jeon NL. Interstitial flow regulates the angiogenic response and phenotype of endothelial cells in a 3D culture model. Lab on a Chip. 2016;16(21):4189-99. doi: 10.1039/c6lc00910g. PubMed PMID: WOS:000386311100014.

71. Belair DG, Whisler JA, Valdez J, Velazquez J, Molenda JA, Vickerman V, et al. Human Vascular Tissue Models Formed from Human Induced Pluripotent Stem Cell Derived Endothelial Cells. Stem Cell Reviews and Reports. 2015;11(3):511-25. doi: 10.1007/s12015-014-9549-5. PubMed PMID: WOS:000355661300013.

72. Trkov S, Eng G, Di Liddo R, Parnigotto PP, Vunjak-Novakovic G. Micropatterned three-dimensional hydrogel system to study human endothelial - mesenchymal stem cell interactions. Journal of Tissue Engineering and Regenerative Medicine. 2010;4(3):205-15. doi: 10.1002/term.231. PubMed PMID: WOS:000277121500004.

73. Hadjizadeh A, Doillon CJ. Directional migration of endothelial cells towards angiogenesis using polymer fibres in a 3D co-culture system. Journal of Tissue Engineering and Regenerative Medicine. 2010;4(7):524-31. doi: 10.1002/term.269. PubMed PMID: WOS:000282837900004.

74. Turturro MV, Christenson MC, Larson JC, Young DA, Brey EM, Papavasiliou G. MMP-Sensitive PEG Diacrylate Hydrogels with Spatial Variations in Matrix Properties Stimulate Directional Vascular Sprout Formation. Plos One. 2013;8(3). doi: 10.1371/journal.pone.0058897. PubMed PMID: WOS:000316252500055.

75. Trappmann B, Baker BM, Polacheck WJ, Choi CK, Burdick JA, Chen CS. Matrix degradability controls multicellularity of 3D cell migration. Nature Communications. 2017;8. doi: 10.1038/s41467-017-00418-6. PubMed PMID: WOS:000408547200002.

76. Hardwicke J, Schmaljohann D, Boyce D, Thomas D. Epidermal growth factor therapy and wound healing - past, present and future. Surgeon-Journal of the Royal Colleges of Surgeons of Edinburgh and Ireland. 2008;6(3):172-7. PubMed PMID: WOS:000256684700010.

77. Chen SX, Liu B, Carlson MA, Gombart AF, Reilly DA, Xie JW. Recent advances in electrospun nanofibers for wound healing. Nanomedicine. 2017;12(11):1335-52. doi: 10.2217/nnm-2017-0017. PubMed PMID: WOS:000403098600011.

78. Kuo C-Y, Wilson E, Fuson A, Gandhi N, Reza M, Jenkins A, et al. Repair of Tympanic Membrane Perforations with Customized, Bioprinted Ear Grafts Using Chinchilla Models. Tissue Engineering Part A. 2017. Epub July 20th, 2017.

79. Grasman JM, Page RL, Pins GD. Design of an In Vitro Model of Cell Recruitment for Skeletal Muscle Regeneration Using Hepatocyte Growth Factor-Loaded Fibrin Microthreads. Tissue Engineering Part A. 2017;23(15-16):773-83. doi: 10.1089/ten.tea.2016.0440. PubMed PMID: WOS:000407673600006.

80. Aizawa Y, Shoichet MS. The role of endothelial cells in the retinal stem and progenitor cell niche within a 3D engineered hydrogel matrix. Biomaterials. 2012;33(21):5198-205. doi: 10.1016/j.biomaterials.2012.03.062. PubMed PMID: WOS:000305105400003.

81. Muerza-Cascante ML, Shokoohmand A, Khosrotehrani K, Haylock D, Dalton PD, Hutmacher DW, et al. Endosteal-like extracellular matrix expression on melt electrospun written scaffolds. Acta Biomaterialia. 2017;52:145-58. doi: 10.1016/j.actbio.2016.12.040. PubMed PMID: WOS:000401043100015.

82. Mosser DM, Edwards JP. Exploring the full spectrum of macrophage activation. Nature Reviews Immunology. 2008;8(12):958-69. doi: 10.1038/nri2448. PubMed PMID: WOS:000261197200015.

83. Murray PJ, Wynn TA. Protective and pathogenic functions of macrophage subsets. Nature Reviews Immunology. 2011;11(11):723-37. doi: 10.1038/nri3073. PubMed PMID: WOS:000296584700011.

84. Budczies J, von Winterfeld M, Klauschen F, Bockmayr M, Lennerz JK, Denkert C, et al. The landscape of metastatic progression patterns across major human cancers. Oncotarget. 2015;6(1):570-83. PubMed PMID: WOS:000352065200045.

85. Steeg PS. Tumor metastasis: mechanistic insights and clinical challenges. Nature Medicine. 2006;12(8):895-904. doi: 10.1038/nm1469. PubMed PMID: WOS:000239626200019.

86. Quail DF, Joyce JA. Microenvironmental regulation of tumor progression and metastasis. Nature Medicine. 2013;19(11):1423-37. doi: 10.1038/nm.3394. PubMed PMID: WOS:000326920300020.

87. Carey SP, Starchenko A, McGregor AL, Reinhart-King CA. Leading malignant cells initiate collective epithelial cell invasion in a three-dimensional heterotypic tumor spheroid model. Clinical & Experimental Metastasis. 2013;30(5):615-30. doi: 10.1007/s10585-013-9565-x. PubMed PMID: WOS:000319345900007.

88. Gioiella F, Urciuolo F, Imparato G, Brancato V, Netti PA. An Engineered Breast Cancer Model on a Chip to Replicate ECM-Activation In Vitro during Tumor Progression. Advanced Healthcare Materials. 2016;5(23):3074-84. doi: 10.1002/adhm.201600772. PubMed PMID: WOS:000389920100012.

89. Hockemeyer K, Janetopoulos C, Terekhov A, Hofmeister W, Vilgelm A, Costa L, et al. Engineered three-dimensional microfluidic device for interrogating cell-cell interactions in the tumor microenvironment. Biomicrofluidics. 2014;8(4). doi: 10.1063/1.4890330. PubMed PMID: WOS:000344225400010.

90. Estrada MF, Rebelo SP, Davies EJ, Pinto MT, Pereira H, Santo VE, et al. Modelling the tumour microenvironment in long-term microencapsulated 3D co-cultures recapitulates phenotypic features of disease progression. Biomaterials. 2016;78:50-61. doi: 10.1016/j.biomaterials.2015.11.030. PubMed PMID: WOS:000368955200006.

91. Boghaert E, Gleghorn JP, Lee K, Gjorevski N, Radisky DC, Nelson CM. Host epithelial geometry regulates breast cancer cell invasiveness. Proceedings of the National Academy of Sciences of the United States of America. 2012;109(48):19632-7. doi: 10.1073/pnas.1118872109. PubMed PMID: WOS:000312313900033.

92. DelNero P, Lane M, Verbridge SS, Kwee B, Kermani P, Hempstead B, et al. 3D culture broadly regulates tumor cell hypoxia response and angiogenesis via pro-inflammatory pathways. Biomaterials. 2015;55:110-8. doi: 10.1016/j.biomaterials.2015.03.035. PubMed PMID: WOS:000355043400010.

93. Nietzer S, Baur F, Sieber S, Hansmann J, Schwarz T, Stoffer C, et al. Mimicking Metastases Including Tumor Stroma: A New Technique to Generate a Three-Dimensional Colorectal Cancer Model Based on a Biological Decellularized Intestinal Scaffold. Tissue Engineering Part C-Methods. 2016;22(7):621-35. doi: 10.1089/ten.tec.2015.0557. PubMed PMID: WOS:000380803200001.

94. Nyga A, Loizidou M, Emberton M, Cheema U. A novel tissue engineered three-dimensional in vitro colorectal cancer model. Acta Biomaterialia. 2013;9(8):7917-26. doi: 10.1016/j.actbio.2013.04.028. PubMed PMID: WOS:000322207700032.

95. Magdeldin T, Lopez-Davila V, Pape J, Cameron GWW, Emberton M, Loizidou M, et al. Engineering a vascularised 3D in vitro model of cancer progression. Scientific Reports. 2017;7. doi: 10.1038/srep44045. PubMed PMID: WOS:000396135400001.

96. Okochi M, Matsumura T, Yamamoto S, Nakayama E, Jimbow K, Honda H. Cell behavior observation and gene expression analysis of melanoma associated with stromal fibroblasts in a three-dimensional magnetic cell culture array. Biotechnology Progress. 2013;29(1):135-42. doi: 10.1002/btpr.1642. PubMed PMID: WOS:000314472200017.

97. Marques CMD, MacNeil S. Use of a Tissue Engineered Human Skin Model to Investigate the Effects of Wounding and of an Anti-Inflammatory on Melanoma Cell Invasion. Plos One. 2016;11(6). doi: 10.1371/journal.pone.0156931. PubMed PMID: WOS:000377561000051.

98. Acerbi I, Cassereau L, Dean I, Shi Q, Au A, Park C, et al. Human breast cancer invasion and aggression correlates with ECM stiffening and immune cell infiltration. Integrative Biology. 2015;7(10):1120-34. doi: 10.1039/c5ib00040h. PubMed PMID: WOS:000366717300004.

99. Baish JW, Gazit Y, Berk DA, Nozue M, Baxter LT, Jain RK. Role of tumor vascular architecture in nutrient and drug delivery: An invasion percolation-based network model. Microvascular Research. 1996;51(3):327-46. doi: 10.1006/mvre.1996.0031. PubMed PMID: WOS:A1996UK97700005.

100. Dickson BJ. Molecular mechanisms of axon guidance. Science. 2002;298(5600):1959-64. doi: 10.1126/science.1072165. PubMed PMID: WOS:000179629200036.

101. Romano NH, Lampe KJ, Xu H, Ferreira MM, Heilshorn SC. Microfluidic Gradients Reveal Enhanced Neurite Outgrowth but Impaired Guidance within 3D Matrices with High Integrin Ligand Densities. Small. 2015;11(6):722-30. doi: 10.1002/smll.201401574. PubMed PMID: WOS:000349977500010.

102. Koivisto JT, Joki T, Parraga JE, Paakkonen R, Yla-Outinen L, Salonen L, et al. Bioamine-crosslinked gellan gum hydrogel for neural tissue engineering. Biomedical Materials. 2017;12(2). doi: 10.1088/1748-605X/aa62b0. PubMed PMID: WOS:000397532300008.

103. !!! INVALID CITATION !!! {}.

104. Lancaster MA, Corsini NS, Wolfinger S, Gustafson EH, Phillips AW, Burkard TR, et al. Guided self-organization and cortical plate formation in human brain organoids. Nature Biotechnology. 2017;35(7):659-+. doi: 10.1038/nbt.3906. PubMed PMID: WOS:000405310300018.

105. Gingras M, Beaulieu MM, Gagnon V, Durham HD, Berthod F. In vitro study of axonal migration and myelination of motor neurons in a three-dimensional tissue-engineered model. Glia. 2008;56(3):354-64. doi: 10.1002/glia.20617. PubMed PMID: WOS:000252585900010.

106. Weller RO, Djuanda E, Yow HY, Carare RO. Lymphatic drainage of the brain and the pathophysiology of neurological disease. Acta Neuropathologica. 2009;117(1):1-14. doi: 10.1007/s00401-008-0457-0. PubMed PMID: WOS:000261185200001.

107. Eric A P Steegers PvD, Johannes J Duvekot, Robert Pijnenborg. Pre-eclampsia. The Lancet. 2010;376:631-44. doi: 10.1016/s01406736(10)60279-6.

108. Aldo PB, Krikun G, Visintin I, Lockwood C, Romero R, Mor G. A novel three-dimensional in vitro system to study trophoblast-endothelium cell interactions. American Journal of Reproductive Immunology. 2007;58(2):98-110. doi: 10.1111/j.1600-0897.2007.00493.x. PubMed PMID: WOS:000247965900002.

109. Pathak A, Kumar S. Independent regulation of tumor cell migration by matrix stiffness and confinement. Proceedings of the National Academy of Sciences of the United States of America. 2012;109(26):10334-9. doi: 10.1073/pnas.1118073109. PubMed PMID: WOS:000306291400053.

110. Santoro M, Lamhamedi-Cherradi SE, Menegaz BA, Ludwig JA, Mikos AG. Flow perfusion effects on three-dimensional culture and drug sensitivity of Ewing sarcoma. Proceedings of the National Academy of Sciences of the United States of America. 2015;112(33):10304-9. doi: 10.1073/pnas.1506684112. PubMed PMID: WOS:000359738300057.

111. Yeatts AB, Both SK, Yang WX, Alghamdi HS, Yang F, Fisher JP, et al. In Vivo Bone Regeneration Using Tubular Perfusion System Bioreactor Cultured Nanofibrous Scaffolds. Tissue Engineering Part A. 2014;20(1-2):139-46. doi: 10.1089/ten.tea.2013.0168. PubMed PMID: WOS:000337280600013.

112. Kundu J, Shim JH, Jang J, Kim SW, Cho DW. An additive manufacturing-based PCL-alginate-chondrocyte bioprinted scaffold for cartilage tissue engineering. Journal of Tissue Engineering and Regenerative Medicine. 2015;9(11):1286-97. doi: 10.1002/term.1682. PubMed PMID: WOS:000364520300009.

113. Topman G, Shoham N, Sharabani-Yosef O, Lin FH, Gefen A. A new technique for studying directional cell migration in a hydrogel-based three-dimensional matrix for tissue engineering model systems. Micron. 2013;51:9-12. doi: 10.1016/j.micron.2013.06.002. PubMed PMID: WOS:000324784100002.

114. Tang Q, Piard C, Lin J, Nan K, Guo T, Caccamese J, et al. Imaging stem cell distribution, growth, migration, and differentiation in 3-D scaffolds for bone tissue engineering using mesoscopic fluorescence tomography. Biotechnol Bioeng. 2017;Accepted Author Manuscript. doi: 10.1002/bit.26452.

115. Portillo-Lara R, Annabi N. Microengineered cancer-on-a-chip platforms to study the metastatic microenvironment. Lab on a Chip. 2016;16(21):4063-81. doi: 10.1039/c6lc00718j. PubMed PMID: WOS:000386311100002.

116. Nguyen BNB, Ko H, Moriarty RA, Etheridge JM, Fisher JP. Dynamic Bioreactor Culture of High Volume Engineered Bone Tissue. Tissue Engineering Part A. 2016;22(3-4):263-71. doi: 10.1089/ten.tea.2015.0395. PubMed PMID: WOS:000369987900009.

117. Yeatts AB, Gordon CN, Fisher JP. Formation of an Aggregated Alginate Construct in a Tubular Perfusion System. Tissue Engineering Part C-Methods. 2011;17(12):1171-8. doi: 10.1089/ten.tec.2011.0263. PubMed PMID: WOS:000298078300003.

118. Yeatts AB, Geibel EM, Fears FF, Fisher JP. Human mesenchymal stem cell position within scaffolds influences cell fate during dynamic culture. Biotechnology and Bioengineering. 2012;109(9):2381-91. doi: 10.1002/bit.24497. PubMed PMID: WOS:000306759500022.

119. Rustad KC, Sorkin M, Levi B, Longaker MT, Gurtner GC. Strategies for organ level tissue engineering. Organogenesis. 2010;6(3):151-7. doi: 10.4161/org.6.3.12139. PubMed PMID: WOS:000290266200003.

120. Zhang YY, He YJ, Bharadwaj S, Hammam N, Carnagey K, Myers R, et al. Tissue-specific extracellular matrix coatings for the promotion of cell proliferation and maintenance of cell phenotype. Biomaterials. 2009;30(23-24):4021-8. doi: 10.1016/j.biomaterials.2009.04.005. PubMed PMID: WOS:000267469300024.

121. Tinnakorn Chaiworapongsa PC, Lami Yeo and Roberto Romero. Pre-eclampsia part 1: current understanding of its paothophsiology. Nature Nephrology. 2014;10.

122. Mohd Nordin Noraihan PSaABEJ. Report of 50 cases of eclampsia. 2005;31(4):302-9.

123. Hunkapiller NM, Fisher SJ. PLACENTAL REMODELING OF THE UTERINE VASCULATURE. Angiogenesis: in Vivo Systems, Pt B. 2008;445:281-+. doi: 10.1016/s0076-6879(08)03012-7. PubMed PMID: WOS:000260774900012.

124. Tinnakorn Chaiworapongsa PC, Lami Yeo and Roberto Romero. Pre-eclampsia part 2: prediction, prevention and management. Nature Reviews Nephrology. 2014;10:531-40.

125. Adu-Bonsaffoh K, Oppong SA, Binlinla G, Obed SA. Maternal deaths attributable to hypertensive disorders in a tertiary hospital in Ghana. Int J Gynaecol Obstet. 2013;123(2):110-3. Epub 2013/08/24. doi: 10.1016/j.ijgo.2013.05.017. PubMed PMID: 23969337.

126. Sibai B, Dekker G, Kupferminc M. Pre-eclampsia. The Lancet. 2005;365(9461):785-99. doi: 10.1016/s0140-6736(05)17987-2.

127. Aubuchon M, Schulz LC, Schust DJ. Preeclampsia: animal models for a human cure. Proceedings of the National Academy of Sciences of the United States of America. 2011;108(4):1197-8. Epub 2011/01/15. doi: 10.1073/pnas.1018164108. PubMed PMID: 21233419; PubMed Central PMCID: PMC3029729.

128. Kolesky DB, Truby RL, Gladman AS, Busbee TA, Homan KA, Lewis JA. 3D bioprinting of vascularized, heterogeneous cell-laden tissue constructs. Advanced materials. 2014;26(19):3124-30. Epub 2014/02/20. doi: 10.1002/adma.201305506. PubMed PMID: 24550124.

129. Billiet T, Gevaert E, De Schryver T, Cornelissen M, Dubruel P. The 3D printing of gelatin methacrylamide cell-laden tissue-engineered constructs with high cell viability. Biomaterials. 2014;35(1):49-62. Epub 2013/10/12. doi: 10.1016/j.biomaterials.2013.09.078. PubMed PMID: 24112804.

130. De Cock LJ, De Wever O, Hammad H, Lambrecht BN, Vanderleyden E, Dubruel P, et al. Engineered 3D microporous gelatin scaffolds to study cell migration. Chemical communications. 2012;48(29):3512-4. Epub 2012/03/02. doi: 10.1039/c2cc17006j. PubMed PMID: 22378164.

131. An I. Van Den Bulke BB, Nadine De Rooze, Etienne H. Schacht, Maria Cornelissen, and Hugo Berghmans. Structural and Rheological Properties of Methacrylamide Modified Gelatin Hydrogels. Biomacromolecules. 2000;1(1):31-8.

132. Kaemmerer E, Melchels FP, Holzapfel BM, Meckel T, Hutmacher DW, Loessner D. Gelatine methacrylamide-based hydrogels: an alternative three-dimensional cancer cell culture system. Acta biomaterialia. 2014;10(6):2551-62. Epub 2014/03/05. doi: 10.1016/j.actbio.2014.02.035. PubMed PMID: 24590158.

133. Santoro M, Tatara AM, Mikos AG. Gelatin carriers for drug and cell delivery in tissue engineering. Journal of controlled release : official journal of the Controlled Release Society. 2014;190:210-8. Epub 2014/04/22. doi: 10.1016/j.jconrel.2014.04.014. PubMed PMID: 24746627; PubMed Central PMCID: PMC4142078.

134. Miller K, Chinzei K. Mechanical properties of brain tissue in tension. Journal of Biomechanics. 2002;35(4):483-90. doi: 10.1016/s0021-9290(01)00234-2. PubMed PMID: WOS:000175407100009.

135. Umale S, Deck C, Bourdet N, Dhumane P, Soler L, Marescaux J, et al. Experimental mechanical characterization of abdominal organs: liver, kidney & spleen. Journal of the Mechanical Behavior of Biomedical Materials. 2013;17:22-33. doi: 10.1016/j.jmbbm.2012.07.010. PubMed PMID: WOS:000313230400003.

136. Hu J, Klinich KD, Miller CS, Nazmi G, Pearlman MD, Schneider LW, et al. Quantifying dynamic mechanical properties of human placenta tissue using optimization techniques with specimen-specific finite-element models. Journal of biomechanics. 2009;42(15):2528-34. Epub 2009/08/12. doi: 10.1016/j.jbiomech.2009.07.003. PubMed PMID: 19665131.

137. Hellinger JC, Medina LS, Epelman M. Pediatric Advanced Imaging and Informatics: State of the Art. Seminars in Ultrasound Ct and Mri. 2010;31(2):171-93. doi: 10.1053/j.sult.2010.01.003. PubMed PMID: WOS:000276295500010.

138. Soliman AA, Wojcinski S, Degenhardt F. Ultrasonographic examination of the endometrium and myometrium using acoustic radiation force impulse (ARFI) imaging technology: An initial experience with a new method. Clinical Hemorheology and Microcirculation. 2015;59(3):235-43. doi: 10.3233/ch-141842. PubMed PMID: WOS:000351948800005.

139. Liu L, Zhao G, Fan H, Zhao X, Li P, Wang Z, et al. Mesenchymal Stem Cells Ameliorate Thi-Induced Pre-Eclampsia-Like Symptoms in Mice via the Supression of TNF-a Expression. PLOS ONE: PLOS; 2014.

140. Huang Y, Wu Y, Chang X, Li Y, Wang W, Duan T. Effects of Human Umbilical Cord Mesenchymal Stem Cells on Human Trophoblast Cell Functions In Vitro. Stem Cells International: Hindawi Publishing Corporation; 2015.

141. Wang HB, Dey SK. Roadmap to embryo implantation: clues from mouse models. Nature Reviews Genetics. 2006;7(3):185-99. doi: 10.1038/nrg1808. PubMed PMID: WOS:000235384300014.

142. Nichol JW, Koshy ST, Bae H, Hwang CM, Yamanlar S, Khademhosseini A. Cell-laden microengineered gelatin methacrylate hydrogels. Biomaterials. 2010;31(21):5536-44. Epub 2010/04/27. doi: 10.1016/j.biomaterials.2010.03.064. PubMed PMID: 20417964; PubMed Central PMCID: PMC2878615.

143. Vanstroebiezen SAM, Everaerts FM, Janssen LJJ, Tacken RA. DIFFUSION-COEFFICIENTS OF OXYGEN, HYDROGEN-PEROXIDE AND GLUCOSE IN A HYDROGEL. Analytica Chimica Acta. 1993;273(1-2):553-60. doi: 10.1016/0003-2670(93)80202-v. PubMed PMID: WOS:A1993KM93400065.

144. C.-P.Chen. Placental Extracellular Matrix- Gene Expression, Deposition by Placental Fibroblasts and the Effect of Oxygen. Placenta. 2003;24:316-25. doi: 10.1053/plac.2002.0904.

145. Vertelov G, Kharazi L, Muralidhar MG, Sanati G, Tankovich T, Kharazi A. High targeted migration of human mesenchymal stem cells grown in hypoxia is associated with enhanced activation of RhoA. Stem Cell Research & Therapy. 2013;4. doi: 10.1186/scrt153. PubMed PMID: WOS:000314722500002.

146. Schuurman W, Levett PA, Pot MW, van Weeren PR, Dhert WJ, Hutmacher DW, et al. Gelatin-methacrylamide hydrogels as potential biomaterials for fabrication of tissue-engineered cartilage constructs. Macromolecular bioscience. 2013;13(5):551-61. Epub 2013/02/20. doi: 10.1002/mabi.201200471. PubMed PMID: 23420700.

147. Thorne RG, Hrabetova S, Nicholson C. Diffusion of epidermal growth factor in rat brain extracellular space measured by integrative optical imaging. Journal of Neurophysiology. 2004;92(6):3471-81. doi: 10.1152/jn.00352.2004. PubMed PMID: WOS:000225164800031.

148. Takano S, Yoshii Y, Kondo S, Suzuki H, Maruno T, Shirai S, et al. Concentration of vascular endothelial growth factor in the serum and tumor tissue of brain tumor patients. Cancer Research. 1996;56(9):2185-90. PubMed PMID: WOS:A1996UG75600041.

149. Lang UE, Gallinat J, Danker-Hopf H, Bajbouj M, Hellweg R. Nerve growth factor serum concentrations in healthy human volunteers: physiological variance and stability. Neuroscience Letters. 2003;344(1):13-6. doi: 10.1016/s0304-3940(03)00403-8. PubMed PMID: WOS:000183375300004.

150. Takayama H, Miyake Y, Nouso K, Ikeda F, Shiraha H, Takaki A, et al. Serum levels of platelet-derived growth factor-BB and vascular endothelial growth factor as prognostic factors for patients with fulminant hepatic failure. Journal of Gastroenterology and Hepatology. 2011;26(1):116-21. doi: 10.1111/j.1440-1746.2010.06441.x. PubMed PMID: WOS:000285765800022.

151. Gannoun MB, Bourrelly S, Raguema N, Zitouni H, Nouvellon E, Maleh W, et al. Placental growth factor and vascular endothelial growth factor serum levels in Tunisian Arab women with suspected preeclampsia. Cytokine. 2016;79:1-6. doi: 10.1016/j.cyto.2015.12.005. PubMed PMID: WOS:000370109600001.

152. Perez D, Rohde A, Callejon G, Perez-Ruiz E, Rodrigo I, Rivas-Ruiz F, et al. Correlation between serum levels of vascular endothelial growth factor-C and sentinel lymph node status in early breast cancer. Tumor Biology. 2015;36(12):9285-93. doi: 10.1007/s13277-015-3663-0. PubMed PMID: WOS:000367329300021.

153. Collaborators GMaCoD. Global, regional, and national age–sex specific all-cause and cause-specific mortality for 240 causes of death, 1990–2013: a systematic analysis for the Global Burden of Disease Study 2013. The Lancet. 2015;385(9963):117-71. doi: 10.1016/s0140-6736(14)61682-2.

154. Babiarz B, Romagnano L, Afonso S, Kurilla G. Localization and expression of fibronectin during mouse decidualization in vitro: Mechanisms of cell:matrix interactions. Developmental Dynamics. 1996;206(3):330-42. doi: 10.1002/(sici)1097-0177(199607)206:3<330::aid-aja10>3.3.co;2-7. PubMed PMID: WOS:A1996UU00500010.

155. Miner JH, Cunningham J, Sanes JR. Roles for laminin in embryogenesis: Exencephaly, syndactyly, and placentopathy in mice lacking the laminin alpha 5 chain. Journal of Cell Biology. 1998;143(6):1713-23. doi: 10.1083/jcb.143.6.1713. PubMed PMID: WOS:000077644800023.

156. Wiradjaja F, DiTommaso T, Smyth I. Basement Membranes in Development and Disease. Birth Defects Research Part C-Embryo Today-Reviews. 2010;90(1):8-31. doi: 10.1002/bdrc.20172. PubMed PMID: WOS:000276286600002.

157. Ma KD, Jin H, Hu R, Xiong Y, Zhou SF, Ting P, et al. A Proteomic Analysis of Placental Trophoblastic Cells in Preeclampsia-Eclampsia. Cell Biochemistry and Biophysics. 2014;69(2):247-58. doi: 10.1007/s12013-013-9792-4. PubMed PMID: WOS:000335983300009.

158. Kurdoglu M, Kurdoglu Z, Ozen S, Kucukaydin Z, Bulut G, Erten R, et al. Expression of laminin receptor 1 in human placentas from normal and preeclamptic pregnancies and its relationship with the severity of preeclampsia. Journal of Perinatal Medicine. 2011;39(4):411-6. doi: 10.1515/jpm.2011.024. PubMed PMID: WOS:000292642200009.

159. Risteli J, Foidart JM, Risteli L, Boniver J, Goffinet G. THE BASEMENT-MEMBRANE PROTEINS LAMININ AND TYPE-IV COLLAGEN IN ISOLATED VILLI IN PRE-ECLAMPSIA. Placenta. 1984;5(6):541-50. doi: 10.1016/s0143-4004(84)80008-9. PubMed PMID: WOS:A1984AAU7800008.

160. Winn VD, Gormley M, Fisher SJ. The impact of preeclampsia on gene expression at the maternal-fetal interface. Pregnancy Hypertension-an International Journal of Womens Cardiovascular Health. 2011;1(1):100-8. doi: 10.1016/j.preghy.2010.12.001. PubMed PMID: WOS:000209443200015.

161. Pati F, Jang J, Ha DH, Won Kim S, Rhie JW, Shim JH, et al. Printing three-dimensional tissue analogues with decellularized extracellular matrix bioink. Nature communications. 2014;5:3935. Epub 2014/06/03. doi: 10.1038/ncomms4935. PubMed PMID: 24887553; PubMed Central PMCID: PMC4059935.

162. Radisky ES, Radisky DC. Matrix Metalloproteinase-Induced Epithelial-Mesenchymal Transition in Breast Cancer. Journal of Mammary Gland Biology and Neoplasia. 2010;15(2):201-12. doi: 10.1007/s10911-010-9177-x. PubMed PMID: WOS:000278835900007.

163. Flynn L, Semple JL, Woodhouse KA. Decellularized placental matrices for adipose tissue engineering. Journal of Biomedical Materials Research Part A. 2006;79A(2):359-69. doi: 10.1002/jbm.a.30762. PubMed PMID: WOS:000241132500016.

164. Klebe RJ. ISOLATION OF A COLLAGEN-DEPENDENT CELL ATTACHMENT FACTOR. Nature. 1974;250(5463):248-51. doi: 10.1038/250248a0. PubMed PMID: WOS:A1974T571500053.

165. Crapo PM, Gilbert TW, Badylak SF. An overview of tissue and whole organ decellularization processes. Biomaterials. 2011;32(12):3233-43. doi: 10.1016/j.biomaterials.2011.01.057. PubMed PMID: WOS:000288629600008.

166. Discher DE, Janmey P, Wang YL. Tissue cells feel and respond to the stiffness of their substrate. Science. 2005;310(5751):1139-43. doi: 10.1126/science.1116995. PubMed PMID: WOS:000233437300033.

167. Daoud G, Barrak J, Abou-Kheir W. Assessment Of Different Trophoblast Cell Lines As In Vitro Models For Placental Development. Faseb Journal. 2016;30. PubMed PMID: WOS:000406444706426.

168. Ren QA, Guan S, Fu JL, Wang AG. Spatio-Temporal Expression of Matrix Metalloproteinases-2 and-9 in Porcine Endometrium During Implantation. Journal of Animal and Veterinary Advances. 2010;9(15):2074-81. PubMed PMID: WOS:000281374200016.

169. Karar J, Maity A. PI3K/AKT/mTOR pathway in angiogenesis. Frontiers in Molecular Neuroscience. 2011;4. doi: 10.3389/fnmol.2011.00051. PubMed PMID: WOS:000209370100048.

170. Pijnenborg R, Dhooghe T, Vercruysse L, Bambra C. Evaluation of trophoblast invasion in placental bed biopsies of the baboon, with immunohistochemical localisation of cytokeratin, fibronectin, and laminin. Journal of Medical Primatology. 1996;25(4):272-81. PubMed PMID: WOS:A1996VL83100004.

171. Shan N, Zhang X, Xiao X, Zhang H, Tong C, Luo X, et al. Laminin alpha 4 (LAMA4) expression promotes trophoblast cell invasion, migration, and angiogenesis, and is lowered in preeclamptic placentas. Placenta. 2015;36(8):809-20. doi: 10.1016/j.placenta.2015.04.008. PubMed PMID: WOS:000359875000006.

172. Wang LL, Yu Y, Guan HB, Liu T, Qiao C. 67-kDa Laminin receptor contributes to hypoxia-induced migration and invasion of trophoblast-like cells by mediating matrix metalloproteinase-9. Clinical and Experimental Pharmacology and Physiology. 2015;42(5):549-58. doi: 10.1111/1440-1681.12389. PubMed PMID: WOS:000353410100014.

173. Wong HS, Cheung YK. Sonographic study of the decidua basalis in early pregnancy loss. Ultrasound in Obstetrics & Gynecology. 2010;36(3):362-7. doi: 10.1002/uog.7736. PubMed PMID: WOS:000282149900018.

174. Langenbach KJ, Rando TA. Inhibition of dystroglycan binding to laminin disrupts the PI3K/AKT pathway and survival signaling in muscle cells. Muscle & Nerve. 2002;26(5):644-53. doi: 10.1002/mus.10258. PubMed PMID: WOS:000179029100007.

175. Guilak F, Cohen DM, Estes BT, Gimble JM, Liedtke W, Chen CS. Control of Stem Cell Fate by Physical Interactions with the Extracellular Matrix. Cell Stem Cell. 2009;5(1):17-26. doi: 10.1016/j.stem.2009.06.016. PubMed PMID: WOS:000267879200007.

176. Sellaro TL, Ranade A, Faulk DM, McCabe GP, Dorko K, Badylak SF, et al. Maintenance of Human Hepatocyte Function In Vitro by Liver-Derived Extracellular Matrix Gels. Tissue Engineering Part A. 2010;16(3):1075-82. doi: 10.1089/ten.tea.2008.0587. PubMed PMID: WOS:000275041500030.

177. Borbely AU, Sandri S, Fernandes IR, Prado KM, Cardoso EC, Correa-Silva S, et al. The term basal plate of the human placenta as a source of functional extravillous trophoblast cells. Reproductive Biology and Endocrinology. 2014;12. doi: 10.1186/1477-7827-12-7. PubMed PMID: WOS:000331637300001.

178. Bracaglia L, Messina M, Winston S, Kuo C-Y, Lerman M, Fisher J. 3D Printed Pericardium Hydrogels To Promote Wound Healing in Vascular Applications. Biomacromolecules. 2017;Article ASAP.

179. Swartz MA, Fleury ME. Interstitial flow and its effects in soft tissues. Annual Review of Biomedical Engineering. 2007;9:229-56. doi: 10.1146/annure/bioeng.9.060906.151850. PubMed PMID: WOS:000249337000008.

180. Dimmeler S, Assmus B, Hermann C, Haendeler J, Zeiher AM. Fluid shear stress stimulates phosphorylation of Akt in human endothelial cells - Involvement in suppression of apoptosis. Circulation Research. 1998;83(3):334-41. PubMed PMID: WOS:000075287300013.

181. James JL, Whitley GS, Cartwright JE. Shear stress and spiral artery remodelling: the effects of low shear stress on trophoblast-induced endothelial cell apoptosis. Cardiovascular research. 2011;90(1):130-9. Epub 2010/12/16. doi: 10.1093/cvr/cvq396. PubMed PMID: 21156824.

182. Chen T, Buckley M, Cohen I, Bonassar L, Awad HA. Insights into interstitial flow, shear stress, and mass transport effects on ECM heterogeneity in bioreactor-cultivated engineered cartilage hydrogels. Biomechanics and Modeling in Mechanobiology. 2012;11(5):689-702. doi: 10.1007/s10237-011-0343-x. PubMed PMID: WOS:000303378200009.

183. Polacheck WJ, Charest JL, Kamm RD. Interstitial flow influences direction of tumor cell migration through competing mechanisms. Proceedings of the National Academy of Sciences of the United States of America. 2011;108(27):11115-20. doi: 10.1073/pnas.1103581108. PubMed PMID: WOS:000292376700042.

184. Aguilar HN, Mitchell BF. Physiological pathways and molecular mechanisms regulating uterine contractility. Human Reproduction Update. 2010;16(6):725-44. doi: 10.1093/humupd/dmq016. PubMed PMID: WOS:000283123200014.

185. Halasz M, Szekeres-Bartho J. The role of progesterone in implantation and trophoblast invasion. Journal of reproductive immunology. 2013;97(1):43-50. Epub 2013/02/26. doi: 10.1016/j.jri.2012.10.011. PubMed PMID: 23432871.

186. Kuklina EV, Ayala C, Callaghan WM. Hypertensive Disorders and Severe Obstetric Morbidity in the United States. Obstetrics and Gynecology. 2009;113(6):1299-306. PubMed PMID: WOS:000266392400015.

187. American College of Obstetricians and Gynecologists. Task Force on Hypertension in Pregnancy, American College of Obstetricians and Gynecologists. Hypertension in pregnancy. Washington, DC: American College of Obstetricians and Gynecologists; 2013. x, 89 pages p.

188. Bergmann F, Rotmensch S, Rosenzweig B, How H, Chediak J. THE ROLE OF VONWILLEBRAND-FACTOR IN PREECLAMPSIA. Thrombosis and Haemostasis. 1991;66(5):525-8. PubMed PMID: WOS:A1991GM14700003.

189. Friedman SA, Degroot CJM, Taylor RN, Golditch BD, Roberts JM. PLASMA CELLULAR FIBRONECTIN AS A MEASURE OF ENDOTHELIAL INVOLVEMENT IN PREECLAMPSIA AND INTRAUTERINE GROWTH-RETARDATION. American Journal of Obstetrics and Gynecology. 1994;170(3):838-41. PubMed PMID: WOS:A1994NC56600029.

190. Boffa MC, Valsecchi L, Fausto A, Gozin D, D'Angelo SV, Safa O, et al. Predictive value of plasma thrombomodulin in preeclampsia and gestational hypertension. Thrombosis and Haemostasis. 1998;79(6):1092-5. PubMed PMID: WOS:000074281300004.

191. Schiff E, Benbaruch G, Peleg E, Rosenthal T, Alcalay M, Devir M, et al. IMMUNOREACTIVE CIRCULATING ENDOTHELIN-1 IN NORMAL AND HYPERTENSIVE PREGNANCIES. American Journal of Obstetrics and Gynecology. 1992;166(2):624-8. PubMed PMID: WOS:A1992HE65600036.

192. Venkatesha S, Toporsian M, Lam C, Hanai J, Mammoto T, Kim YM, et al. Soluble endoglin contributes to the pathogenesis of preeclampsia. Nature medicine. 2006;12(6):642-9. Epub 2006/06/06. doi: 10.1038/nm1429. PubMed PMID: 16751767.

193. Shibata E, Rajakumar A, Powers RW, Larkin RW, Gilmour C, Bodnar LM, et al. Soluble fms-like tyrosine kinase 1 is increased in preeclampsia but not in normotensive pregnancies with small-for-gestational-age neonates: relationship to circulating placental growth factor. The Journal of clinical endocrinology and metabolism. 2005;90(8):4895-903. Epub 2005/05/12. doi: 10.1210/jc.2004-1955. PubMed PMID: 15886253.

194. Sargent IL, Germain SJ, Sacks GP, Kumar S, Redman CWG. Trophoblast deportation and the maternal inflammatory response in pre-eclampsia. Journal of Reproductive Immunology. 2003;59(2):153-60. doi: 10.1016/s0165-0378(03)00044-5. PubMed PMID: WOS:000184965800007.

195. Roland CS, Hu J, Ren CE, Chen HB, Li JP, Varvoutis MS, et al. Morphological changes of placental syncytium and their implications for the pathogenesis of preeclampsia. Cellular and Molecular Life Sciences. 2016;73(2):365-76. doi: 10.1007/s00018-015-2069-x. PubMed PMID: WOS:000368077900008.

196. Jackson MR, Mayhew TM, Boyd PA. QUANTITATIVE DESCRIPTION OF THE ELABORATION AND MATURATION OF VILLI FROM 10 WEEKS OF GESTATION TO TERM. Placenta. 1992;13(4):357-70. doi: 10.1016/0143-4004(92)90060-7. PubMed PMID: WOS:A1992JL97200005.

197. Yeatts AB, Choquette DT, Fisher JP. Bioreactors to influence stem cell fate: Augmentation of mesenchymal stem cell signaling pathways via dynamic culture systems. Biochimica Et Biophysica Acta-General Subjects. 2013;1830(2):2470-80. doi: 10.1016/j.bbagen.2012.06.007. PubMed PMID: WOS:000315304500021.

198. Staton CA, Reed MWR, Brown NJ. A critical analysis of current in vitro and in vivo angiogenesis assays. International Journal of Experimental Pathology. 2009;90(3):195-221. doi: 10.1111/j.1365-2613.2008.00633.x. PubMed PMID: WOS:000265981600001.

199. DeLisser HM, ChristofidouSolomidou M, Strieter RM, Burdick MD, Robinson CS, Wexler RS, et al. Involvement of endothelial PECAM-1/CD31 in angiogenesis. American Journal of Pathology. 1997;151(3):671-7. PubMed PMID: WOS:A1997XU37800006.

200. Ahmed A, Dunk C, Ahmad S, Khaliq A. Regulation of placental vascular endothelial growth factor (VEGF) and placenta growth factor (PIGF) and soluble Flt-1 by oxygen - A review. Placenta. 2000;21:S16-S24. doi: 10.1053/plac.1999.0524. PubMed PMID: WOS:000086840500005.

201. Fraser HM, Lunn SF. Angiogenesis and its control in the female reproductive system. British Medical Bulletin. 2000;56(3):787-97. doi: 10.1258/0007142001903364. PubMed PMID: WOS:000166109700017.

202. Lovett M, Lee K, Edwards A, Kaplan DL. Vascularization Strategies for Tissue Engineering. Tissue Engineering Part B-Reviews. 2009;15(3):353-70. doi: 10.1089/ten.teb.2009.0085. PubMed PMID: WOS:000269621100010.

203. Liu JS, Gartner ZJ. Directing the assembly of spatially organized multicomponent tissues from the bottom up. Trends in Cell Biology. 2012;22(12):683-91. doi: 10.1016/j.tcb.2012.09.004. PubMed PMID: WOS:000312052700010.

204. Velicky P, Knofler M, Pollheimer J. Function and control of human invasive trophoblast subtypes: Intrinsic vs. maternal control. Cell Adhesion & Migration. 2016;10(1-2):154-62. doi: 10.1080/19336918.2015.1089376. PubMed PMID: WOS:000374999400014.